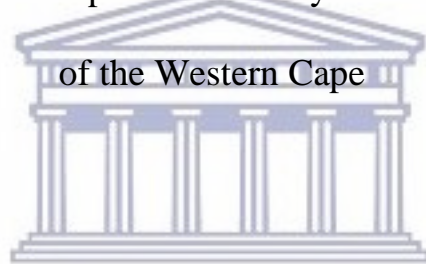


A study of SiC thin film layers for electrically conductive diffusion barrier
application in Si thin film solar cells.

Thandi Elinah Mazibuko

A minithesis submitted in partial fulfilment of the requirements for the degree
of Magister Scientiae in the Department of Physics and Astronomy, University



UNIVERSITY *of the*
WESTERN CAPE

Supervisor: Dr. S. Halindintwali, University of the Western Cape

Co-supervisors: Dr. O. Nemraoui, Cape Town University of Technology and

Prof. C. J. Arendse, University of the Western Cape

July 2019

KEYWORDS

Silicon

Solar cells

Silicon carbide

Transition metal contamination

Diffusion barrier

Ion implantation

Annealing

Spectrometry

Depth profile



UNIVERSITY *of the*
WESTERN CAPE

ABSTRACT

Semiconductor silicon carbide (SiC) thin films of different thicknesses were deposited by electron beam physical vapour deposition (EBPVD) for application as diffusion barrier application to guard against metal contaminants in Si silicon solar cells. The deposited films were implanted with a high and low fluence of 5×10^{16} ions/cm² and 1×10^{16} ions/cm²; before implantation stopping of ions in matter (SRIM) software package was used to simulate an implantation profile. Realtime Rutherford backscattering spectrometry (real-time-RBS) studies were done on the implanted films ramping from room-temperature (RT) to temperature of 600 °C, which was the maximum temperature that the heater in the system used could achieve, show that Ag was stable until the probed temperature range. Subsequent isochronal annealing experiments were done for 1 hour at 650 °C and 950 °C. The simulations of RBS spectra and Energy dispersive X-ray (EDX) spectroscopy results revealed a gradual Ag decrease in the films with increasing temperature. The broadening and the appearance of new small peaks on the implantation profile of Ag suggest the onset of the metal diffusion in the film. Fourier transform infrared (FTIR) spectroscopy studies showed that the width of the SiC vibration peak at around 800 cm⁻¹ becomes narrower as the temperature is increased, suggesting a crystallization in SiC; the grain boundaries might thus be the pathway of the diffusing Ag. Scanning electron microscopy (SEM) micrographs showed a roughening of the film surface of the same layer in which the onset of diffusion was observed at 850 °C; this suggested a crystallization of the film in agreement with FTIR investigation. This temperature was thus chosen for isothermal annealing studies. As in the case of isochronal annealing, a gradual decrease and change in the shape of the Ag RBS profile both towards the surface and to the interface; this was interpreted as in-diffusion and out-diffusion competing mechanisms.

July 2019

DECLARATION

I declare that *A study of SiC thin film layers for electrically conductive diffusion barrier application in Si thin film solar cells* is my own work, that it has not been submitted for any degree or examination in any other university, and that all sources I have used or quoted have been indicated and acknowledged by complete references.

Thandi Elinah Mazibuko

July 2019



Signature:

A handwritten signature in blue ink, appearing to read "Thandi Elinah Mazibuko".

DEDICATION

To my mother, Selinah Nana Mazibuko, thank you for being my rock, my stronghold and for your unwavering love.

To my brother, Sphiwe Lukas Mazibuko, thank you for a blessing that you have been in my life.



UNIVERSITY *of the*
WESTERN CAPE

ACKNOWLEDGMENTS

Dr. Sylvain Halindintwali of the Department of Physics at the University of the Western Cape (UWC) for giving me the opportunity to be his student, his guidance and support throughout this investigation,

Dr. Christopher Mtshali of Materials Research Department at iThemba LABS for his assistance with deposition, annealing, and Rutherford Backscattering spectrometry experiments,

Dr. Morgan Madhaku of Tandem and Accelerator Mass Spectrometry Department at iThemba LABS for his assistance with ion implantation and Rutherford Backscattering experiments,

Dr. Philip Sehogela of Tandem and Accelerator Mass Spectrometry Department at iThemba LABS, Gauteng for his assistance with Rutherford Backscattering experiments,

Mr. Timothy Lesch of the Department of Chemistry at UWC, for his assistance with FTIR measurements,

Mr. Siphelo Ngqoloda and Mr. Stephen Klue of the Department of Physics at UWC, for their assistance with annealing experiments,

Mr. Earl Mc Donald and Mr. Adrian Josephs of the Electron Microscopy Unit at UWC for their assistance with SEM measurements,

Mrs. Valencia Jamalie of the Department of Chemistry at UWC for her support and words of encouragement throughout this study,

My fellow friends Puleng and Likhapha for their much-appreciated friendship, and

A special thanks to my friend Senamile Nhlalwenhle Ntuli, for her continuous support and encouragement during the last few months of this project.

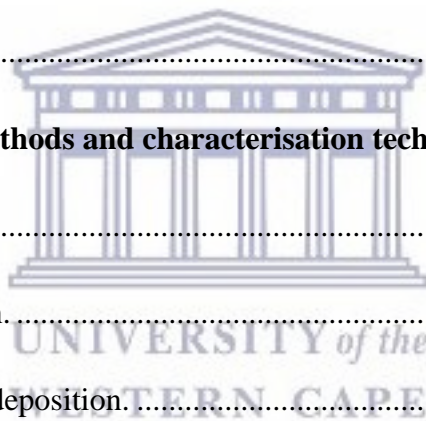
This work is supported by the National Nanoscience Postgraduate Teaching and Training Programme (NNPTTP), a collaborative initiative between the University of the Western Cape (UWC), University of Johannesburg (UJ), University of the Free State (UFS), the Nelson Mandela Metropolitan University (NMMU) and the Department of Science and Technology (DST).



Table of contents.

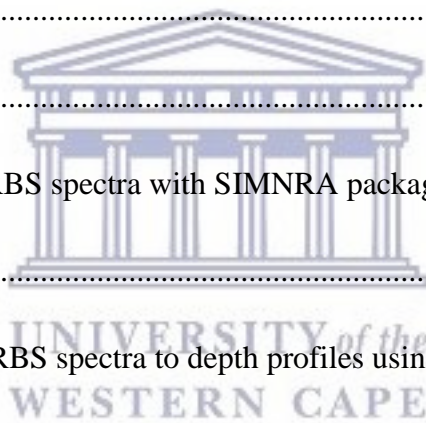
KEYWORDS	i
ABSTRACT	ii
DECLARATION	iii
DEDICATION	iv
ACKNOWLEDGMENTS	v
Table of contents.	vii
Chapter 1: Introduction.	1
1.1 Solar energy and photovoltaic technology.....	1
1.1.1 Three generations of photovoltaic technology.....	2
1.1.2 Crystalline Silicon solar cells.....	3
1.2 Background on silicon carbide thin films.....	6
1.2.1 Silicon carbide crystallographic forms.....	6
1.2.2 Amorphous and microcrystalline silicon carbide.....	9
1.3 Aims and outlines.....	10
References.....	11
Chapter 2 Overview of elemental diffusion.	15
2.1 Introduction.....	15
2.2 Effect of contamination from transition metals in Si.....	15
2.2.1 Points defects in crystals.....	16
2.2.2 Shockley Read Hall recombination.....	18
2.2.3 Impact of silver impurities on electronic transport in Si.....	20

2.3 Diffusion mechanism.....	20
2.3.1 Fick’s laws of diffusion.....	21
2.3.2 Diffusion mechanisms.....	23
2.3.2.1 Self diffusion mechanism.....	23
2.3.2.2 Substitutional diffusion mechanism.....	24
2.3.2.3 Interstitial diffusion mechanism.....	25
2.3.2.4 Grain boundary diffusion mechanism.....	25
2.3.3 Factors affecting diffusion.....	26
2.3.3.1 Activation energy for diffusion.....	26
2.3.3.2 Temperature and the diffusion coefficients.....	26
2.3.3.3 Type of diffusion.....	27
2.4 Nature of silver defects contributing to diffusion in SiC.....	28
References.....	31
Chapter 3: Experimental methods and characterisation techniques.....	34
3.1 Introduction.....	34
3.2 Physical vapour deposition.....	34
3.2.1 Preparation and sample deposition.....	36
3.3 Elementary principles governing ion implantation.....	38
3.3.1 Introduction.....	38
3.3.2 Stopping power.....	39
3.3.3 Energy loss in compounds.....	41
3.3.4 Energy straggling.....	42
3.3.5 Simulation of stopping power of ions in matter.....	44
3.4 Rutherford Backscattering Spectrometry.....	47
3.4.1 Basics on Rutherford backscattering spectrometry.....	48
3.4.1.1 Realtime studies on Ag implanted in silicon carbide Rutherford backscattering spectrometry.....	51



3.4.1.2 Basic Concepts and Analysis.....	52
3.4.1.3 Kinematic factor and mass resolution.	53
3.4.1.4 The relation between energy loss and thin film thickness.....	55
3.4.1.5 Stopping power and energy loss.....	55
3.4.1.6 Evaluation of energy loss.	56
3.4.1.7 Energy loss due to straggling in compounds.....	57
3.4.1.8 Scattering Cross Section.....	58
3.4.2 Instrumentation in relation to conventional Rutherford backscattering spectroscopy....	60
3.4.3 Computer simulation and fitting programs for analysis of RBS spectra.	61
3.5 Scanning electron microscopy-energy dispersive spectroscopy.....	61
3.5.1 Introduction.....	61
3.5.2 Basic principles of scanning electron microscopy.....	62
3.5.2.1 Basic principle.....	62
3.5.2.2 Instrumentation related to scanning electron microscopy.	64
3.5.3 Energy dispersive spectroscopy.....	66
3.5.3.1 Basic principle of Energy-dispersive X-ray spectroscopy.	66
3.5.3.2 Instrumentation related to energy dispersive X-ray spectroscopy.....	68
3.6 Fourier transform Infrared spectroscopy.....	69
3.6.1 Introduction.....	69
3.6.2 Fundamentals on Fourier transform infrared spectroscopy.	69
3.6.3 Vibrational modes.....	71
3.6.3 Bonding in Silicon carbide films.	72
References.....	73
Chapter 4 Results and discussion.....	77
4.1 Introduction.....	77
4.2 Thickness determination from the simulation of RBS spectra.	77
4.3 The effect of fluence on the microstructure of silicon carbide films.....	80
4.4 Annealing studies on Ag implanted silicon carbide films.	84

4.4.1 The stability of Ag in SiC deposited films at low temperatures.	84
4.4.2 Isochronal annealing studies using SEM/EDX.	85
4.4.3 Isochronal annealing studies using RBS.	89
4.4.4 Isothermal annealing studies by RBS.	90
4.6 Ag depth profiling.	93
4.7 Proposed mechanism of diffusion.	99
4.8 Summary and recommendations.	101
4.8.1 Conclusions.	101
4.8.2 Recommendations for future studies	102
References.	103
Appendix A.	104
Basic steps for simulation of RBS spectra with SIMNRA package.	104
Appendix B.	106
Basic steps for conversion of RBS spectra to depth profiles using DataFurnace package.	106





UNIVERSITY *of the*
WESTERN CAPE

Chapter 1: Introduction.

1.1 Solar energy and photovoltaic technology.

The increasingly imperative demand for clean and renewable energy has led to the emergence of solar power as one of the best sustainable energies for the future. Solar radiation is directly converted into either thermal or electrical power by thermal and photovoltaic (PV) processes respectively [1.1]. The sun is an abundant energy source that is available although non-uniformly distributed. The energy radiated from the sun in the outer atmosphere is 3.8×10^{20} MW but only 173×10^6 kW [1.1] reaches the surface of the earth. Multiple factors contribute to this energy loss such as scattering, absorption, reflection, and the weather.

The availability of insolation at a given location on earth depends on the weather of the region as well as the time of day. This intermittent nature of solar energy introduces a challenge when designing solar panels. The selection of the semiconductor is important for optimized collection efficiency. Solar cells make use of an intrinsic semiconductor absorber of photons.

Si-based commercial solar cells have an overall conversion efficiency of ~15% [1.1], the cell performance can be improved towards maximum theoretical efficiency by mitigating the source of losses. For the PV technology to be competitive with conventional established technologies for power generation, not only the manufacturing cost of panels has to be lowered but also losses have to be minimized. One of the challenges in Si-based solar cells is the presence of transition metal impurities [1.2 – 1.4]. These metals have a deleterious effect on the minority carrier lifetime, especially when found at substitutional and interstitial lattice positions [1.4 – 1.6].

Silicon carbide (SiC) has been actively utilized as the main diffusion barrier in fuel particles in high-temperature nuclear reactors to guard against the release of radioactive fission products such as Ag [1.7 - 1.8]. SiC is used in these fuel particles because it can withstand high-temperature operating conditions. The study of silver (Ag) transport mechanisms in SiC has been intensively researched in SiC diffusion barrier coatings for nuclear reactor fuel particles [1.7 – 1.9]. However, there is not much-published research on the use of SiC as a diffusion barrier against metal contaminants in solar cells.

1.1.1 Three generations of photovoltaic technology.

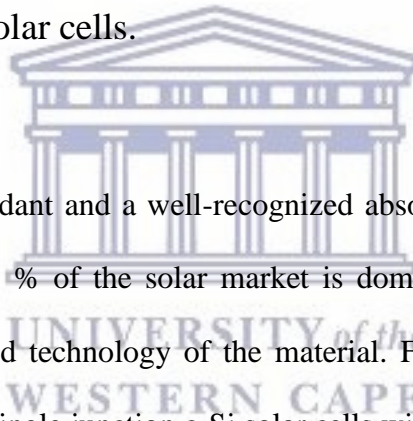
The overall awareness about the significance of renewable energy has resulted in the rapid growth of PV technologies, leading to increased PV devices development and fabrication [1.1, 1.10]. The PV industry is categorized into three basic chronological successive types, namely, wafer based (1st generation PV), thin film (2nd generation PV) and the so-called 3rd generation PVs, which include organic, dye-sensitized (DSSC), perovskite and quantum dots cells. [1.11].

Crystalline silicon (c-Si) (single or multi-crystalline) and gallium arsenide (GaAs) cells belong to the first generation of PVs [1.3]. Thin film technology provides alternative absorber materials to c-Si, such as amorphous silicon (a-Si) or a combination of amorphous and microcrystalline silicon (a-Si/ μ c-Si), the compound semiconductor made of copper, indium, gallium, and selenium (CIS or CIGS) and group III – V materials (GaAs, InP, and AlGaAs) [1.11]. Solar cells made from these materials are referred to as thin film cells because of the reduction of the thickness of the absorber to a few micrometers thick.

Crystalline silicon has an indirect band-gap, this means that there are both changes of energy and momentum of the excited charge carriers from the valence to the conduction band. Due to

the required change in momentum, there is less probability of photon's absorption [1.12]. As a result, the absorption coefficient of c-Si is lower than that of amorphous Si where the requirement of momentum conservation is relaxed [1.12]. Therefore the absorption coefficient of a-Si:H is much larger than that of c-Si. Hydrogenated amorphous silicon has a band gap in the order of 1.6 – 1.8 eV, which can be tuned by the amount of hydrogen incorporated in the Si network. The high absorption coefficient of a-Si:H allowed the evolution from first generation solar cells to thin film based solar cells (second generation).

1.1.2 Crystalline Silicon solar cells.



Si is a stable, non-toxic, abundant and a well-recognized absorber material with an indirect bandgap of 1.12 eV [1.3]. 90 % of the solar market is dominated by c-Si because of the developed and well-established technology of the material. Fig. 1.1 shows the Shockley – Queisser efficiency curve for single junction c-Si solar cells with a theoretical efficiency limit of 33, 5%. However, these single junction solar cells only convert a fraction of the solar spectrum into electricity [1.4]. The efficiency can be increased up to 46% by stacking several materials of different bandgap values, the higher gap layers on top in order to filter the short wavelength photons first; such arranged structure is known as a multi-junction solar cell. [1.1, 1.11, 1.13].

A conventional single-junction solar cell has a characteristic band gap, E_g . The energy of the photon is given proportional to its frequency $\bar{\nu}$ as

$$E = h\bar{\nu} \quad (1.1)$$

If the photon's energy is greater than the bandgap value of the material, it is absorbed and the excess energy is lost by thermalization [1.14]. Whereas, if the photon energy is less than E_g , it is neither absorbed or reflected but transmitted [1.14].

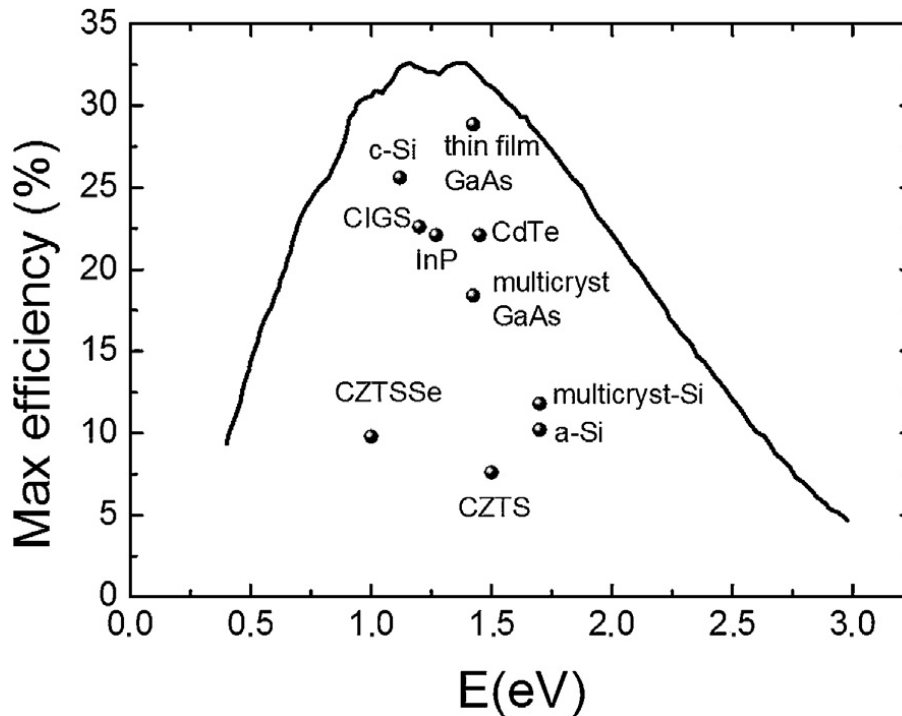


Figure 1.1: Shockley – Queisser efficiency curve for a single junction solar cell under AM1.5 illumination. The points represent the best experimental single junction cells fabricated to date.

The solar spectrum has a wide photon range that extends from around 0.39 eV in the far infrared to about 4.3 eV in the UV; this means that the efficiency of any single-junction solar cell is inherently limited. One way to circumvent this limitation is to divide the spectrum into several spectral regions and convert each region with its own junction whose band gap is tuned to that region [1.14]. This multi-junction concept requires a way of directing the different regions of the incident solar spectrum to the corresponding junctions [1.14]. This is done by stacking the junction with the highest band-gap on top, the second highest underneath and so forth [1.13]. Although multi-junction solar cells have high efficiencies, the fundamental

challenge remains to find materials with optimal band-gaps while maintaining a near-ideal material quality [1.14]. Effects of dislocation arising from mix-matched materials also present a huge challenge [1.14]. Moreover, multi-junction solar cells are often too expensive for general use [1.11, 1.13].

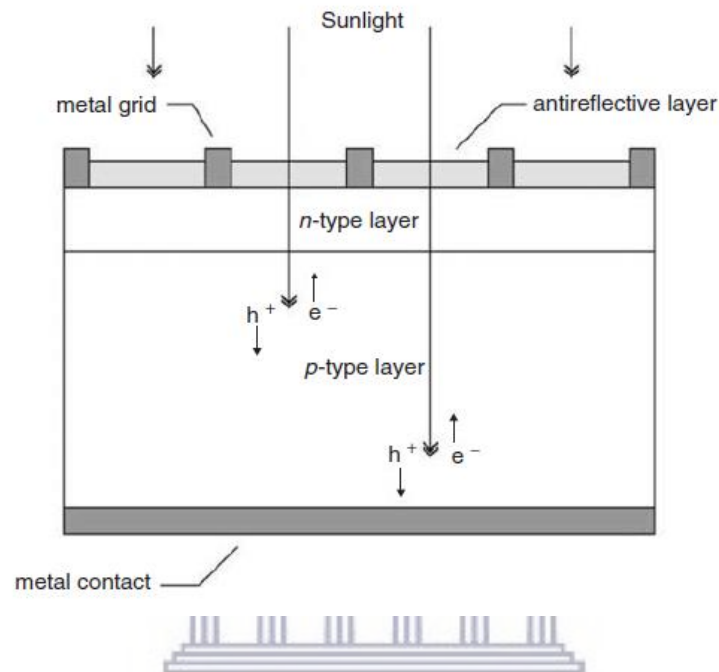


Figure 1.2: A schematic depiction of a simple conventional solar cell [1.15].

Fig. 1.2 represents a schematic of a conventional solar cell [1.1]. The cell is made up of p-type semiconductor material and an n-type semiconductor material [1.1] forming what is termed the p-n junction where they meet. Solar energy is incident on top, on the front of the solar cell. A metallic grid forms one of the electrical contacts of the cell and allows light to fall on the semiconductor between the gridlines converting the light into electrical energy. An anti-reflective coating (ARC) on top of the n-type layer increases the amount of light transmitted to the semiconductor. The second electrical contact is formed by a metallic layer at the back of the solar cell [1.15]. The difference in thickness between the n-type layer and p-type layer is due to the fact that minority charge carriers must reach the p-n junction before they can recombine with majority charge carriers. Holes are the minority carriers in the n-region and

they have lower mobility than the electrons; the n-layer must thus be thin in the order of magnitude of the diffusion length of holes in order to minimize their recombination.

1.2 Background on silicon carbide thin films.

SiC is a wide band gap semiconductor compound made of silicon and carbon. It has superior material properties to Si [1.1]. SiC has ten times the electric field strength, three times the thermal conductivity of Si [1.1], and has a widely tunable bandgap, up to 3.3 eV [1.10]. SiC is termed a wide bandgap semiconductor because more energy is required to excite an electron from the top of the valence band to the conduction band. This leads to a decrease in the intrinsic carrier concentration thereby reducing the device leakage current, a material property that makes it suitable for operation in high-temperature conditions [1.1]. Therefore, SiC can be used in the processing of electronic and optoelectronic devices such as solar cells, for example as window layer [1.16]. Additionally, it can find application high-power and high-temperature application such as in nuclear reactors. Moreover, SiC has excellent thermal and mechanical stability [1.10, 1.16].

1.2.1 Silicon carbide crystallographic forms.

SiC is the only chemically stable form of Si and carbon [1.17]. It is covalently bonded, and the distance between the Si and C atom is approximately 1.87 Å [1.18]. In SiC crystal structures, each Si is bonded to four neighbouring carbon atoms, or vice versa, forming strong tetrahedral sp³-bonds, as depicted in Fig. 1.3. The crystal structure of SiC can be thought to consist of a

close-packed stacking of Si-C double-atomic layers. The stacking of the double-atomic layers is along the c-axis and follows one of the three possible relative positions; A, B, and C as shown in Fig. 1.4. The three types of double-atomic layers, A, B, and C form a periodical series with a specific repeating unit along the c-axis.

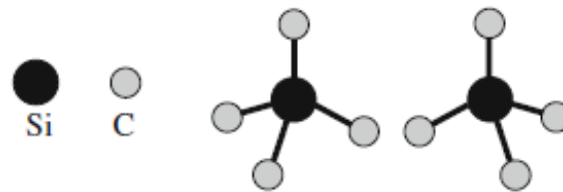


Figure 1.3: Tetrahedrons forming the building blocks of crystalline SiC.

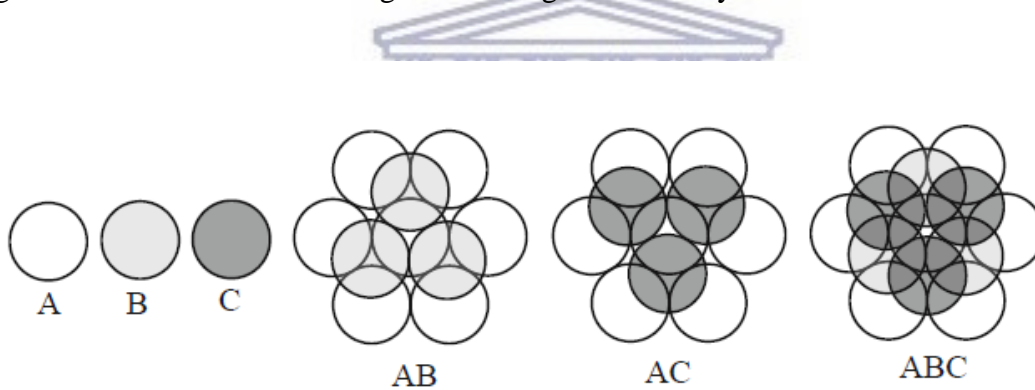


Figure 1.4: The arrangement of three possible positions (A, B, and C) of Si-C double-atomic layers along the stacking direction or c-axis. The c-axis is normal the plane of the paper.

The c-axis is normal the plane of the paper. The stacking sequence of the double-atomic layers is responsible for SiC's large number of crystallographic forms called polytypes. For example, 3C-SiC has a stacking sequence of the form ABCABC... This way of writing the polytype, where the digit is followed by the letter, is known as the Ramsdell notation. The digit denotes the number of double-atomic layers in one repeating unit and the letter represents the

crystallographic structure. For example, we have “C” for cubic, “H” for hexagonal and “R” for rhombohedral crystal structure. 3C-SiC is the only cubic form of SiC. The prevalent polytypes of SiC are hexagonal such as the 2H, 4H, and 6H with stacking sequences of ABAB, ABCBABC, and ABCACBABCACB... respectively. There are other types of SiC crystal forms, which are less common, for instance, the 15R.

The various polytypes do not only differ in their stacking sequence but also exhibit different electronic and optical properties. For example, the indirect bandgaps, at room temperature, of 3C-SiC, 6H-SiC and 4H-SiC are 2.2 eV, 2.86 eV (or 3.02 eV) and 3.2 – 3.3 eV, respectively.

8

The bandgap is dependent on the temperature so that the measured room temperature bandgaps of specific polytypes may be different, within a small range. The range of uncertainty is mostly influenced by the varying ways different researchers in different laboratories estimate the optical absorption edge [1.19]. Table 1.1 below shows properties of common SiC polytypes in comparison to Si.

Table 1.1: Properties of common silicon carbide polytypes in comparison to Si [1.1, 1.20].

Material property	Unit	Si	3C-SiC	6H-SiC	4H-SiC
Crystal Structure	--	Diamond	Cubic	Hexagonal	Hexagonal
Energy Gap	eV	1.12	2.403	3.101	3.26 - 3.285
Electron mobility	Cm ² /(Vs)	1200		370	720 - 900
Thermal conductivity	W/cm ⁻¹ k ⁻¹	1.3	3.2	3.6	3.7 – 4.9

1.2.2 Amorphous and microcrystalline silicon carbide.

Amorphous SiC (a-SiC) is a wide band gap material with high thermal oxidation, high hardness and IR transmittance [1.21 - 1.22]. This material can be used in the processing of electronic and optoelectronic devices [1.22]. Plasma enhanced chemical vapour deposition (PECVD) and hot wire chemical vapour deposition (HWCVD) are commonly used methods to grow hydrogenated amorphous SiC (a-SiC: H) [1.21, 1.22, 1.24] whereas its non-hydrogenated counterpart, a-SiC, can be synthesized using physical deposition methods such as sputtering, carbon ion implantation in Si, pulsed laser deposition [1.21], and e-beam evaporation.

The presence of hydrogen in a-SiC: H significantly changes the microstructure and properties of a-SiC and may be desirable depending on the property of interest [1.23]. Hydrogen has the beneficial effect of reducing the defect density in the layers by passivating the formed dangling bonds during the deposition process. a-SiC:H is used as a wide band gap intrinsic layer or window layer in multilayer hydrogenated amorphous Si (a-Si:H) solar cells [1.24- 1.27].

Hydrogenated microcrystalline silicon – carbide alloys ($\mu\text{c-Si}_{1-x}\text{C}_x\text{:H}$) are potential candidates as they exhibit a higher conductivity than their amorphous counterpart because of the presence of submicron size Si crystallites embedded in an amorphous silicon-carbon matrix [1.28] and a large energy gap than that of $\mu\text{c-Si:H}$ due to the incorporation of carbon. Si-rich a-SiC_x: H thin films exhibit excellent surface passivation properties [1.27].

1.3 Aims and outlines.

The aim of our investigation is to study the properties of silicon carbide as a diffusion barrier for application in Si solar cells. This is achieved by implanting Ag ions into silicon carbide thin films deposited on Si (100) substrates by the e-beam evaporation method.

The thesis is outlined as follows:

Chapter 1 gives a background on the basics of solar cells and on the three generations of photovoltaic technology. An introduction on semiconductor silicon carbide polytypes and their main properties is provided.

In Chapter 2, the detrimental impact of transition metal contamination on Si-based solar cell is discussed. Moreover, the presence of point defects and how they facilitate various diffusion mechanisms in crystals is discussed. Fick's laws of diffusion and factors affecting diffusion are discussed.

Chapter 3 discusses the methods and experimental techniques used; EBPVD) technique is used for the samples processing and ion implantation in the layers are described. The fundamentals of the analytical techniques used (RBS, SEM/EDX, and FTIR) are given.

In chapter 4, we present the results obtained and they are discussed. We contrast the diffusion process of implanted Ag in for both isothermally and isochronally annealed films. We correlate RBS, SEM/EDX, and FTIR findings.

The last part of the thesis gives a summary of the results as well as the recommendations for future work.

References.

- [1.1] B. N. Pushpakaran, A. S. Subburaj, S. B. Bayne, and J. Mookken, *Impact of silicon carbide semiconductor technology in Photovoltaic Energy System*, Renewable Sustainable Energy Review 55 (2016) 971–989.
- [1.2] I. Witting, N. Stoddard, and G. Rozgonyi, Proceedings: 18th Workshop Crystal Silicon Solar Cells Modules, 2008, 155-158.
- [1.3] S.H. Muller, G.M. Tuynman, E.G. Sieverts, and C.A.J. Ammerlaan, *Electron Paramagnetic resonance on iron-related centers in silicon*, Physics Review B 25 (1) (1982) 25 40.
- [1.4] H.H.A.A. Istratov, and E.R. Weber, *Iron and its complexes in silicon*, Applied Physics A Materials 69 (1) (1999) 13-44.
- [1.5] V.P. Markevich, S. Leonard, A.R. Peaker, B. Hamilton, A.G. Marinopoulos, and J. Coutinho, *Titanium in silicon: lattice positions and electronic properties*, Applied Physics Letters 104 (2014) 152-105.
- [1.6] R. Holzl, L. Fabry, and K.J. Range, *Gettering efficiencies for Cu and Ni as a function of size and density of oxygen precipitates in p/p- silicon epitaxial wafers*, Applied Physics A- Materials Science and Processing 73 (2001) 137–142.
- [1.7] E. Friedland, J.B. Malherbe, N.G. van der Berg, T. Hlatshwayo, A.J. Botha, E. Wendler, and W. Wesch, *Study of silver diffusion in silicon carbide*, Journal of Nuclear Materials 389 (2009) 326–331. 12
- [1.8] T. J. Gerczak, B. Leng, K. Sridharan, J. L. Hunter, A. J. Giordani and T. R. Allen, *Observations of Ag diffusion in ion implanted SiC*, Journal of Nuclear Materials 461 (2015)

[1.9] T.T. Hlatshwayo, *Diffusion of silver in 6H-SiC*, Ph.D. Thesis, Department of Physics, University of Pretoria (2010).

[1.10] P. M. Kaminski, A. Abbas, K. Bass, and G. Claudio, *Passivation of silicon wafers by Silicon Carbide (SiC_x) thin film grown by sputtering*, Energy Procedia, 10 (2011) 71–75.

[1.11] E. Płaczek-Popko, *Top PV market solar cells 2016*, Optoelectronics Review 25 (2) (2017) 55–64.

[1.12] K. Jager, O. Isabella, A.H.M. Smets, R.A.C.M.M.V Swaij, and M. Zeman, *Solar energy fundamentals, technology and system*, Delft University of Technology, 2014,

[1.13] M. Syvajarvi , Q. Ma, V. Jokubavicius, A. Galeckas, J. Sun, X. Liu, M. Jansson, P. Wellmann, M. Linnarsson, P. Runde, B. A. Johansen, A. Thøgersen, S. Diplas, P. A. Carvalho, O. M Løvvik, D. N. Wright, A. Y. Azarov, and B. G. Svensson, *Cubic silicon carbide as a potential photovoltaic material*, Solar Energy Materials and Solar Cells, 145 (2016) 104–108.

[1.14] D. J. Friedman, *Progress and challenges for next-generation high-efficiency multijunction solar cells*, Current opinion in solid state and materials science 14 (2010) 131-138.

[1.15] J. L. Grey, *Chapter 3: The physics of the solar cells*, Purdue University, West Lafayette, Indiana, USA.

[1.16] S. Janz, *Amorphous Silicon Carbide for Photovoltaic Applications*, Ph.D. Thesis, Fraunhofer Institut für Solare Energiesysteme Freiburg, 2007.

[1.17] G. L. Harris, *Properties of silicon carbide*, 1995. Accessed on https://books.google.co.za/books/about/Properties_of_Silicon_Carbide.html?id=Yy_B8GzxNlgC&redir_esc=y

[1.18] J.H. van Laar, I.J. van der Walt, H. Bissett I G.J. Puts, and P.L. Crouse II P, *Synthesis and deposition of silicon carbide nanopowders in a microwave- induced plasma operating at low to atmospheric pressures*, Journal of the Southern African Institute of Mining and Metallurgy 115 (2015) 949–955.

[1.19] J. Fan and P. K. Chu, *Silicon Carbide Nanostructures*, Switzerland, Springer International Publishing, 2014.

[1.20] P. Masri, *Silicon carbide and silicon carbide-based structures: The physics of epitaxy*, Surface Science Reports 48 (2002) 1–51.

[1.21] A. Majid, *A perspective on non-stoichiometry in SiC*, Ceramic international 44 (2018) 1277 -1283.

[1.22] T. Christidis, M. Tabbal, S. Isber, M.A. El Khakani, and M. Chaker, *Comparative EPR study of hydrogenated and amorphous silicon carbide thin films*, Applied surface science 184 (2001) 268 – 272.

[1.23] M. A. Petrich, K. K. Gleason, and J. A. Reimer, *Structure and properties of amorphous hydrogenated silicon carbide*, Physical Review B, 36 (1987), 9722 – 9731.

[1.24] T.Chen, Y. Huang, A. Dasgupta, M. Laysberg, L. Houben, D. Yang, R. Carius, and F. Finger, *Microcrystalline silicon carbide window layers in thin films silicon solar cells*, Solar Energy Materials & solar cells 98 (2012) 370 – 378.

[1.25] J.L. He, M.H. Hon, and L.C. Chang, *Properties of amorphous silicon carbide deposited on glass*, Materials chemistry and physics 45 (1996) 43 – 49.

[1.26] M. Pomaska, W. Beyer, E. Neumann, F. Finger, and K. Ding, *Impact of microcrystalline silicon carbide growth using hot wire chemical vapour deposition on crystalline silicon surface passivation*, Thin solid films 592 (2015) 217 – 220. 14

[1.27] S. Gaiaschi, R. Ruggeri, E.V. Johnson, P. Bulkin, P. Chapon, M. –E. Gueunier-Farret, G. Mannino, C. Longeaud, and J. –P. Kleider, *Structural properties of hydrogenated microcrystalline silicon – carbon alloys deposited by radio frequency plasma enhanced chemical deposition: effect of microcrystalline silicon seed layer and methane*, Thin solid films 550 (2014) 312 – 318.

[1.28] J. Huran, A. Valovip, A.P. Kobzev, N.I. Balalykin, M. Kuþera, Ő. Haþpik, d. Malinovskýc, and E. Kováþová, *Structural and physical characteristics of plasma enhanced chemical vapour deposition nanocrystalline silicon carbide thin films*, Physics Procedia 32 (2012) 303 – 317.



Chapter 2 Overview of elemental diffusion.

2.1 Introduction.

A diffusion barrier is a material that physically separates two materials of interest so that under some external conditions the unwanted intermixing of the materials is prohibited [2.1]. Nicolet [2.1] discusses the requirements of a good diffusion barrier. A good diffusion barrier should be thermodynamically stable against the adjoining material(s), resistant to thermal stress, have a high thermal and electrical conduction. For these reasons, SiC has been actively used as a diffusion barrier in fuel particles for high-temperature nuclear reactors [2.2]. SiC presents a good candidate to use as a barrier material for application in Si thin film because it does satisfy the above requirements and it is compatible with silicon.

2.2 Effect of contamination from transition metals in Si.

The aim of this thesis is to study the effectiveness of SiC for application as a diffusion barrier against metal contaminants in Si solar cells. Transition metal (TM) impurities are common in Si because of their fast diffusivities [2.3]. In particular, Cu is the most prevalent impurity because of its wide use in electrical wires [2.4] and its relatively high mobility at room temperature [2.5]. Additionally, Istratov *et al.* [2.6] found that other primary contaminants in Si include Fe, Ni, and Cr.

Contaminants are harmful species in the manufacturing process of Si-based devices such as solar cells [2.4, 2.7] and are thought to be one of the major factors contributing to the lifetime

degradation of solar cells [2.6]. Although gettering can reduce the amount of metal contamination in the cells, additional contaminants can be introduced during processing due to the relatively lenient requirements for the cleanliness of the production environment at a typical PV facility [2.6].

G. Coletti *et al.* [2.5] reported that impurities like Fe, Cr, and Ti caused a reduction in the diffusion length and Ni affected the emitter recombination strongly, significantly reducing the solar cell performance. Cu, on the other hand, affected the base-bulk recombination as well as the emitter-bulk recombination.

Istratov *et al.* [2.6] reported that in the samples that they analysed that the impact of transition metals on solar efficiency is not limited on the total metal concentration, but also by the distribution of the profile of the metals in Si. The dominant metal impurities were found to be Fe ($6 \times 10^{14} \text{ cm}^{-3}$ to $1.5 \times 10^{16} \text{ cm}^{-3}$, depending on the material), Ni (up to $1.8 \times 10^{15} \text{ cm}^{-3}$), Co ($1.7 \times 10^{12} \text{ cm}^{-3}$ to $9.7 \times 10^{13} \text{ cm}^{-3}$), Mo ($6.4 \times 10^{12} \text{ cm}^{-3}$ to $4.6 \times 10^{13} \text{ cm}^{-3}$), and Cr ($1.7 \times 10^{12} \text{ cm}^{-3}$ to $1.8 \times 10^{15} \text{ cm}^{-3}$), Cu (less than $2.4 \times 10^{14} \text{ cm}^{-3}$). In all samples, the metal contamination level would be sufficient to degrade the minority carrier diffusion length to less than a micron, if all metals were in an interstitial or substitutional state.

2.2.1 Points defects in crystals.

The arrangement of atoms in crystals may include defects, imperfections, and impurities [2.8]. Defects have a detrimental effect on the properties and the overall behavior of the material. Defects may be created intentionally to produce a set of desired electronic, magnetic, optical,

or mechanical properties [2.8]. However, in most instances, the presence of defects or impurities is not desired. Point defects can be described as localized disruptions in an otherwise perfect crystal structure [2.8, 2.9]. Point defect(s) include either a single atom or a pair of atoms and are different from extended defects such as dislocations or grain boundaries [2.9]. Point defects occur at one or two atomic sites but their inclusion in the material is felt over much larger distances [2.9]. There are three main types of point defects found in crystals: be (a) vacancy, (b) interstitial defect or (c) substitutional defect [2.8, 2.9]

A vacancy is formed when an atom is missing from its normal lattice site in a crystal as depicted in Fig. 2.1 (a). The vacancy disturbs the regular arrangement of atoms and causes an increase in the local strain energy owing to the minor misalignment in the atom positions [2.9]. Vacancies are created by the displacement of atoms from their lattice points in the crystal structure.

The defect is created when, for an example, an impurity atom sits within a gap between crystal lattice points of the host crystal [2.8, 2.9] shown in fig 2.1(b). Interstitial atoms are usually much smaller than the host atoms, but if it is larger than the interstitial site, it compresses and distorts the surrounding crystal lattice.

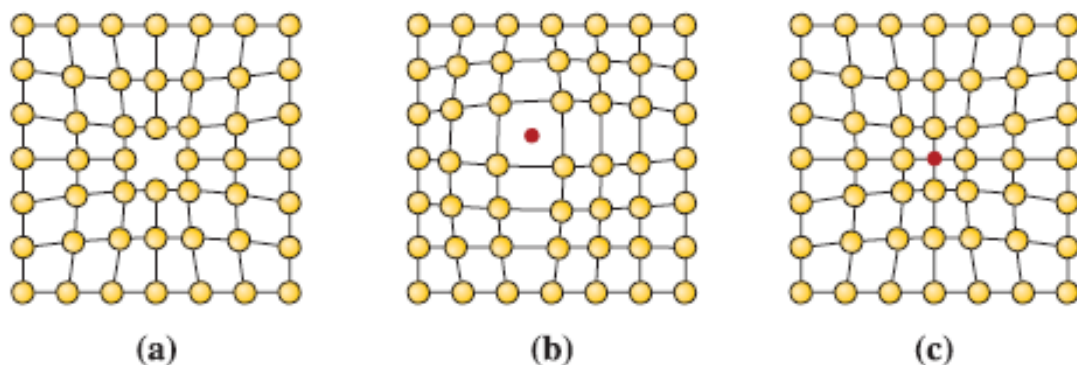
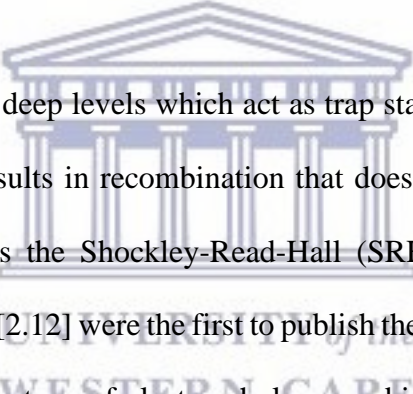


Figure 2.1: Point defects: (a) vacancy, (b) interstitial atom, and (c) substitutional atom.

A substitutional defect is created when one atom from the host crystal is replaced by a foreign atom. Substitutional atoms may be larger than the host atoms in which case the surrounding interatomic spacing is reduced or they can be smaller and this results in the surrounding interatomic spacing to increase as shown in fig. 2.1 (c). In either case, the substitutional defects disturb the surrounding crystal structure and cause a local increase in the lattice strain energy [2.9]. Substitutional defects can be introduced into the material either as an impurity or as a deliberate alloying addition.

2.2.2 Shockley Read Hall recombination.



Impurities or defects introduce deep levels which act as trap states in the bandgap of the host material [2.10 – 2.11]. This results in recombination that does not occur from band to band transition and is referred to as the Shockley-Read-Hall (SRH) [2.10]. William Shockley, William Read, and Robert Hall [2.12] were the first to publish the theory of SRH recombination mechanisms. Fig. 2.2 shows the type of electron-hole recombination that is facilitated by an impurity or lattice defect. The electron that has been previously promoted in the conduction band, relaxes to such a deep state from where it recombines with the hole that was left in the valence band. Table 2.1 shows trap states of point-like defects in c-Si, e.g. Fe produces a donor deep trap at $E_v + 0.33$ eV in the bandgap of Si and thus increasing the recombination of minority charge carriers [2.10]. Although this type of recombination is less common, it is the most dominant in semiconductors at operational conditions. It is usually nonradioactive and the excess energy is converted into heat [2.10].

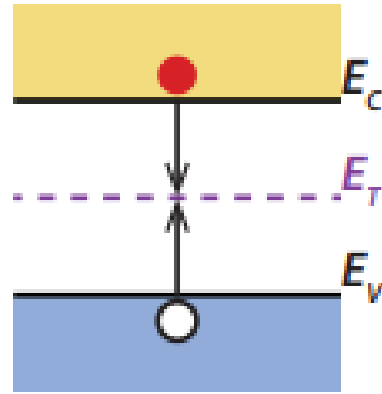


Fig 2.2: A schematic illustration of an an energy level band diagram.

Table 2.1: Energy levels of active deep level point-like metal impurities in crystalline silicon at RT [2.13].

Impurity	RT lattice site	Type	Group	Energy (eV)
Ti	Interstitial	Donor	4	$E_C - 0.27$
Cr	Interstitial	Donor	6	$E_V - 0.22$
Mo	Interstitial	Donor	6	$E_V + 0.28$
Fe	Interstitial	Donor	8	$E_V + 0.38$
Au	Substitutional	Acceptor	11	$E_C - 0.55$
Zn	Substitutional	Acceptor	12	$E_V + 0.33$

The lifetime of minority carriers ($\tau_{n,SRH}$) in p-type semiconductor and minority carriers ($\tau_{p,SRH}$) in an n-type semiconductor are given by;

$$\tau_{p,SRH} = \frac{1}{c_p N_T} \quad \text{and} \quad \tau_{n,SRH} = \frac{1}{c_n N_T} \quad (2.1)$$

where C_n , C_p is the electron and hole capture cross section, respectively and N_T is the trap density. In essence, the lifetime of the minority carriers due to SRH recombination is inversely proportional to the trap density. Therefore, the more trap states there are, the greater the recombination leading to lifetime degradation of minority carriers. This has the overall effect of decreasing the short circuit deliverable current. From this model it can be deduced that in order to increase the short circuit deliverable current in a Si intrinsic layer in solar cells, metal diffusion must be restricted or lowered, thus enhancing the total efficiency in solar cells.

2.2.3 Impact of silver impurities on electronic transport in Si.

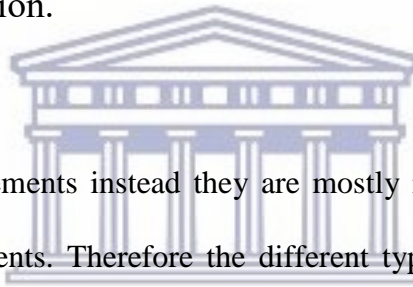
Adegboyeda *et al.* [2.14] used the four-point probe and minority carrier measurements to investigate the effects of varying Ag impurity concentration levels on the electrical characteristics of p-type float-zone silicon. They reported that Ag atom concentration in the range of 10^{14} to 10^{15} led to the reduction in the lifetime of minority carriers by forming deep-level traps in the material. The incorporation of Ag impurities in the Si substrates showed a detrimental effect on the minority carrier lifetimes. Ag impurity concentration of about 7.5×10^{14} and $1.5 \times 10^{15} \text{ cm}^{-3}$ reduced the lifetime value from 18.40 to 0.23 μs and 0.13 μs respectively. This reduction was attributed to the presence of Ag related traps.

2.3 Diffusion mechanism.

Diffusion of atoms is mediated by defects as well as imperfections in the crystal. It is governed by Fick's laws. Atoms in crystals are in constant oscillations around their equilibrium or lattice

positions [2.14]. When these oscillations are large enough, the result is a displacement of atoms from their lattice positions. This movement can only occur when the atom overcomes the potential energy barrier between itself and its neighbors. The moving atoms collide with other atoms that are also displaced from their sites. The overall migration, in an inhomogeneous material, exhibits an observable drift from high concentration to low concentration region; this process is referred to as diffusion. Diffusion is thus an atomic transport mechanism, which is dependent on the concentration gradients and it leads to changes in the physical and chemical properties of materials.

2.3.1 Fick's laws of diffusion.



Materials are seldom pure elements instead they are mostly in alloy forms, compounds or variant combinations of elements. Therefore the different types of ions or atoms within a material will most likely move i.e. diffuse as a response to the difference in their bulk concentration. The rate of diffusion is dependent on the concentration gradient as well as on the temperature [2.8]. Diffusion plays a critical role in material fabrication, there is a whole range of technologies that make use of the enhancement or restriction of diffusion. Examples of applications where diffusion plays a central role are carburization where carbon is introduced into steel in order to increase its hardness [2.8] and the diffusion of dopant atoms into intrinsic semiconductors in order to create the p-n junction for photovoltaic and thin film transistor applications.

Adolf Eugen Fick was the first scientist to present a quantitative description of the random movement of atoms by adapting mathematical equations of heat conduction derived by Fourier [2.8, 2.15], to the equations of matter transport. According to Fick, in an isotropic material, the

rate of transfer of the diffusing atoms through a cross-section area is proportional to the concentration gradient measured along the normal of the cross section, i.e.

$$J = -D \frac{dC}{dx} \quad (2.2)$$

where J is the flux, C the concentration in $\frac{\text{atom}}{\text{cm}^3}$ of the diffusing substance, x the space coordinate in cm , and D is the diffusion coefficient in $\frac{\text{cm}^2}{\text{s}}$ of the diffusing substance. The negative sign in eq. 2.2 is due to the fact that the flux of the diffusing species occurs in the direction opposite to that of increasing concentration, i.e. from a region of higher to lower concentration. Eq. 2.2 is known as Fick's first law.

The diffusion coefficient D of a substance depends on various factors such as the crystal structure, the composition of the matrix through which it is diffusing and the temperature [2.8].

The temperature dependence of D follows an Arrhenius relation:

$$D = D_0 \exp\left(\frac{-Q}{kT}\right), \quad (2.3)$$

where D_0 is the pre-exponential factor, Q is the activation energy (eV), k is the Boltzmann's constant (eV/K) and T is the absolute temperature in Kelvin (K).

Fick's first law assumes a constant concentration gradient over time. However, in most cases where diffusion takes place, both the concentration profile and gradient changes with time and thus eq. (2.2) is modified into the second law of Fick. The continuity requirement dictates that $\partial C / \partial t = -\partial J / \partial x$; when this is inserted in eq. (2.2), the second Fick law follows [2.8],

$$\frac{\partial c}{\partial t} = D \frac{\partial^2 c}{\partial x^2}, \quad (2.4)$$

2.3.2 Diffusion mechanisms.

Solids are susceptible to a variety of defects, e.g. point, planar and complex defects that are caused by dislocation or stacking faults [2.8] and clustering of point or planar defects [2.8], respectively. Defects influence the net observable diffusion in crystals. Diffusion mechanisms have been a subject of intense studies [2.16 - 2.18]; in this section, we give an overview of different mechanisms of diffusion, which is adapted to Ag in SiC. Silver can diffuse through vacancies and interstitial states in the SiC layer as well as through grain boundaries if the film is polycrystalline. Each mode will depend on the annealing temperature [2.13]. The annealing temperature capable of yielding vacancies is normally high while diffusion mediated by interstitials can happen at a lower temperature. The mobility of these self-interstitials defects is expected to be greater than vacancies Si in general and in SiC in particular, however, the stable nature of SiC interstitials [2.19] suggests only a few diffusion pathways. Rollert *et al.* [2.20] have shown by means of neutron activation analysis (NAA) on Ag implanted specimens that Ag interstitials are the most frequently observed in dislocation-free Si. Alternatively, *ab initio* simulations on SiC by Schrader *et al.* [2.20] suggested that Ag will most likely be found in the defect clusters on a Si sub-lattice site coupled with a C vacancy ($Ag_{Si} - V_C^{-1}$).

2.3.2.1 Self diffusion mechanism.

Fig 2.3 depicts a scenario in which a neighboring atom moves from its normal lattice position into the vacancy thus creating a vacancy behind. The atom is said to have diffused via a vacancy mediated self diffusion mechanism. During this process, the vacancy appears to have also moved in the opposite direction of the motion of the atoms [2.21]. In the schematic, fig. 2.3(a)

and fig. 2.3 (b) show the position of the vacancy before and after diffusion respectively (the atom on the right side filled the vacancy). The solid and dotted circles represent the atom and the vacancy respectively.

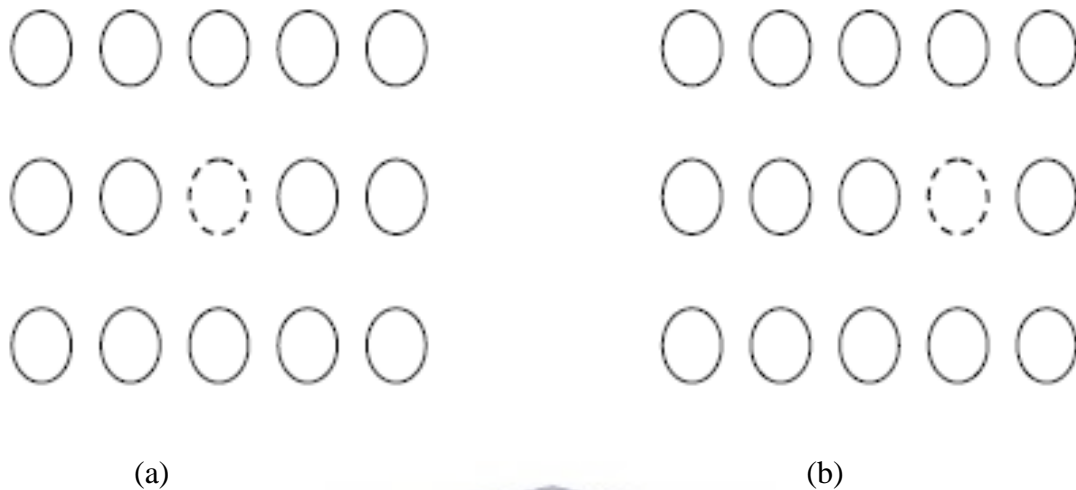


Figure 2.3: Schematic representation of self-diffusion [2.21].



2.3.2.2 Substitutional diffusion mechanism.

In this diffusion mechanism, a foreign diffusing atom substitutes a host atom by displacing it from its lattice site [2.8]. This is a high activation energy process. A straight-forward swapping of atoms requires a great deal of energy, as the swapping atoms would need to physically push the host atoms out of the way in order to swap places. In practice, substitutional diffusion occurs only if a vacancy is present. The number of vacancies, which increases as the temperature increases, influences the extent of both self-diffusion and diffusion of substitutional atoms.

2.3.2.3 Interstitial diffusion mechanism.

Fig. 2.4 depicts a situation in which the diffusing atom or ion moves from one interstitial position to the next. Fig 2.4 (a) presents the situation before diffusion and fig. 2.4 (b) presents a situation after interstitial diffusion; the dark filled circle represents the interstitial diffusing species and the white hollow circle represents the host atoms. No vacancies are required for this mechanism to proceed. Partly because there are more interstitial sites than vacancies, interstitial diffusion occurs more easily, at low temperature, than self-diffusion and substitutional diffusion. Interstitial atoms that are relatively smaller can diffuse faster.

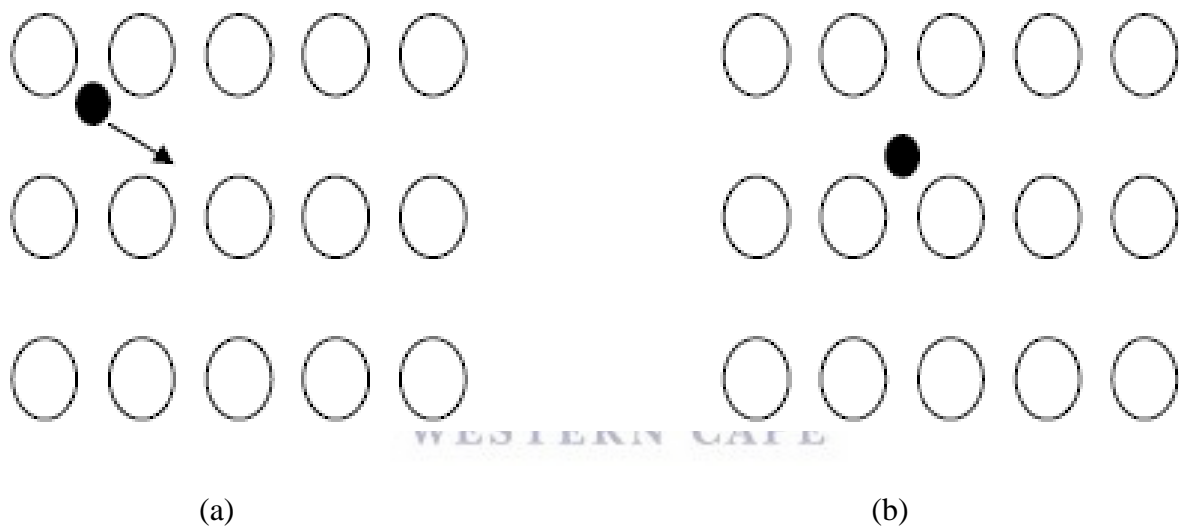


Figure 2.4: (a) before and (b) and after interstitial diffusion [2.21].

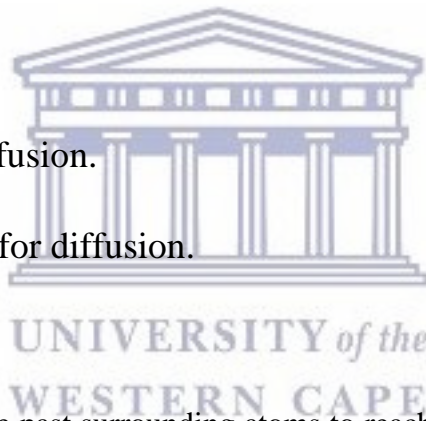
2.3.2.4 Grain boundary diffusion mechanism.

The motion of atoms in solids is not limited to the inside of crystals, diffusion processes also occur on the surface and along the boundaries of crystalline grains. A grain boundary can be defined as the interfacial transition region between two grains in a polycrystalline material in

contact with each other but differ in crystallographic orientation [2.22]. Grain boundary diffusion is the process of atomic transport along grain boundaries in polycrystalline materials. Research reports [2.23] has shown that diffusion is faster along grain boundaries because more open structure is found at grain boundaries as well as at exterior of surfaces. It is reasonable to assume that atoms should transport easier on the surface and with more difficulty in grain boundaries whereas it would require the highest energy in the interior of the crystals. Grain boundaries are highly disordered, and it can be stated that they provide “open” medium for diffusion in comparison with other mechanisms. The density of grain boundaries is particularly high in polycrystalline thin films most likely due to grain boundary diffusion being the dominant transport mechanism in these structures at relatively low temperature.

2.3.3 Factors affecting diffusion.

2.3.3.1 Activation energy for diffusion.



A diffusing atom must squeeze past surrounding atoms to reach its new site. In order for this to happen, energy must be supplied to allow the atom to move to its positions. In order to move to a new location, the atom must overcome an energy barrier. The thermal energy provides atoms or ions with the necessary energy needed to exceed this barrier. Normally, less energy is required to squeeze an interstitial atom past the surrounding atom; consequently, activation energies are lower for interstitial diffusion than for self-diffusion or substitutional diffusion.

2.3.3.2 Temperature and the diffusion coefficients.

Covalently bonded materials, such as carbon and silicon, have unusually high activation energies, consistent with the high strength of their atomic bonds. When the temperature of a material increases, the diffusion coefficient D increases and, therefore, the flux of atoms increases as well. At higher temperature, the thermal energy supplied to the diffusion atoms permits the atoms to overcome the activation energy barrier and to move more easily to a new site. At low temperature, e.g. below 0.4 times the absolute melting temperature of the material, diffusion is very slow and may not be significant.

2.3.3.3 Type of diffusion.

In volume diffusion, the atoms move through the crystal from one regular or interstitial site to another. Because of the surrounding atoms, the activation energy is large and the rate of diffusion is relatively slow. Atoms can also diffuse along boundaries, interfaces, and surfaces in the material. Atoms diffuse easier through grain boundaries because the atom packing is disordered and less dense in the grain boundaries. For this reason, the required activation energy is lower in diffusion mediated by grain boundaries. Surface diffusion is the easiest because there are even fewer constraints on the diffusing atoms at the surface.

Table 2.2 shows the dependence of the diffusion rate on some of the structural properties of the material.

Table 2.2: Factors influencing the speed of diffusion rate in materials [2.24].

Diffusion is faster in	Diffusion is slower in
Open crystal structures	Close-packed structures

Lower melting temperature materials	Higher melting temperature materials
Materials with secondary bonding	Materials with covalent bonding
Smaller diffusing atoms	Larger diffusing atoms
Cations	Anions
Lower density materials	Higher density materials

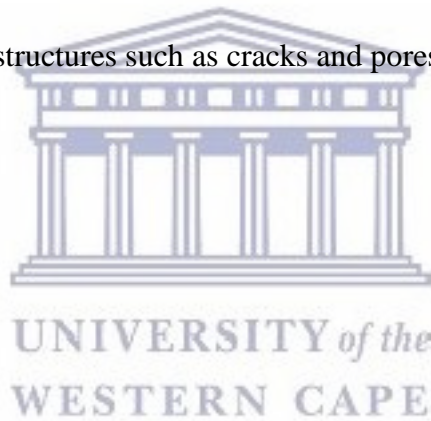
2.4 Nature of silver defects contributing to diffusion in SiC.

The nature of implantation-induced point defects for the Ag-SiC system is not explicitly known [2.25] and as such, there exists inconsistency in various published results. Friedland *et al.* [2.26] investigated Ag transport in implanted SiC substrates employing RBS depth profiling. The implanted substrates were heat treated under isothermal and isochronal annealing conditions. Ag diffusion was observed after isothermal annealing of 10 h at 1300 °C in both polycrystalline and single crystalline SiC and this was said ascribed to implant radiation damage. There was no additional annealing noticeable in the monocrystalline SiC substrate when the annealing time was extended further than 10 h. However, reduced diffusion was detected in the polycrystalline SiC substrates and was attributed to the presence of grain boundaries (GBs). This posited that in single crystalline SiC the Ag is initially embedded in amorphous SiC network, whereas in the polycrystalline SiC it is surrounded by polycrystalline matter containing a relatively high density of extended defects. The conclusion drawn was that diffusion is enhanced in defective or amorphous SiC and that most of the damage is repaired after annealing for 10 h.

A similar study to Friedland *et al.* [2.26] was done by Gerzack *et al.* [2.25] where the effects of isochronal and isothermal annealing on Ag implanted monocrystalline and polycrystalline SiC substrate were investigated, using SIMS depth profiling technique. Under isochronal annealing conditions, the as-implanted (AI) single crystal substrates spectra showed a singular Ag concentration peak with a skewed Ag concentration past the primary implantation peak into the bulk substrate from the expected ion straggling. The thermally treated substrates indicated a bi-modal Ag distribution with no significant variation in the Ag concentration profile past the primary implantation peak. The isothermally treated substrates exhibited the same behaviour and that was suggestive of the fact that Ag distribution in single crystal substrates was independent of annealing temperature or exposure time probed in their study. The redistribution of Ag past the primary implantation peak is owed to the annealing-out of a finite population of implantation induced defects in the substrates. The energetics of residual defects formed by the implantation process suggests that excess point defects, notably Si and C vacancies and Si self-interstitials were available in the substrates to contribute to the Ag diffusion process post implantation [2.25]. Additionally, they suggested that the correlation of the damage profile with bi-modal Ag redistribution indicated the non-equilibrium interstitial point defects, which remain after ion implantation, contribute to the observed diffusion of Ag in mono-crystalline SiC. This was consistent with a previous ion-implantation study by Xiao *et al.* [2.27] that reported that implanted Ag exists interstitially after implantation at 377 °C as determined by RBS channelling experiments. Shrader *et al.* [2.28] *ab initio* studies suggested that the fastest diffusion mechanism for Ag in bulk SiC was found to be that of Ag interstitials. Bulk diffusion is limited by high migration barriers for the most stable Ag defects and the inability of Ag to reach the faster diffusing interstitial state due to the high formation energy of interstitial [2.28]. In polycrystalline 3C-SiC substrates, Gerzack *et al.* [2.25] observed that Ag concentration was observed to penetrate into the SiC with increasing exposure temperature. Under isothermal

annealing conditions Ag penetration into bulk SiC also increased as a function of time. These observations suggested that Ag penetration into the bulk is due to a thermal transport mechanism. In polycrystalline 3C-SiC substrates, GBs act as Ag impurity sinks to the mobile implanted Ag defects during the initial stages of thermal annealing. The presence of GBs facilitates diffusion, i.e. grain boundary diffusion is more significant than impurity lattice diffusion. Other microstructural variables may contribute to the observed diffusion, including differences in dislocation density, stacking fault density, and extrinsic defect populations [2.25].

Contradictory observations were made by MacLean [2.29] whereby Ag did not diffuse in polycrystalline SiC. Thus, he proposed that the dominant method of Ag in SiC might be vapour transport through mechanical structures such as cracks and pores.



References.

- [2.1] M. A. Nicolet, *Diffusion barriers in thin films*, Thin Solid Films 52(3) (1978) 415–443.
- [2.2] E. Friedland, J.B. Malherbe, N.G. van der Berg, T. Hlatshwayo, A.J. Botha, E. Wendler, and W. Wesch, *Study of silver diffusion in silicon carbide*, Journal of Nuclear Materials 389 (2009) 326–331.
- [2.3] L. Zhong and F. Shimura, *Substitutional diffusion of transition metal impurities in Si*, Japan. Journal of Applied Physics. 32 (1993) 112 – 1116.
- [2.4] K. Matsukawa, K. Shirai, H. Yamaguchi, and H. Katayama-Yoshida, *Diffusion of transition-metal impurities in silicon*, Physics B: Condensed Matter 402 (2007) 151–154.
- [2.5] G. Coletti, P. C. P. Bronsveld, G. Hahn, W. Warta, D. Macdonald, B. Ceccaroli, K. Wambach, N. L. Quang, and J. M. Fernandez, *Impact of metal contamination in Si solar cells*, Advanced Functional Materials 21 (2011) 879-890.
- [2.6] A. A. Istratov, T. Buonassisi, R. J. Mcdonald, A. R. Smith, L. Berkeley, and C. Road, *Metal content of multicrystalline silicon for solar cells and its impact on minority carrier diffusion length*, Journal of Applied Physics 94(10) (2003) 6552–6559.
- [2.7] R. Czaputa, *Transition Metal Impurities in Silicon: New Defect Reactions*, Applied Physics A, 49 (1989) 431-436.
- [2.8] D.R. Askeland, P.P. Fulay, and W.J. Wright, *The science and engineering of materials*, Cengage learning: Stanford, 2010.
- [2.9] A. P. Mouritz, *Introduction to Aerospace materials*, Elsevier, 2009.

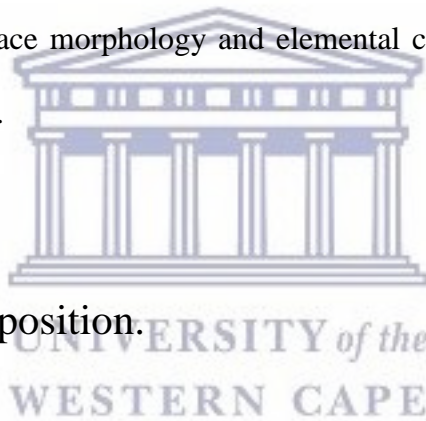
- [2.10] D. Macdonald, *Recombination activity of interstitial iron and other transition metal point defects in p- and n-type crystalline silicon*, Applied Physics Letters 85(18) (2004) 4061–4063.
- [2.11] K. Jager, O. Isabella, A. H. M. Smets, R. A. C. M. M. van Swaaij, and M. Zeman, *Solar energy fundamentals system*, Delft University of Technology, 2014.
- [2.12] W. Shockley and W. T. Read, *Statistics of the Recombination of Holes and Electrons*, Physics Review 87(469) (1952) 835–842.
- [2.13] [2.20] M. Bockstedte, M. Heid, A. Mattausch, O. Pankratov, *The Nature and Diffusion of Intrinsic Point Defects in SiC*, Material science Forum 389–393 (2002) 471–476.
- [2.14] Adegboyega G.A. and Poggi A, *Copper impurities and their annealing behaviour in FZ silicon*, Physica Status Solidi (a) 143 (1994) 373.
- [2.15] J. Crank, *The mathematics of diffusion*, Claredon press, 1975.
- [2.16] R.M. Cohen, *Point defects and diffusion in thin films of GaAs*, Material science and engineering reports R: R20 (1997) 167 – 280.
- [2.17] E.G. Seebauer, M. C. Kratzer, *Charged point defects in semiconductors*, Materials science and engineering Reports: R55 (2006), 57 – 149.
- [2.18] A.V. Ven, H. Yu, G. Ceder, and K. Thornton, *Vacancy mediated substitutional diffusion in binary crystalline solids*, Progress in material sciences 55 (2010) 61 -105.
- [2.19] T. J. Gerczak, B. Leng, K. Sridharan, J. L. Hunter, A. J. Giordani, and T. R. Allen, *Observations of Ag diffusion in ion implanted SiC*, Journal of Nuclear Materials 461 (2015) 314–324

- [2.20] Rollert F., Stolwijk N.A. and Mehrer H, *Solubility, diffusion and thermodynamic properties of silver in silicon*, Journal of Physics D: Applied Physics 20 (1987) 1148.
- [2.21] T.T. Hlatshwayo, *Diffusion of silver in 6H-SiC*, Ph.D. Thesis, Department of Physics, University of Pretoria, 2010.
- [2.22] I. Kaur, Y. Mushin and W. Gust, *Fundamentals of grain and interphase boundary diffusion*, New York: John Wiley and Sons, 1995.
- [2.23] D. Turnbull, *Grain Boundary and Surface Diffusion*, Trans. A.S.M., 43A (1951) 129.
- [2.24] K. J. Pondo, *In-situ real-time backscattering spectrometry study of Ni/Ge interaction*, M.Sc. Thesis, Department of Physics, University of Zambia, 2010.
- [2.25] T. J. Gerczak, B. Leng, K. Sridharan, J. L. Hunter, A. J. Giordani, and T. R. Allen, *Observations of Ag diffusion in ion implanted SiC*, Journal of Nuclear Materials 461 (2015) 314–324
- [2.26] E. Friedland, J.B. Malherbe, N.G. van der Berg, T. Hlatshwayo, A.J. Botha, E. Wendler, and W. Wesch, *Study of silver diffusion in silicon carbide*, Journal of Nuclear Materials 389 (2009) 326–331.
- [2.27] X.Y. Xiao, Y. Zhang, L.L. Snead, V. Shutthanandan, H.Z. Xue, and W.J. Weber, *Near-surface and bulk behavior of Ag in SiC*, Journal of Nuclear Materials 420 (2012) 123–130.
- [2.28] D. Shrader, S. M. Khalil, T. Gerczak, T. R. Allen, A. J. Heim, I. Szlufarska, and D. Morgan, *Ag diffusion in cubic silicon carbide*, Journal of Nuclear Materials 408 (2011) 257–271.
- [2.29] H.J. MacLean, *Silver Transport in CVD Silicon Carbide*, Ph.D. Thesis, Department Of Nuclear Engineering, MIT, Boston, 2004.

Chapter 3: Experimental methods and characterisation techniques.

3.1 Introduction.

Electron beam evaporation was used to deposit SiC films on Si (100) substrates from a commercial high purity hot pressed SiC sheet. The films were subsequently implanted with Ag ions. Before implantation, computer simulations were done to predict the distribution profile of Ag ions in SiC. The samples were then characterized for elemental and compositional analysis using RBS. The surface morphology and elemental composition were investigated using SEM/EDX, respectively.



3.2 Physical vapour deposition.

Physical vapour deposition, PVD, is a method in which atoms are transported by physical means to the substrate, i.e. no chemical reaction takes place [3.1] during the deposition. Two commonly used methods of PVD are evaporation and sputtering. PVD differ from CVD where a chemical reaction occurs at a surface during thin film deposition [3.1].

At equilibrium, the flux of atoms that transition from solid/liquid to vapour is the same as the flux of atoms that transition from vapour to liquid/solid at the surface of the source. The flux of evaporated atoms from the source material is given by the following relation [3.1],

$$Z = 3.51 \times 10^{22} \frac{P}{\sqrt{MT}} \quad (3.1)$$

where M is the molecular weight, P is the pressure and T is the temperature. Fig. 3.1 shows a schematic diagram of distances and angles for deposition, in which the angles are measured perpendicularly from to the source and substrate respectively. The distance from the source to the substrate is denoted by r , the angle from the source is given by Φ , and the substrate angle is given by Θ . The flux calculation in eq. 3.1 is only valid at the source and in a real application the substrates are a considerable distance from the source as shown in fig. 3.1. This means that the rate of deposition at the substrate will be less than the rate of evaporation at the source. As a result, the standard kinetic theory must be used to determine the flux at the substrate. For a flat substrate whereby $\Theta = 0$ the flux of atoms at the substrate is given by

$$Z_{dep} = R_{sec} \frac{\cos(\Phi)}{r^2} \quad (3.2)$$

where R_{sec} is the rate at which the molecules leave the source in units of molecules/second. The flux has units of molecules/cm².

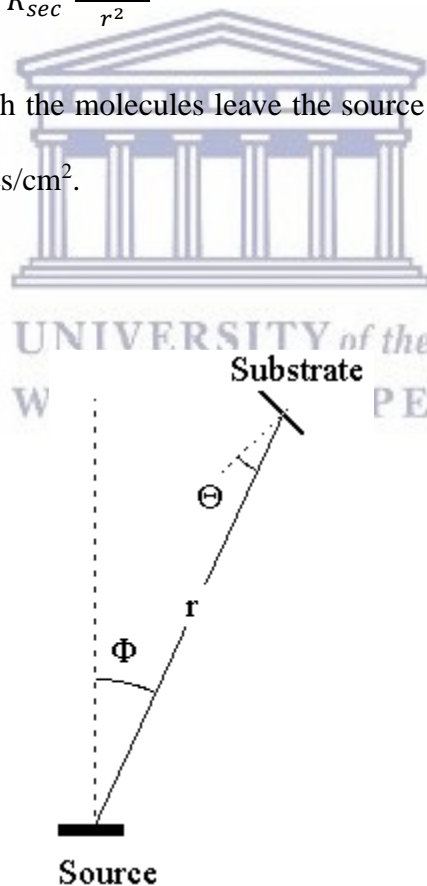


Figure 3.1: Schematic diagram describing distances and angles during a typical physical deposition technique.

3.2.1 Preparation and sample deposition.

A Si (100) wafer was cut into approximately 1 cm x 1 cm substrates. The substrates were ultrasonically bathed in acetone to remove organic contaminants followed by methanol for 5 minutes in each. Thereafter, they were dipped in 5% HF solution, one by one, for 60 seconds to get rid of the native SiO₂ and air dried. SiC films were deposited at a rate of 0.6 ($\frac{\text{Å}}{\text{s}}$) using electron beam evaporator with a base pressure better than 10⁻⁵ mbar. The deposition was done at iThemba LABS, Cape Town. The films were implanted with energetic Ag ions at iThemba LABS, Gauteng.

During electron beam evaporation, a high energy electron beam is generated from a thermionic-emitting filament. A high voltage is used to accelerate the electron beam from the filament to the target material where it is brought to focus by the presence of an electric and magnetic field [3.2 – 3.3]. Upon impingement, the source is evaporated in vacuum and surface atoms leave the surface and deposit on the substrate positioned above the evaporating source. The electron beam can be rastered across the source surface to produce heating over a large area.

The pressure in the deposition chamber must be kept at 3.0 x 10⁻⁴ mbar or lower [3.2]. This is because the pressure in the chamber must be low enough so that the mean free path is longer than the distance between the electron beam and the substrate. The mean free path is the average distance an atom or molecule can travel, in the chamber, before colliding with another particle thereby disturbing its motion [3.2].

Fig. 3.2 shows a schematic illustration of a typical high vacuum system used for electron beam evaporation of thin films [3.4]. There three crucibles into which elements to be evaporated are loaded. The positions of the crucibles can be moved from the outside so that each of the three

crucibles can be placed in the path of the electron beam. The electron beam supplies heat to the crucibles. Electrons are supplied by the electron gun. The filament current can be varied consequently changing the electron beam current which in turn alters the rate of deposition. Sample holders, each of which takes up to seven samples, are loaded face down on a rotating platform which can take up to six sample holders. A quartz monitor was used to determine the deposition rate as well as the thicknesses of the evaporated films. All depositions were done in a vacuum. The vacuum was maintained by means of ion pumps, sublimation pumps, cryopanel, and the turbo molecular pump. The upper section contains the sample holder, the thickness monitor, and the electron gun. The baffle valve is closed to ensure that the lower section of the system is maintained under vacuum when the system is not in use or during sample changing.

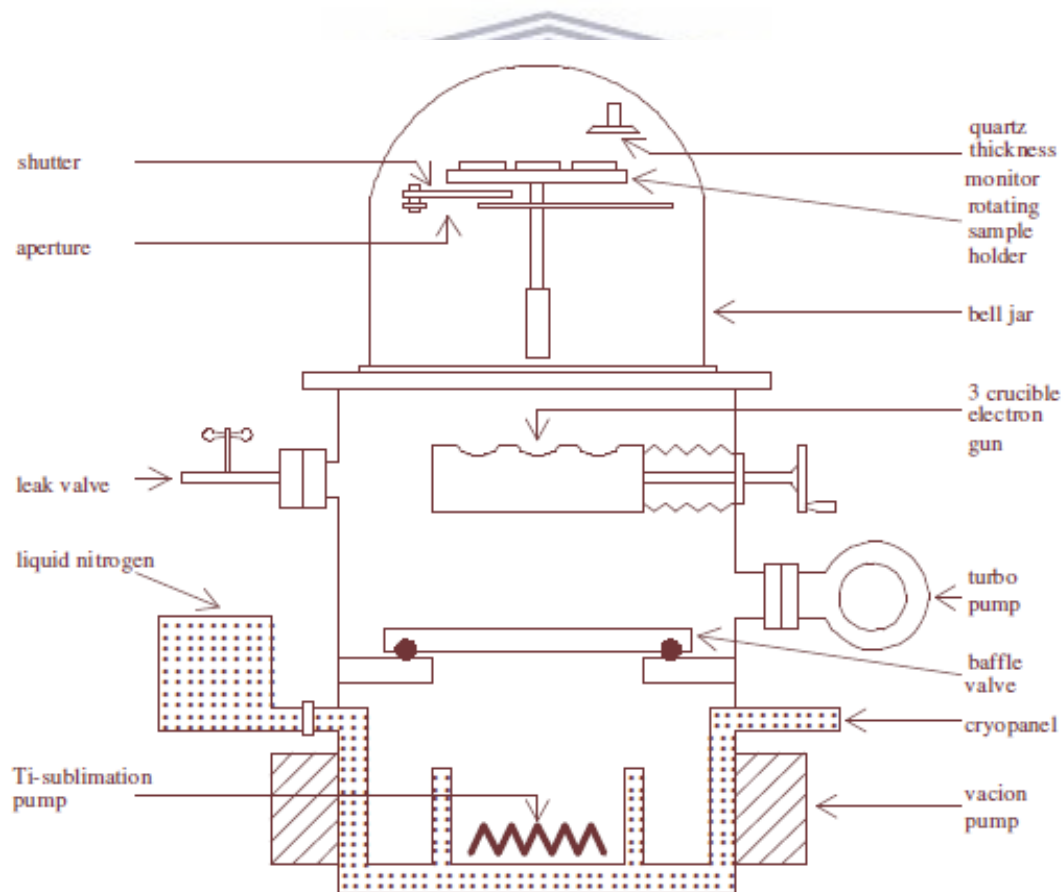


Figure 3.2: Schematic illustration of a typical high vacuum system used for electron beam evaporation of thin films [3.4].

3.3 Elementary principles governing ion implantation.

3.3.1 Introduction.

When you bombard a solid target with an energetic ion beam, the ions penetrate the material, slow down by transferring part of their energy to the target atoms and electrons and eventually stop at a certain depth below the surface [3.5– 3.7]. This process is known as ion implantation. The energy loss mechanism is a result of the elastic and inelastic collisions of the ions with target atoms and electrons [3.5 – 3.7]. Ion implantation is commonly used in the manufacturing of semiconductors and various material doping processes [3.7]. During ion implantation, the fluence, the total amount of implanted atoms, and the depth can be controlled with precision [3.7]. The drawback of ion implantation is radiation damage; the material can, however, recover by subsequent thermal processing [3.5, 3.7 - 3.8].

The fluence for singly charged ions is related to the beam current, implantation time and the ion beam scattering by:

$$\text{Fluence } (\Phi) = \frac{\left(\frac{\text{Ion beam current in amps}}{q}\right) \times (\text{Implantation time})}{[\text{Ion beam scattering area}]} = \frac{\# \text{ atoms}}{\text{cm}^2} \quad (3.3)$$

During ion implantation, it is important to know the final distribution of the ions in the target [3.5, 3.8]. All the processes involved until the ions come to a stop must be well understood. Thus, this section details the most important processes that occur during ion implantation.

3.3.2 Stopping power.

Energy loss in materials is an important mechanism that influences the profile of implanted ions in the material. When ions penetrate into a target, they lose energy through a series of collisions with the atoms and the electrons of the target. The spatial rate of energy loss of incident ions is called the stopping power of the target material and it is due to two contributions: the two additive terms as in eq. 3.4.

$$S = \frac{dE}{dx} = \left(\frac{dE}{dx}\right)_n + \left(\frac{dE}{dx}\right)_e = S_n + S_e \quad (3.4)$$

The nuclear stopping power S_n is due to collisions between the incident ions and the target nuclei. Upon collision, the incoming ion transfers part of its energy to the target nuclei inducing its displacement. The electronic contribution, S_e is due to an energy transfer from the ion to the target electrons, which results in the excitation or ionization of the target atoms, or excitation of conduction or valence band electrons.

To calculate the stopping power using eq. 3.4 the sample density is required. The densities of thin films are hardly known with precision, the accurate values of S in thin films are thus difficult to calculate. Therefore, the stopping cross-sections must be used to replace S . The stopping cross section is the energy loss per atom and does not require the density. It can be obtained by dividing S with the target density N' :

$$\mathcal{E} = - \frac{dE}{N' dx} \quad (3.5)$$

From eq. 3.5 the penetration length R of ions with incident energy E_0 can be derived;

$$R = \frac{1}{N} \int_0^{E_0} \frac{dE}{dx} \quad (3.6)$$

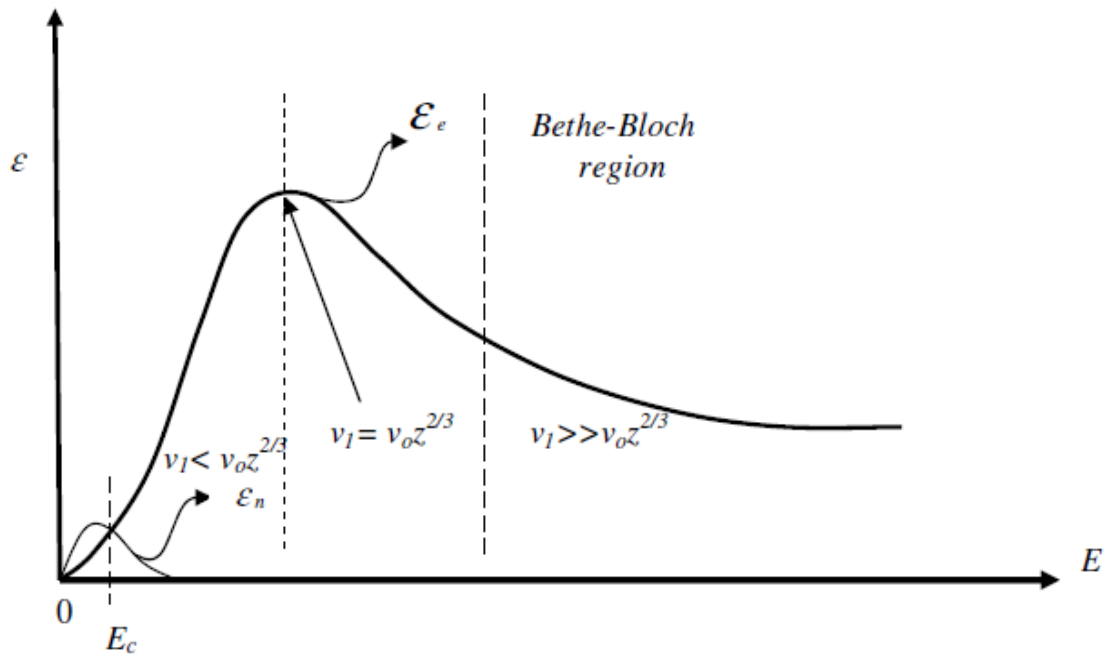


Figure 3.3: The dependence of nuclear (\mathcal{E}_n) and electronic (\mathcal{E}_e) contributions to the stopping cross section \mathcal{E} as a function of ion energy E .

Fig. 3.3 shows the dependence of the nuclear and electronic contributions to the stopping cross section as a function of E . V_0 is the Bohr velocity ($V_0 = q^2/4\pi\epsilon_0\hbar$) and Z is the atomic number of the incident ion. Nuclear collisions predominate at low energies and electronic collisions at high energies. Electronic stopping power starts to dominate above the critical energy \mathcal{E}_c , where the velocity of the ${}^4\text{He}^+$ ion is equal to the average orbital velocity of the electron, then reaches a maximum and decreases at a very high energy region or Bethe – Bloch region. This decrease in the electronic stopping power is caused by the short amount of time that the ion has to interact with the electrons of the target atoms due to its high velocity.

3.3.3 Energy loss in compounds.

If the target is a compound A_mB_n of two different elements A and B then the total stopping power can be found by a simple additive rule, eq. 3.7. This rule assumes that the interaction between the ions and the target atoms are independent of the physical and chemical state of the medium. For a compound consisting of different elements i with atomic concentrations c_i ($\sum_i c_i = 1$) the total stopping power S is given by;

$$S = \sum_i c_i S_i \quad (3.7)$$

where S_i is the stopping power of each element. The stopping cross sections of element A and B are written as ε^A and ε^B respectively, thus total stopping cross section is given by;

$$\varepsilon^{A_mB_n} = m\varepsilon^A + n\varepsilon^B \quad (3.8)$$

where m and n are the relative molar fractions of the compound materials. Equations 3.7 and 3.8 are equivalent and they are known as Bragg's rule [3.9]. Bragg's rule assumes that the interaction between the ion and the atom is independent of the environment. However, the chemical and physical state of the medium is observed to have an effect on energy loss leading to a deviation from Bragg's rule predictions. Deviations are most pronounced around the stopping power maximum and for solid compounds such as oxides, nitrides, and hydrocarbons. The core and bonds model (CAB) by Zeigler and Manoyan [3.10] was developed to address these deviations. The CAB model assumes that the electronic energy loss has two contributions; the effect of atomic cores and the effect of atomic bonds such as C-H and C-C. The CAB model allows for better predictions of the stopping cross section in compounds, but the detailed target bond structure has to be known.

3.3.4 Energy straggling.

When a beam of charged particles penetrate matter, the slowing down is accompanied by a spread in the beam's energy and this is referred to as energy straggling. It is a result of statistical fluctuations of the energy transfer during collisions. This implies that identical ions with the same initial energy no longer have the same energy after traversing a distance Δx in the same medium because the energy loss is subjected to fluctuations. The ion forms a zigzag path in the film due to statistical fluctuations and multiple scattering events of the ion by the target atoms. Essentially, the statistical fluctuations lead to ions being implanted at various depths.

The range of the i^{th} ion is the total distance it travels before coming to a halt. The total range, taking all effects into account, is given by;

$$R_{TOT} = \sum l_i \quad (3.9)$$

where l_i is the different paths taken by the ion in the solid. Fig. 3.4 shows a schematic of two charged particles penetrating a material; one with high energy and the other with low energy, are shown. The ion with high energy exhibits a straight line path in the beginning due to electronic stopping, while at the end it tends to form a zigzag path due to nuclear stopping. For the low energy ion, the path is zigzag from the onset because both the magnitude of the electronic and nuclear stopping both have a noticeable influence.

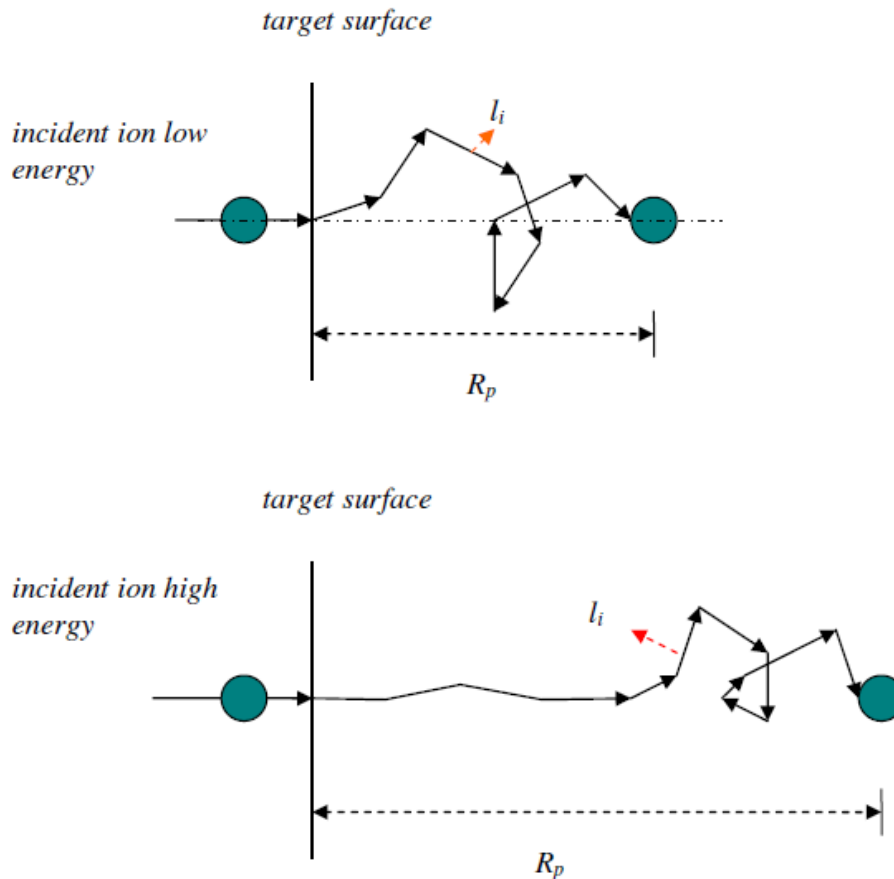
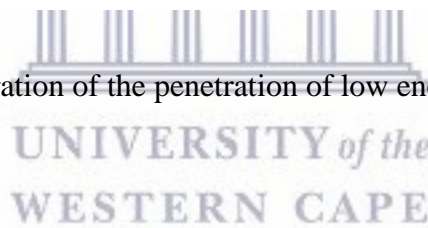


Figure 3.4: A schematic illustration of the penetration of low energy ion (top) and high energy ion (bottom) [3.8].



The projected range, R_p , is the total path length of the ion along the direction of incidence. Fig. 3.5 shows a three-dimensional representation of ion penetration into the target material. The ion penetrates the target at point $(0, 0, 0)$ at an angle α to the normal. It comes to rest at a point (x_s, y_s, z_s) . The range is labeled R and the projected range R_p . In the case of Fig 3.5, the direction of the incident ions is not normal to the surface and hence we can also define the depth of penetration, x_s , which is the perpendicular distance from the point where the ion came to rest to the surface.

The mean projected range is the most probable location for an ion to come to rest:

$$R_p = \sum_i x_i / N \quad (3.10)$$

where x_i is the projected range of the i^{th} ion, N is the total number of implanted ions. R_p is also referred to as the first moment of the ion distribution. The second momentum of the ion distribution, i.e. the average fluctuation or straggling is calculated by;

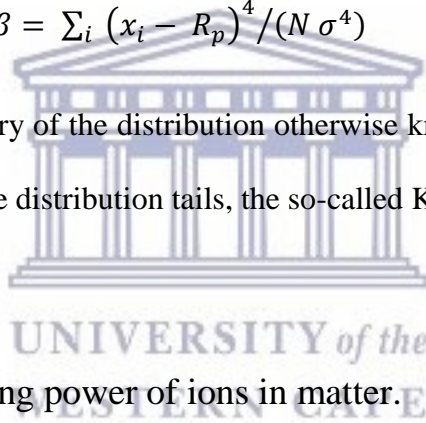
$$\sigma = \left[\frac{\sum_i (x_i - R_p)^2}{N} \right]^{\frac{1}{2}} \quad (3.11)$$

The third and fourth moment of the ion distribution are calculated as follows:

$$\gamma = \sum_i (x_i - R_p)^3 / (N \sigma^3) \quad (3.12)$$

$$\beta = \sum_i (x_i - R_p)^4 / (N \sigma^4) \quad (3.13)$$

Eq. 3.12 indicates the symmetry of the distribution otherwise known as the skewness and eq. 3.13 translates the extent of the distribution tails, the so-called Kurtosis.



3.3.5 Simulation of stopping power of ions in matter.

Prior to implantation, it is important that a simulation of ions distribution be done in order to test the feasibility of the experiment and predict the expected results. A calculation of implantation distributions is based on the Monte Carlo calculations [3.11]. This method makes use of the ion stopping process. A transport calculation has been developed by Zeigler and Biersack [3.12] in the PRAL (Projected Range Algorithm) code, which is part of SRIM (stopping range of ions in matter) [3.9]. In this approach, the paths of the ions in the target are followed. Atom recoils and sputtering are taken into account as well, providing an evaluation

of the implantation damage. The main advantage in SRIM is that implantation can be simulated for a wide range of targets, including composite materials and layered structures.

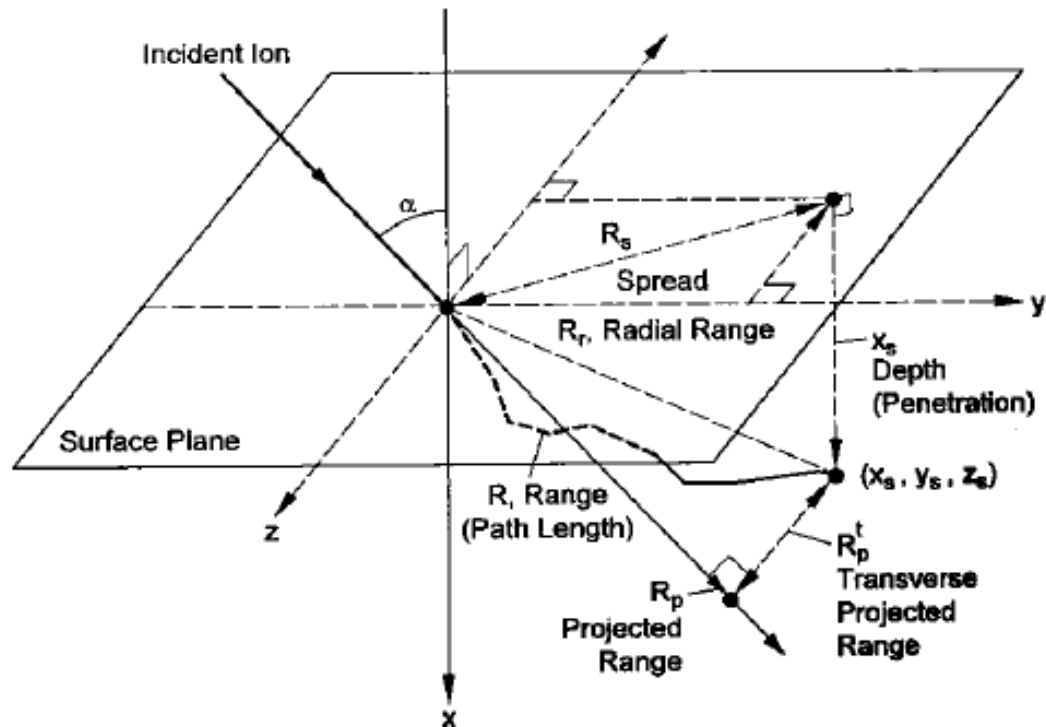


Figure 3.5: A schematic drawing for the depiction of depth, projected range and path length of an incident ion [3.12].

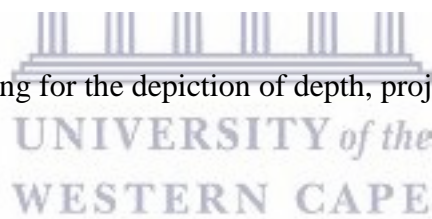


Fig. 3.6 – 3.7, as well as table 3.8, show the expected outcomes for a simulation we have run using a thin film of SiC on Si substrate. Fig. 3.6 shows 1200 ion paths from Monte Carlo calculation for 110 keV Ag atoms in SiC layered on Si substrate, and the ion recoils generated by nuclear collisions. As can be seen, the ion paths are irregular due to the random nature of nuclear scattering. Fig. 3.7 shows computer-simulated ion implantation distribution profile for Ag ions implanted at an energy of 110 keV in SiC film on Si. Table 3.1 shows the ion energy, electronic and nuclear stopping power, the projected range, and the longitudinal and lateral straggling obtained from SRIM simulation software.

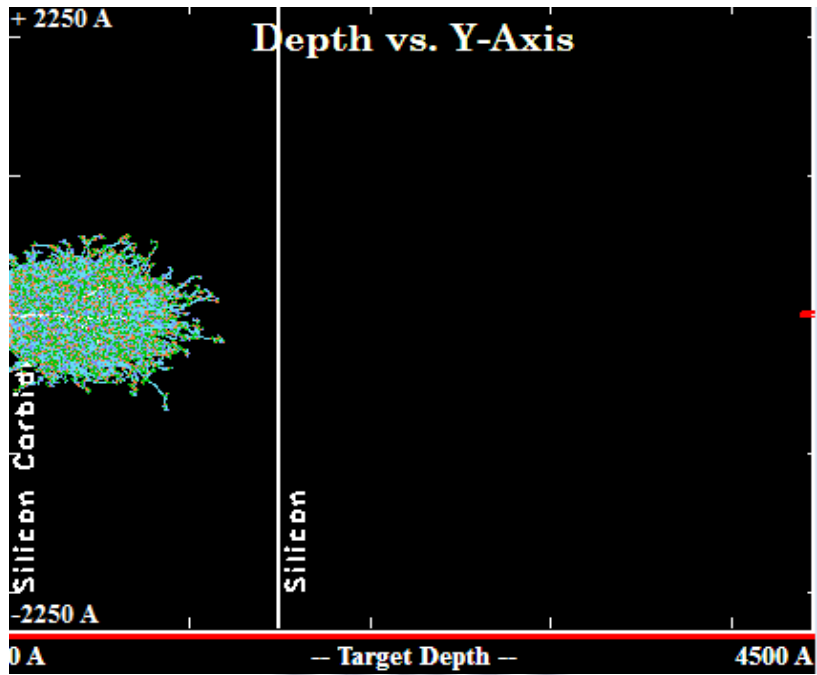


Figure 3.6: The paths of 1200 Ag ions with an energy of 110 keV implanted in SiC layered on top of a Si substrate.

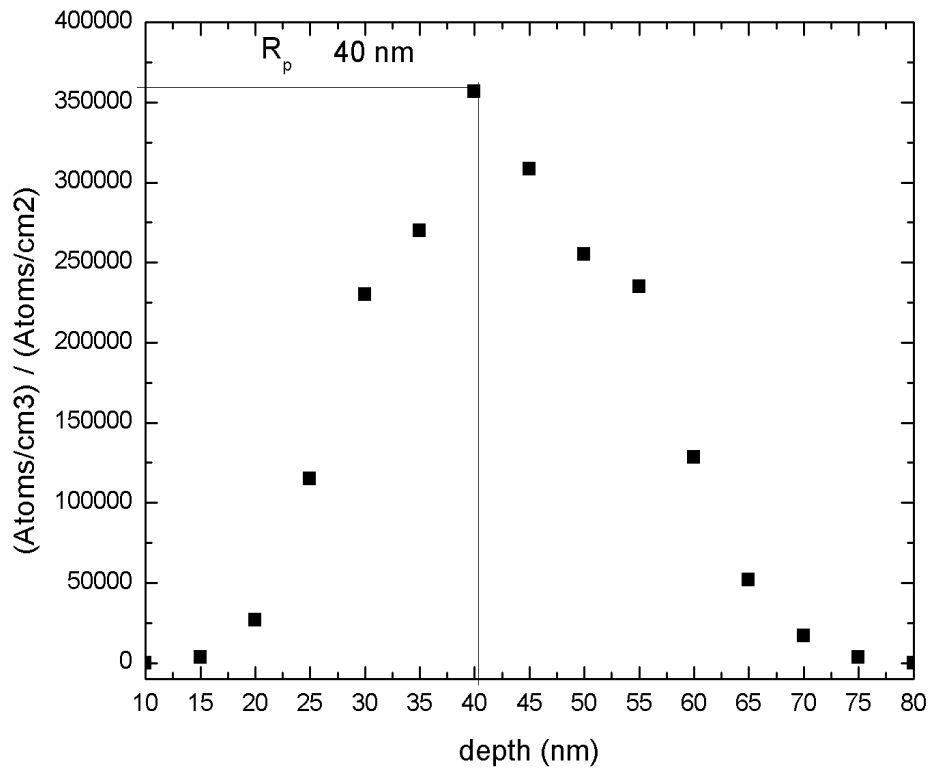
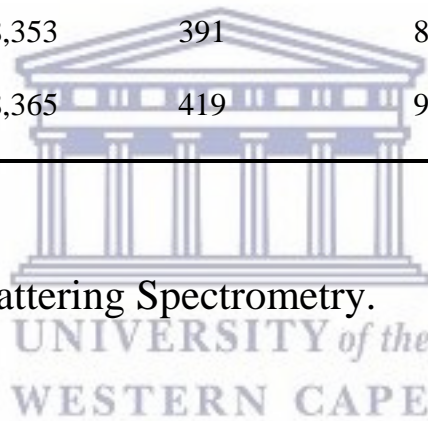


Figure 3.7: Computer-simulated ion implantation distribution profile for Ag ions implanted at an energy of 110 keV in SiC film on Si.

Table 3.1: SRIM output text file for analytically derived stopping power, projected range and stragglings of Ag ions in implanted in SiC.

Ion energy (keV)	dE/dx Elec.	dE/dx Nuclear	Projected Range (Å)	Longitudinal Stragging (Å)	Lateral Stragging (Å)
90	1,61	8,29	335	78	64
100	1,67	8,33	363	84	69
110	1,78	8,353	391	89	73
120	1,859	8,365	419	95	78

3.4 Rutherford Backscattering Spectrometry.



Rutherford Backscattering Spectrometry (RBS) is the widely used ion-scattering method that makes use of high energy He or H ions in a vacuum, for determination of elemental composition and thickness of the probed layers [3.13 – 3.15]. It is also effective in studying reaction kinetics in samples. The ion, on its way in the sample, loses energy in a continuous manner through a series of electronic and nuclear scattering events [3.13 – 3.15]. Typically, an ion undergoes a billiard ball-like collision with the nucleus of an atom in the sample material and it is backscattered with a discrete, large energy loss, whose magnitude is largely dependent on the momentum transfer by the target atom. While most of the energy of the backscattered ion is due to energy transfer process between the beam of ions and atoms of the target, the

spectrum is affected also by a small energy continuum resulting from losses along the depth travelled [3.13 – 3.15].

3.4.1 Basics on Rutherford backscattering spectrometry.

RBS was pioneered by Lord Ernest Rutherford who supervised a series of experiments carried out by Hans Geiger and Ernest Marsden while studying the scattering of alpha particles through metal foils [3.13, - 3.15]. Rutherford was the first person to present the concept of atoms having a positively charged nucleus in 1911 [3.14]. RBS involves elastic scattering of the incident ion, usually ^4He , with the target atom. The angles of the backscattering projectiles are typically 150° - 170° .

RBS is a fast [3.13 – 3.14], non-destructive [3.13 – 3.14], technique and has a good depth resolution, high sensitivity for heavier elements, [3.14] and high precision [3.14]. The drawbacks of RBS is the low sensitivity for light elements [3.13], which often requires the combination of other nuclear-based methods such as nuclear reaction analysis (NRA) or elastic recoil detection analysis (ERDA) [3.14], poor mass resolution for heavy elements and an inability to provide chemical information.

Ion beam techniques are among the most important analytical methods for material characterization, especially thin film characterization [3.13]. RBS is the most conventional ion scattering technique used for near surface layer analysis of materials [3.13 - 3.15]. Energetic ions of the order of MeV penetrate a sample and are elastically backscattered, though a Coulomb interaction with target nuclei. The energy of the backscattered projectiles is measured with an energy sensitive detector, yielding mass and depth profile information on the target atoms.

The elemental identification is obtained from the mass-energy transfer dependence upon collision [3.13] and the multi-element depth profiling is based on the stopping power through inelastic energy loss during ion-solid interactions [3.16].

In modern conventional RBS analysis, a collimated energetic ion beam, generated by an accelerator, is incident on a target material. Fig. 3.8 shows successive steps during a conventional RBS experiment. The backscattered ions are registered by a solid-state detector, the electric pulses generated are amplified and sorted by a multichannel analyser (MCA) [3.13].

The initial series of measurement were done at Tandem Accelerator Mass Spectrometry (TAMS) department at iThemba LABS using 2 MeV high energy $^4\text{He}^+$ alpha particles. A μRBS – ORTEC 456 with HV power supply (bias voltage +40 V) was used and a charge and current of 500 nC and 500 pA, respectively. For energy calibration, AuNiAlO/C standard was used. The incident beam angle was set normal to the sample surface, with the exit angle as 30° and the scattering angle 150° and a tilt angle of 5° . The measured spectrum was collected with OMDAQ software.

Subsequent RBS experiments were done using 2 MeV He^{++} ions provided by the Tandetron accelerator based at iThemba LABS, Cape Town. For energy calibration, AuCo/SiO₂/Si standard was used. The collected charge of 20 μC was maintained in all the samples with an average current of 60 nA. The energy of the recorded backscattered He^{++} was recorded by a Si surface barrier detector with an energy resolution of ~ 23 keV positioned at a scattering angle of 150° .

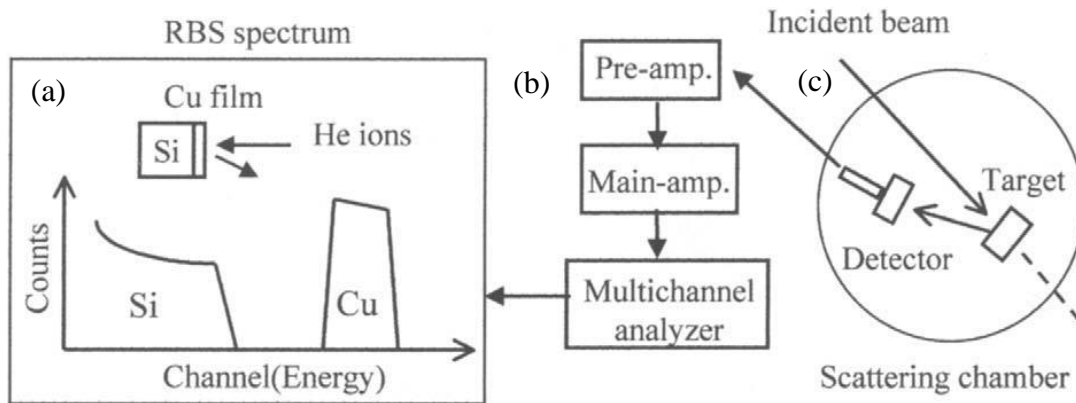


Figure 3.8: Main steps in an RBS experiment (a) example of an RBS spectrum (b) data collection and (c) scattering events

Fig. 3.9 shows a representation of IBM geometry as used in this thesis whereby alpha is the incident angle, beta is the exit angle and theta is the backscattering angle.

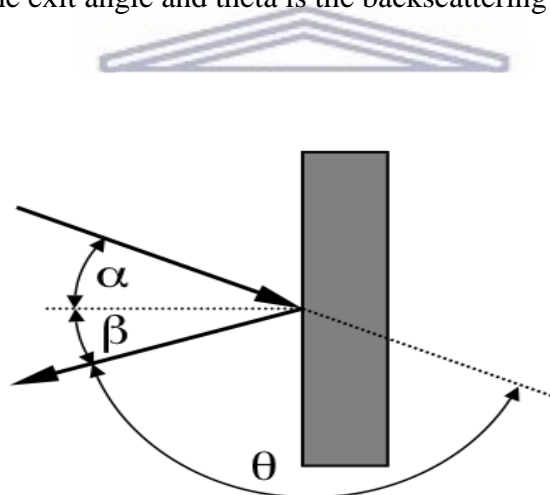


Figure 3.9: A schematic of IBM geometry in RBS as used in our experiment.

In IBM geometry, the incident beam, exit beam and surface normal of the sample are all in the same plane, with

$$\alpha + \beta + \theta = 180^\circ \quad (3.14)$$

3.4.1.1 Realtime studies on Ag implanted in silicon carbide Rutherford backscattering spectrometry.

Real-time RBS was done on one of the as-deposited samples. This was done to evaluate the evolution of Ag in SiC films. The experiment was conducted at iThemba LABS, Cape Town. The real-time RBS, shown in Fig. 3.10 could only go up to a temperature of 600 °C. 2 MeV 4He^{++} alpha particles were used as in the normal RBS. The experiment was as follows: a quick ramp from room-temperature (RT) up to 300 °C at 20 °C/min, followed by a slow ramp from 300 °C to 600 °C at about 3 °C/min for 2 hours and 30 minutes was done. The temperature was then kept constant at 600 °C for 10 minutes followed by sample cooling.

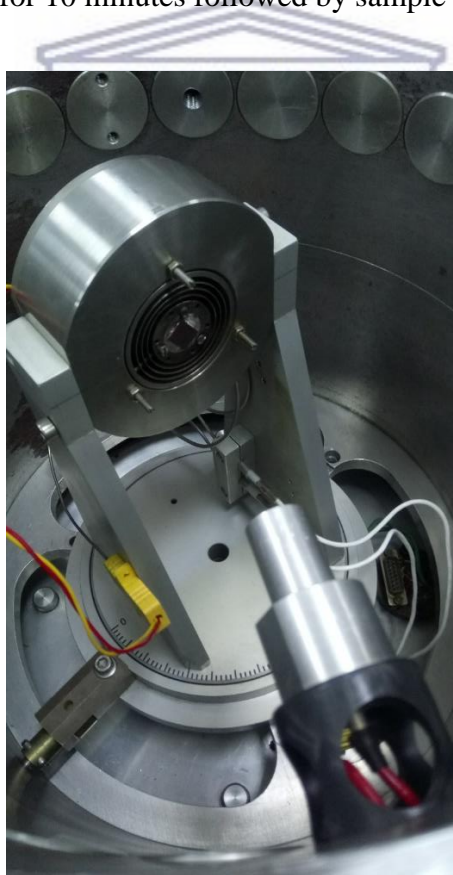


Figure 3.10: Realtime RBS experimental setup as used.

3.4.1.2 Basic Concepts and Analysis.

Fig. 3.11 illustrate four important observables when analyzing an RBS spectrum: E_s represents the energy of the projectile scattered from the surface of the sample as calculated from the kinematic factor and E_t represents the energy of the projectile from the interface; ΔE is the energy width yes at full width half maximum; H_s the height of the yield as probed from the surface of the sample and A the integrated area from the spectrum. In the case of fig. 3.11, the chemical elements that the probed film is made of are heavier than that of the substrate. Thus the energy of the ions scattered from the film is higher than that of those scattered from the substrate. There are three basic parameters that are essential to the processing of an RBS spectrum of a thin film. Those are (a) the kinematic factor, K (b) scattering cross-section $\sigma(\theta, E)$, (c) stopping cross-section $\varepsilon(E)$ all of which are explained in detail below.

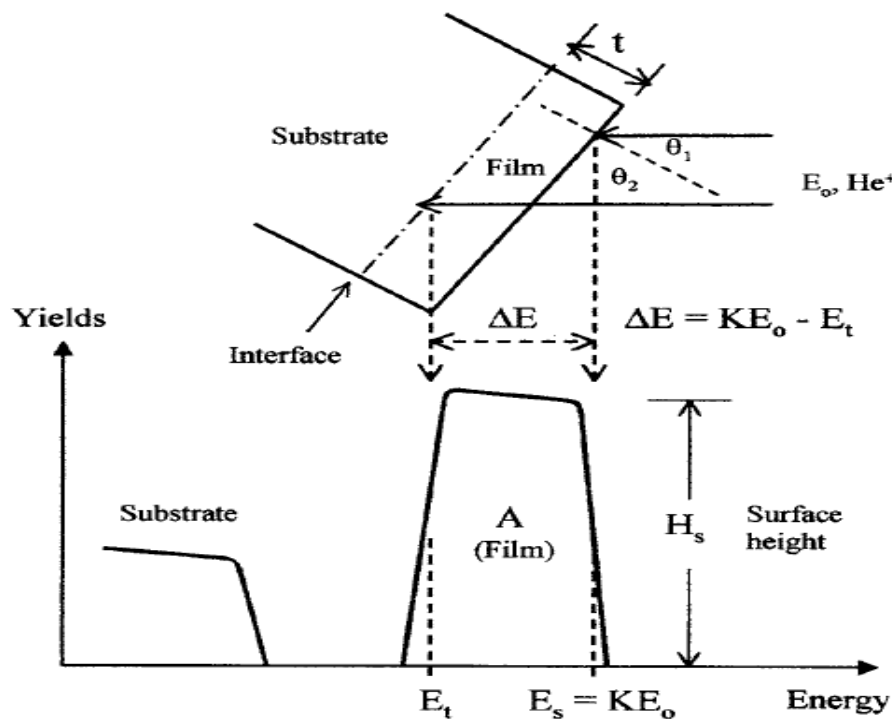


Figure 3.11: Schematic of a typical RBS spectrum on a thin film deposited on a lighter substrate [3.13].

3.4.1.3 Kinematic factor and mass resolution.

The energy E_1 of a backscattered projectile with incident energy E_0 and mass M_1 after scattering and has not suffered losses is given in the laboratory system by

$$E_1 = KE_0 \quad (3.15)$$

where K is the kinematic factor given by

$$K = \frac{M_1^2}{(M_2 + M_1)^2} \left\{ \cos \theta \pm \left[\left(\frac{M_2}{M_1} \right)^2 - \sin^2 \theta \right]^{\frac{1}{2}} \right\}^2 \quad (3.16)$$

θ is the scattering angle and M_2 is the mass of the target nucleus initially at rest. For $M_1 < M_2$ only the + sign in eq. 3.16 applies. If $M_1 > M_2$ then eq. 3.16 has two solutions and the maximum possible scattering angle θ_{max} is given by;

$$\theta_{max} = \arcsin \left(\frac{M_2}{M_1} \right) \quad (3.17)$$

The kinematic factor K , as a function of mass M_2 , is shown in Fig. 3.12 for incident protons, ^4He , and ^7Li at a scattering angle of 165° .

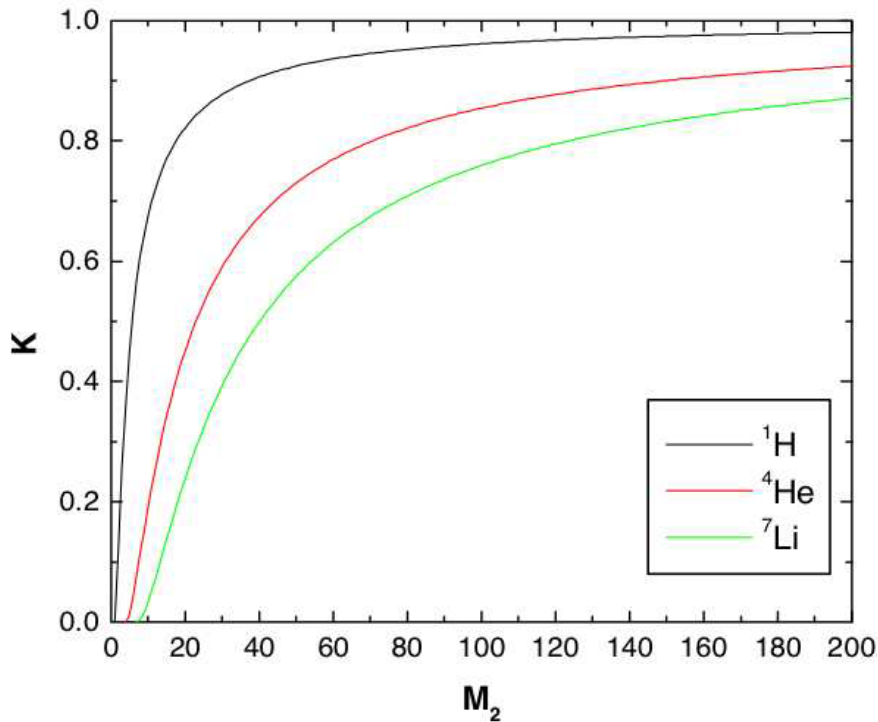


Figure 3.12 Kinematic factor, K , at a scattering angle $\theta = 165^\circ$ as a function of target mass M_2 for three incident ions ${}^1\text{H}^+$, ${}^4\text{He}^+$, and ${}^7\text{Li}^+$ [3.17].

The K factor is significant because it provides a tool to identify unknown elements in the spectrum. The accuracy of the K factor to identify unknown elements is dependent on the mass resolution of the RBS analysis system. If two different target elements with a mass difference ΔM_2 are present, then the energy separation ΔE_1 of particles backscattered from the two masses is given by;

$$\Delta E_1 = E_0 \frac{dK}{dM_2} \Delta M_2 \quad . \quad (3.18)$$

The maximum energy that can be resolved is limited by the resolution of the RBS system. Fig. 3.12 shows that the best energy separation and mass resolutions are obtained for light target elements where the derivative dK/dM_2 is steep, while for heavy elements the mass resolution gets smaller.

3.4.1.4 The relation between energy loss and thin film thickness.

Fig. 3.11 shows that the bulk of the probed film is confined between the film surface and its interface with the substrate. The energy of the ion scattered from the surface is given by E_s and those scattered from the interface, E_t . The difference between these two energies is termed the energy width of the thin film given by;

$$\Delta E = E_s - E_t = E_s K - E_t . \quad (3.19)$$

The relation between thickness, t , and energy width can be worked out from eq. 3.19, which is given by;

$$\Delta E = [S]t \quad (3.20)$$

$$\Delta E = \left[\frac{K}{\cos\theta_1} \left(\frac{dE}{dx} \right)_{in,av} + \frac{1}{\cos\theta_2} \left(\frac{dE}{dx} \right)_{out,av} \right] t \quad (3.21)$$

where K is the kinematic factor, $(dE/dx)_{in,av}$ is the average value of the stopping power along the inward path of the incident ion, $(dE/dx)_{out,av}$ is the average value of the stopping power along the outward path of the scattered ion, and t is the thickness of the film. The parameter $[S]$ is usually called the energy loss factor or the S factor.

3.4.1.5 Stopping power and energy loss.

Eq. 3.21 shows that the capability of the RBS technique to measure the thickness of the film comes from the energy loss of the impinging ions in the sample. We can thus define the stopping power that is the energy loss ΔE per unit distance Δx travelled by the incident ions.

Δx measured in $\frac{10^{15} \text{ atoms}}{\text{cm}^2}$. Higher accuracy in the stopping power results in a better determination of the thickness and better depth profiling [3.14].

The stopping power of any ion in any target element can be calculated using the SRIM [3.11] package. Generally, the accuracy of calculated stopping powers for incident protons and ^4He ions is about 5% and about 10% for heavier ions. In compounds, the stopping power is usually governed by Bragg's rule as eq. 3.7 indicates.

3.4.1.6 Evaluation of energy loss.

The energy of a particle in the depth x is given by the difference between the energy of the incident ion E_0 and the integrated energy loss over the distance travelled in the sample [3.17].

$$E(x) = E_0 - \int_0^x \frac{dE}{dx}(E(x'), x') dx' \quad (3.22)$$

Here we assume that the particle starts with an initial energy E_0 at the surface of ($x = 0$), and $\frac{dE}{dx}(E(x'), x')$ is the energy and depth dependent stopping power. x is the path length into the material in areal density ($10^{15} \frac{\text{atoms}}{\text{cm}^2}$). By differentiating eq. 3.22, a differential equation is obtained:

$$\frac{dE}{dx} = -\epsilon(E) \quad (3.23)$$

where $\epsilon(E)$ is the energy dependant stopping cross-section. Doolittle [3.18] developed an algorithm for the evaluation of energy loss for RUMP [3.19] program, which was also used in earlier versions of SIMNRA [3.20]. He expands the particle energy into Taylor series and the energy E_1 after a layer of material with thickness, Δx is given by;

$$E_1 = E_0 + \Delta x \frac{dE}{dx} (E_0) + \frac{1}{2} \Delta x^2 \frac{d^2E}{dx^2} (E_0) + \frac{1}{6} \Delta x^3 \frac{d^3E}{dx^3} (E_0) \quad (3.24)$$

Noting that:

$$\frac{dE}{dx} = -\epsilon \quad (3.25)$$

$$\frac{d^2E}{dx^2} = \frac{d}{dx} (-\epsilon) = -\frac{d\epsilon}{dE} \frac{dE}{dx} = \epsilon' \epsilon \quad (3.26)$$

$$\frac{d^3E}{dx^3} = \frac{d}{dx} (\epsilon' \epsilon) = \frac{d\epsilon'}{dE} \epsilon + \epsilon' \frac{d\epsilon}{dE} = -\epsilon'' \epsilon^2 - \epsilon'^2 \epsilon \quad (3.27)$$

$\epsilon' = d\epsilon/dE$ is the first and $\epsilon'' = d^2\epsilon/dE^2$ the second derivative of the cross-section ϵ .

This gives the final result:

$$E_1 = E_0 - \Delta x \epsilon + \frac{1}{2} \Delta x^2 \epsilon \epsilon' - \frac{1}{6} \Delta x^3 (\epsilon'' \epsilon^2 + \epsilon'^2 \epsilon) \quad (3.28)$$

The drawback with eq. 3.28 is the requirement for the first and second order derivative of the stopping power. Stopping powers supplied by the SRIM program do not have smooth derivatives and thus use of eq. 3.28 can result in large errors. Moreover, eq. 3.28 does not provide a criterion on how to select the step width Δx in order to obtain the desired accuracy and does not provide an error estimate.

3.4.1.7 Energy loss due to straggling in compounds.

The physics of inelastic and elastic collisions during ion implantation and ion scattering in the case of RBS experiment are similar. When a beam of charged particles penetrates matter, the slowing down is accompanied by a spread in the beam energy and this effect is referred to as straggling. It is a result of statistical fluctuations of the energy transfer during collisions. For compounds like SiC in our case, a simple summation rule for energy loss straggling has been

proposed [3.18]. The straggling in a compound consisting of elements i with atomic concentration c_i ($\sum_i c_i = 1$) is calculated with

$$\sigma^2 = \sum_i c_i \sigma_i^2 \quad (3.29)$$

with σ_i^2 being energy straggling in each element. Energy loss straggling has different contributions [3.14, 3.16]:

1. Nuclear energy loss straggling due to statistical fluctuations in nuclear energy loss. Nuclear energy loss straggling is only important for heavy ions.
2. Geometrical straggling due to finite detector solid angle and finite beam spot size, resulting in a distribution of scattering angles and different path lengths for outgoing particles. Geometrical straggling is important for grazing incident or exit angles and large solid angle detectors.
3. Straggling due to multiple small angle scattering, resulting in angular and energy spread on the ingoing and outgoing paths.
4. Straggling due to surface and interlayer roughness and thickness inhomogeneity of absorber foils.

3.4.1.8 Scattering Cross Section.

a) Rutherford cross section.

The Rutherford cross section for backscattering is given in the laboratory system by

$$\sigma_R \left[\frac{mb}{sr} \right] = 5.1837463 \times 10^6 \left(\frac{Z_1 Z_2}{E[keV]} \right)^2 \frac{\left\{ (M_2^2 - M_1^2 \sin^2 \theta) + M_2 \cos^2 \theta \right\}^2}{M_2 \sin^4 \theta (M_2^2 - M_1^2 \sin^2 \theta)^{1/2}} \quad (3.30)$$

θ is the scattering angle, Z_1 and M_1 is the atomic number and the mass of the projectile, respectively, and Z_2 and M_2 are the nuclear charge and the mass of the target atom, respectively.

It has been shown actual cross-sections deviate from Rutherford at both high and low energies for all projectile-target pairs [3.14]. The low-energy departures are caused by a partial screening of the nuclear charges by the electron shells surrounding both nuclei [3.14, 3.16].

The screening is accounted for with a screening factor, F :

$$\sigma = F\sigma_R \quad (3.31)$$

For $\theta > 90^\circ$ the correction factor by L'Ecuyer *et al.* [3.21] is widely used:

$$F_{L'Ecuyer} = 1 - \frac{0.049Z_1Z_2^{4/3}}{E_{CM}} \quad (3.32)$$

E_{CM} is the energy in the center of the mass system (in keV). Tabulated values of $F_{L'Ecuyer}$ can be found in [3.21]. The correction for backscattering angles $\theta > 90^\circ$ at typical energies used in ion beam analysis usually is small. For 1 MeV ^4He ions backscattered from Au the correction is only about 3.5%. The correction factor by L'Ecuyer (eq. 3.32) is a first order correction and does not take into account the influence of the scattering angle θ . For $\theta < 90^\circ$ eq. 3.32 will underestimate the necessary correction to the Rutherford cross section. At small scattering angles the angular- and energy dependent correction factor by -Andersen *et al.* [3.22] should be used:

$$F_{Andersen} = \frac{\left(1 + \frac{1}{2} \frac{V_1}{E_{CM}}\right)^2}{\left\{1 + \frac{V_1}{E_{CM}} + \left[\frac{V_1}{2E_{CM}\sin\theta_{CM/2}}\right]^2\right\}^2} \quad (3.33)$$

θ_{CM} is the scattering angle in the center of the mass system. The increase in the kinetic energy

V_1 is given by

$$V_1[\text{keV}] = 0.04873Z_1Z_2 \left(Z_1^{2/3} + Z_2^{2/3}\right)^{1/2} \quad (3.34)$$

3.4.2 Instrumentation in relation to conventional Rutherford backscattering spectroscopy.

To carry out a conventional RBS measurement, three basic equipment are required: (a) An ion accelerator, (b) a scattering chamber, and (c) a particle detection system coupled with a multi-channel analyser (MCA) [3.13]. The accelerator produces well-collimated monoenergetic ion-beams. 2 MeV $^4\text{He}^+$ ions were used in this thesis because in this energy range the scatterings are purely Coulomb and the stopping power data are well known. Moreover, $^4\text{He}^+$ ions are preferred to Li, B, or C ions because they generate less radiation damage on the Si detector, which is the most widely used for modern RBS [3.13].

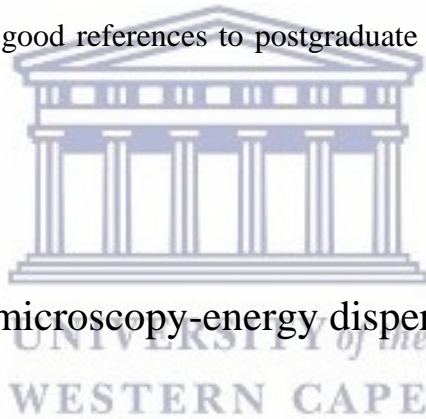
The ion beam generated by the accelerator is then introduced into the scattering chamber and penetrates the sample. The sample is usually mounted on a goniometer, which is a mechanical device that can tilt, rotate, and translate the sample [3.13]. In the scattering chamber, a particle detector is set at a scattering angle usually between 150° to 170° from the direction of the incident beam. The Si detector is preferred to other types of detectors because of certain attributes such as low cost, easy operation, its compactness, prolonged lifetime and good resolutions in the range between 13 to 15 keV [3.13].

The backscattered ions that strike the Si detector lead to the creation of electron-hole pairs. These electron-hole pairs are then collected by the electrode to form electric pulses. One ion creates one electrical pulse in the detector. The amplitude of the pulse is proportional to the energy of the ion. The pulses from the detector are further amplified and shaped by an amplifier. Then they are sent to the MCA. The MCA is an electronic system that converts the pulses to digital signals, sorts, and displays the signals on the screen in the form of counts vs. channel, which is called an RBS spectrum [3.13]. The energy of the scattered ions is proportional to the

channel number, assuming the linearity of the detector and thus the channel number scale can be converted to an energy scale or depth scale.

3.4.3 Computer simulation and fitting programs for analysis of RBS spectra.

SIMNRA [3.20] was used to convert the channel numbers to energy of the backscattered He⁺⁺ and to simulate the experimental data into elemental depth concentrations; while DataFurnace [3.23] computer package was used to convert the RBS spectra into elemental depth profile spectra. Two appendixes are attached at the end of the thesis manuscript explaining the detailed steps we followed. These are good references to postgraduate students working with RBS / ERD data.



3.5 Scanning electron microscopy-energy dispersive spectroscopy.

3.5.1 Introduction.

Microscopy techniques provide a way to study the surface morphology, elemental composition and microstructural details of the sample. The first electron microscopy (EM), a transmission electron microscope (TEM), was invented by Ruska and Knoll in 1931 [3.24 - 3.26]. Knoll was to pioneer a precursor of the modern scanning electron microscopy (SEM), in which it was possible to move the sample rather than the electron probe. SEM/EDX are primarily used for imaging, elemental analysis of the sample; they have both good spatial resolution and sensitivity.

3.5.2 Basic principles of scanning electron microscopy.

3.5.2.1 Basic principle.

Fig. 3.13 (a) shows that an electron source generates a beam of electrons that is focused into a probe, and then scanned across the surface of a sample in a raster fashion [3.24, 3.27 - 3.28]. When the electron probe interacts with the surface of the sample, various kinds of emissions occur; when these are imaged by the respective detectors, they offer complementary information about the specimen to the user [3.27].

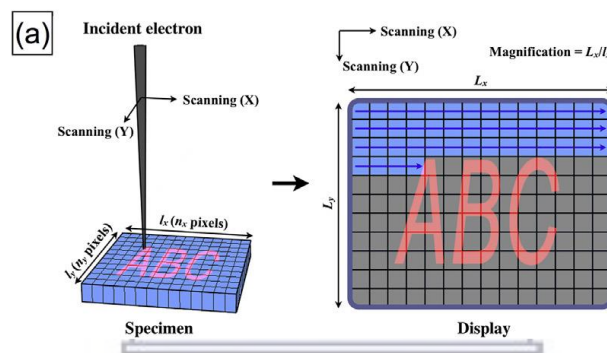


Figure 3.13: A schematic illustration of (a) electron beam rastering across a sample and the emitted signal is transferred as a function of position on a pixelated image/monitor and (b) the emitted energy spectrum from secondary electrons (SEs) to elastically reflected electrons.

Fig. 3.14 shows some of the signals emitted from the interaction volume of the electron beam below the surface. Secondary electrons (SEs) are emitted during the inelastic scattering of the electron beam with the sample whereby part of the incident beam energy is transferred to the specimen atoms. Backscattering electrons (BSEs) are emitted during elastic scattering when the incident beam electrons collide with the nucleus of the specimen atoms resulting in a change in direction, without any energy transfer. SEs and BSEs have different maximum escape

depths given their respective energy differences and are captured to obtain morphological/topological and compositional information, respectively [3.24]. Using an X-ray detector, chemical information about the sample is obtained. Energy dispersive spectroscopy (EDX) is thus used in the SEM for elemental analyses.

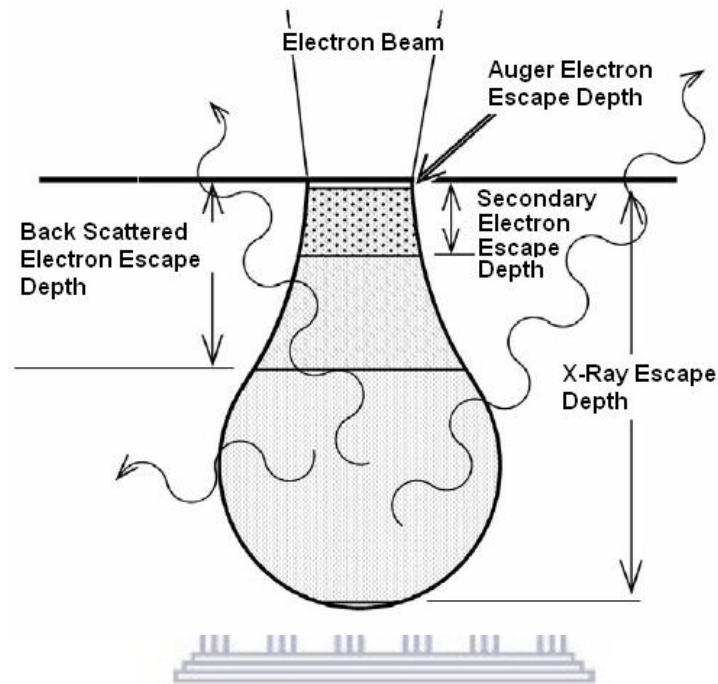


Figure 3.14: Schematic of some of the signals from the interaction volume in SEM [3.27]

Elastic scattering in the sample causes the direction of IE electrons to vary. The screened Rutherford model is used to describe the cross-section of elastic scattering and is given as follows:

$$\frac{d\sigma_{el}}{d\Omega} = [f(\theta)]^2 = \frac{e^4 Z^2}{4(4\pi\epsilon_0)^2 m^2 v^4} \times \frac{1}{\left[\sin^2\left(\frac{\theta}{2}\right) + \sin^2\left(\frac{\theta_0}{2}\right)\right]^2} \quad (3.35)$$

with $\sin\left(\frac{\theta_0}{2}\right) \cong \frac{\theta_0}{2} = \frac{\lambda}{4\pi R}$, $R = a_H Z^{-1/3}$, and $a_H = \frac{h^2 \epsilon_0}{\pi m_0 e^2}$. σ is the total cross section, e is the charge of an electron, Z is the atomic number, ϵ is the dielectric constant, m is the mass of the electron, v is the velocity of the electron $a_H = 0.0569 \text{ nm}$ is the Bohr radius, λ is the wavelength of the electron. The number of BSEs is strongly tied to the cross section given in

eq. 3.35, and ultimately to Z^2 . Such that, areas of the specimen composed of higher atomic number elements will emit more backscatter signal and thus appear brighter in the image.

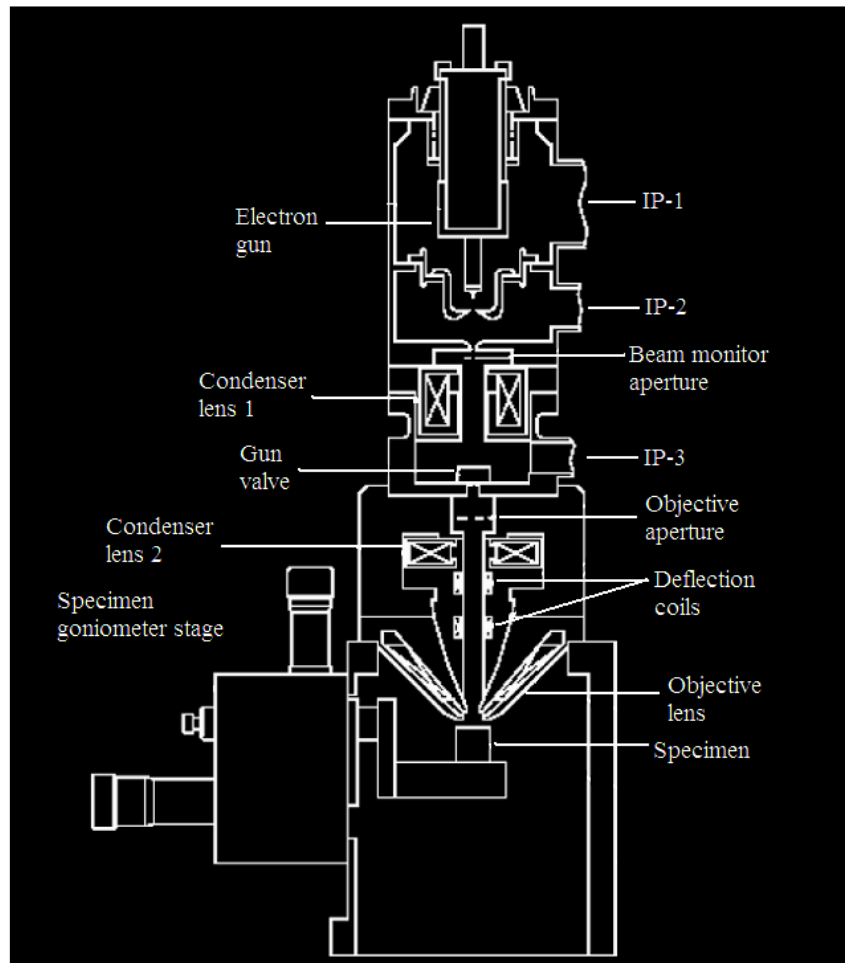
The topography is dependent on the number of SEs and BSEs being emitted from various areas of the sample as well as the directions they take in relation to the position of the detector [3.27]. Moreover, SEs have a much shorter escape depth than BSEs, this combined with the fact that SEs emission is proportional to $\sec[\theta]$, where θ is the surface tilt, causes the image contrast of the SEs to be highly topographic [3.24].

3.5.2.2 Instrumentation related to scanning electron microscopy.

SEM carries the advantages that it requires minimal sample preparation, a much larger depth of field is retained, samples in solid or liquid form can be observed, and does not require any mechanical crushing of the sample, which leads to the destruction of a sample [3.24]. SEM primarily consist of an electron source/gun, a series of lenses and apertures, controls for specimen position, an area of beam/specimen interaction, all of these are kept at high vacuum levels [3.27].

An electron beam is generated by the electron gun/source and accelerated down the column, followed by a reduction and focusing of the beam by the lenses on the sample surface. The signal that is generated from the sample is acquired by the detector and processed to produce an image on the screen [3.27]. There is a one-to-one correspondence between the rastering pattern on the specimen and the rastering pattern used to produce the image on the screen. The image displayed on the screen is a two-dimensional raster pattern of grayscale values. The size of the screen's raster pattern is a constant, i.e. magnification will only increase if we reduce the size of the area scanned on the specimen [3.27].

$$\text{magnification} = \frac{\text{area scanned on monitor}}{\text{area on scanned on specimen}} \quad (3.36)$$



WESTERN CAPE

Figure 3.15: A schematic depiction of a modern conventional SEM [3.27].

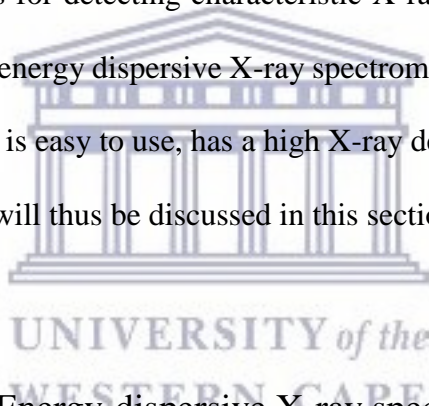
Electromagnetic lenses used in SEM have defects, the most prevalent are spherical and chromatic aberration. Both spherical and chromatic aberration directly influence the diameter, d , of the electron beam on the sample. Spherical aberration, d_s , is caused by the spatial non-uniformity of the electric field produced by lenses whereby some electrons are strongly bent than others resulting in multiple focal points. To circumvent this phenomenon an aperture must be used but if the aperture is too small it may results in diffraction, d_d . Similarly, the energy spread of the beam electrons also lead to a series of focal points and this is called chromatic aberration, d_c . Thus, instead of a clear focal point, a “disc of minimum confusion” is obtained:

$$d = \sqrt{d_0^2 + d_d^2 + d_s^2 + d_c^2} \quad (3.37)$$

d_o is the contribution to the disc from the source size.

3.5.3 Energy dispersive spectroscopy.

The electron beam, as shown on the schematic in fig.3.15, also generates characteristic X-rays from the interaction volume. These X-rays are emitted via electron transition from an occupied level to a lower level where a hole is produced by irradiation of the incident electron beam [3.24]. There are two methods for detecting characteristic X-rays; wavelength dispersive X-rays spectrometry (WDS) and energy dispersive X-ray spectrometry (EDX). EDX is a popular attachment to SEM, because it is easy to use, has a high X-ray detection efficiency and a short measurement time [3.27] and will thus be discussed in this section.



3.5.3.1 Basic principle of Energy-dispersive X-ray spectroscopy.

As discussed, BSEs are responsible for the observed compositional contrast in SEM images as a result of the different atomic elements and their distribution in samples [3.28]. EDX allows for the identification of those particular elements and their relative proportions. EDX is a powerful form of elemental analysis but it has drawbacks such as the low detection limit of 1000 – 3000 ppm > 10 % wt% and the fact that it can only detect elements heavier than Beryllium [3.18].

Two kinds of X-rays are generated during the inelastic collision of the electron beam with the sample, namely the characteristic X-ray and continuum (Bremsstrahlung) X-rays [3.27]. Characteristic X-rays are generated when a vacancy in the inner shell of the atom is created by an incident high energy electron (E_o). The vacancy is subsequently filled by an electron from higher energy (outer) shell. During this transition, energy is emitted in the form of an X-ray. The energy of the X-ray is characteristic of the specimen atomic number from which it is derived.

The characteristic X-ray lines are named according to the shell in which the initial vacancy occurs and the shell from which the electron drops to fill the vacancy. For instance, if the initial vacancy is created in the K-shell and the electron filling the vacancy is from the adjacent shell (L), a $K\alpha$ X-ray is emitted, see Fig. 3.16.

Continuum X-rays are generated when a beam of electrons interact with the coulomb (electric) field of the nucleus of the specimen atom. During this interaction, the beam energy loses energy that is given off as continuum X-rays. Continuum X-rays represent the background on which the characteristic X-rays peaks are superimposed and they are a nuisance to operators [3.27].

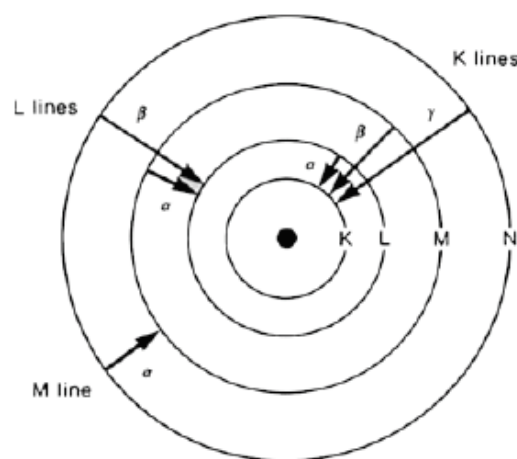


Figure 3.16: A schematic of the electron shell configuration illustrating various transitions.

3.5.3.2 Instrumentation related to energy dispersive X-ray spectroscopy.

The EDX system comprises three basic components namely; the X-ray detector, pulse processor and the multichannel analyser (MCA), Fig 3.17. The absorption of an individual X-ray photon by the detector leads to the ejection of a photoelectron which gives up its energy for the formation of electron-hole pairs. The electron-hole pairs, in turn, swept away by an applied bias to form a charge pulse. The charge pulse is converted to a pulse voltage by a pre-amplifier. The signal is further amplified and “shaped” by a linear amplifier (pulse processor) and then passed on to an MCA where the data is displayed as a histogram of intensity vs voltage. The voltage pulse produced is proportional to the energy of the incoming X-ray photon.

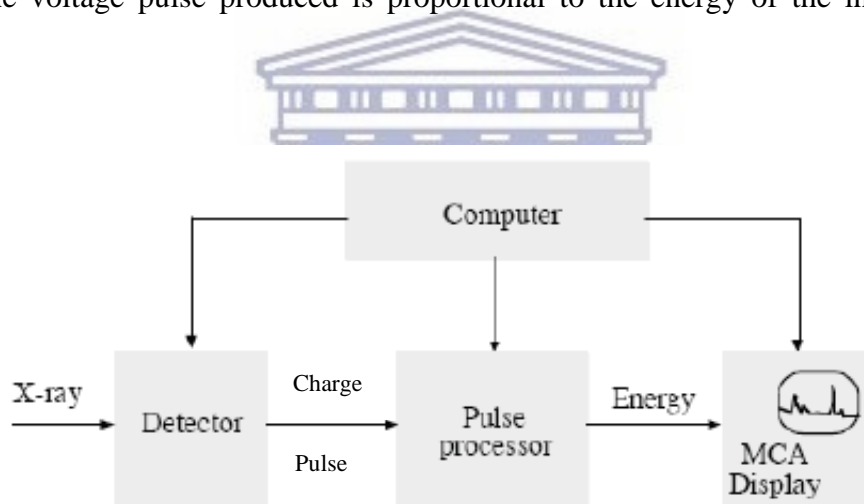


Figure 3.17: A schematic depiction of a typical X-ray detection in EDX.

Top view SEM micrographs were collected from uncoated films by an Everhart-Thornley secondary electron detector using a Zeiss Auriga field-emission gun scanning electron microscopy (FEG-SEM); the accelerating voltage is shown on the appended legend on the images. For EDX, an Oxford Instruments X-Max solid-state silicon drift detector was used to collect the spectra.

3.6 Fourier transform Infrared spectroscopy.

3.6.1 Introduction.

Fourier Transform infrared (FTIR) spectroscopy is a structural characterization and elemental identification technique [3.29]. FTIR measurements are non-destructive, easy to perform, and require minimal sample preparation. In IR spectroscopy, the absorption of infrared light by the sample as a function of frequency is measured. In this technique, the frequencies of mechanical vibrations are used to identify the types of bonds in molecules since different functional groups absorb different characteristic frequencies [3.30-3.33].



3.6.2 Fundamentals on Fourier transform infrared spectroscopy.

Infrared spectroscopy involves the absorption of different infrared frequencies by a sample under illumination by an infrared beam. The change in the transmittance indicates the spectral region where the molecule absorbs the energy from the IR source at each vibrational transition.

Fig. 3.18 shows a Michelson interferometer that FTIR spectroscopy is based on. The Michelson interferometer consists of a beamsplitter, a fixed mirror, and a moving mirror. The beamsplitter takes the incoming infrared beam and splits it into two beams of nearly equal intensity. Half of the infrared beam is transmitted through the beamsplitter and directed onto a fixed mirror. The other half reflects off the beamsplitter and directed onto the moving mirror. The two beams reflect off the two mirrors and recombine at the beamsplitter. Due to the changes in the relative position of the moving mirror to the fixed mirror, an interference pattern is generated. The generated resulting beam passes through the sample where selective absorption takes place and

then continues on to the detector. The detected signal called the interferogram as a function of the moving mirror is fed to a computer. Fourier transformation converts the interferogram to the final infrared spectrum.

The fundamental vibration frequency for diatomic molecules in terms of wavenumber $\bar{\nu}$ is given by,

$$\bar{\nu} = \frac{1}{2\pi c} \sqrt{\frac{k}{\mu}} \quad (3.38)$$

where k is the force constant of the oscillator and μ is the reduced mass of two particles and expressed as;

$$\mu = \frac{m_1 m_2}{m_1 + m_2} \quad (3.39)$$

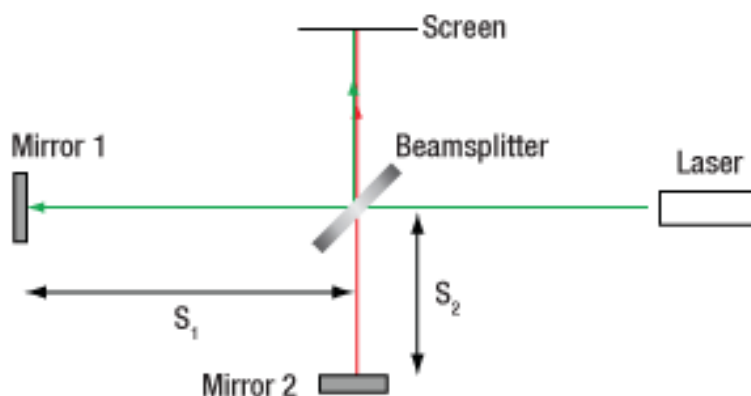


Figure 3.18 Simplified schematic of a typical FTIR spectrometer showing a Michelson interferometer [3.29].

FTIR spectra in this thesis were collected in transmission mode using the Perkin-Elmer Pentagon 1000 FTIR Spectrophotometer in the wavelength range of $400 - 4000 \text{ cm}^{-1}$ with a resolution of 4 cm^{-1} . The thin films were deposited on Si (100) substrates which are partially transparent to infrared light. In order to account for the absorption of the Si (100) substrate, the measured spectra were corrected with a background spectrum of a bare substrate.

The transmittance can be deduced from the Beer-Lambert law as [3.34]:

$$T = \frac{I}{I_0} = e^{-\varepsilon cl} \quad (3.40)$$

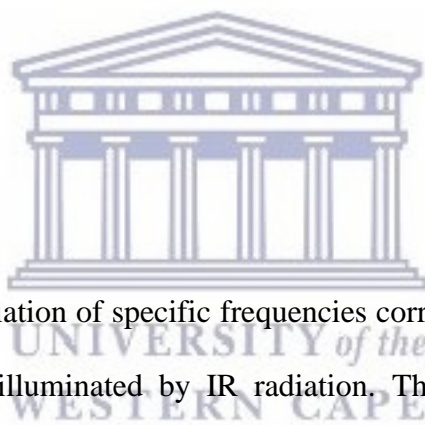
where l is the depth the transmitted beam travels, c is the concentration of the absorbing material, and ε is the molecular absorption coefficient. The optical density or absorbance is defined as [3.35]:

$$A = -\log_{10}\left(\frac{I(l)}{I_0}\right) \quad (3.41)$$

thus

$$A = 0.434\varepsilon cl \quad (3.42)$$

3.6.3 Vibrational modes.



Molecules absorb infrared radiation of specific frequencies corresponding to vibration modes of molecules in the sample illuminated by IR radiation. These molecular vibrations are restricted to certain degrees of freedom. A molecule that is made of N number of atoms has $3N$ degrees of freedom with movement in the three Cartesian plane directions [3.29]. Moreover, the molecule can vibrate in the three dimensions and this applies to rotational motions. For linear molecules, only two degrees can describe rotational motion. The vibration of non-linear and linear molecules result in $3N-6$ and $3N-5$ degrees of freedom, respectively.

The absorption of infrared radiation causes molecules to vibrate in linear motion and rotation motion, absorption bands are observed instead of expected discrete lines, molecular excitations involve many quantized energy levels and thus many transitions [3.29].

3.6.3 Bonding in Silicon carbide films.

Silicon carbide films contain a range of chemical bonds depending on the film composition, the stoichiometry and the microstructure. All these properties are very sensitive to the deposition conditions and post-deposition treatment of the films. Table 3.2 lists the usually prominent infrared absorption bands in non-hydrogenated amorphous and crystalline silicon carbide films.

Table 3.2: Infrared absorption bands in a-SiC and nc-SiC and their assignments.

Bonding	Wavenumber (cm⁻¹)	Assignment
Si-C	800	Stretching
Si-O-Si	1100	Stretching
C=C(sp ²)	1500 -1600	Stretching

UNIVERSITY of the
WESTERN CAPE

References.

- [3.1] V. Linderberg, *Physical vapour deposition*, RIT School of Physics and Astronomy, (2008). Accessed at <https://people.rit.edu/vwlsps/LabTech/Deposition.pdf> on 04/02/2019.
- [3.2] W. Hale, *what is electron beam (e-beam) evaporation*, AJA international Inc. Accessed at <https://ajaint.com/what-is-e-beam-evaporation.html> on 04/02/2019.
- [3.3] D. M. Mattox, *Handbook of physical vapour deposition (PVD) processing*, William Andrew Inc., Society of Vacuum Coaters Albuquerque, New Mexico.
- [3.4] K. J. Pondo, *In-situ realtime Rutherford backscattering spectrometry study of Ni/Ge interaction*, M.Sc. Thesis, Department of Physics, University of Zambia, 2010.
- [3.5] M. Canino, *Phosphorus ion implantation in SiC: Influence of the annealing conditions on dopant activation energies*, Ph.D. Thesis, University Degli Studi di Bologna,
- [3.6] L.A. Giannuzzi, B. I. Prenzler, and B. W. Kempshall, *Introduction to focused ion beams*, Springer Science + Business Media, Inc., 233 Spring Street, New York, NY 10013, USA.
- [3.7] G. Lulli, *Introduction to ion implantation*, CNR Institute for Microelectronics and Microsystems (IMM), Bologna, <http://webarch.bo.imm.cnr.it/lulli/didattica/index.html>
- [3.8] T.T Hlatshwayo, Ph.D. dissertation: *Diffusion of Silver in 6H-SiC*, University of Pretoria, South Africa, July 2010.
- [3.9] W.H. Bragg and R. Kleeman, *On the α particles of radium, and their loss of range in passing through various atoms and molecule*, The London, Edinburg, and Dublin Philosophical Magazine and Journal of Science 10 (1905) 318-340.

- [3.10] J.F. Ziegler and Manoyan, *The stopping of ions in compounds*, Nuclear Instruments and Methods in Physics Research Section B: Beam Interactions with Materials and Atoms, 35 (1988) 215-228.
- [3.11] J.F. Ziegler, SRIM: *The stopping and range of ions in matter*. Accessed at <http://www.srim.org/>.
- [3.12] Eckstein W, Computer simulation of ion-solid interactions, Springer –Verlag Berlin Heidelberg.
- [3.13] H.S. Nalwa, *Handbook of Thin Film Materials*, Academic Press, Elsevier Inc., 2002.
- [3.14] M. Mayer, *Rutherford Backscattering Spectrometry (RBS)*, Max-Planck-Institut für Plasmaphysik, EUROATOM Association, Garching, Germany, 2003. Accessed on http://users.ictp.it/~pub_off/lectures/Ins022/Mayer_1/Mayer_1.pdf.
- [3.15] Y. Zwang, A. Debelle, A. Bouille, P. Kluth, and F. Tuomisto, *Advanced techniques for characterization of ion beam modified materials*, Current Opinion In Solid State and Material Science 19 (2015) 19-28.
- [3.16] F. Ernst, *Rutherford Backscattering Spectrometry*, EMSE-515, 2005, page 1-48.
- [3.17] M. Mayer, *SIMNRA User's guide*, Max-Planck-Institut für Plasmaphysik, Boltzmannstr. Garching, Germany.
- [3.18] R. Doolittle, *Algorithms for the rapid simulation of Rutherford backscattering spectra*, Nuclear Instruments and Methods in Physics Research Section B: Beam Interactions with Materials and Atoms 9 (1985) 344 – 351.
- [3.19] M. Thompson, *RUMP: Rutherford backscattering spectroscopy analysis package*. Accessed at <http://www.genplot.com>.

- [3.20] M. Mayer, *SIMNRA: Simulation of RBS, ERD and NRA spectra*. Accessed on <http://www.rzg.mpg.de/mam/>.
- [3.21] J. L'Ecuyer, J.A. Davies and N. Matsunami, *How accurate are absolute Rutherford backscattering yields*, Nuclear Instruments and Methods 160 (1979) 337.
- [3.22] H.H. Andersen, F. Besenbacher, P. Loftager, and W. Möller, *Large-angle scattering of light ions in the weakly screened Rutherford region*, Physical Review A 21(6) (1980) 1891.
- [3.23] N. Barradas and C. Jeynes, *Advanced physics and algorithms in the IBA DataFurnace*, Nuclear Instruments & Methods B 266, 1875–1879.
- [3.24] M. Suga, S. Asahina, Y. Sakuda, H. Kazumori, H. Nishiyama, T. Nokuo, V. Alfredson, T. Kjellman, S. M. Stevens, H. S. Cho, M. Cho, L. Han, S. Che, M. W. Anderson, F. Schüth, H. Deng, O. M. Yaghi, Z. Liu, H. Y. Jeong, A. Stein, K. Sakamoto, R. Ryoo, and O. Terasaki, *Recent progress in scanning electron microscopy for the characterization of fine structural details of nanomaterials*, Progress in Solid State Chemistry 42 (2014) 1-21.
- [3.25] Ruska E, *The development of the electron microscope and of electron microscopy*. Bioscience Reports 7 (1987) 607-629.
- [3.26] Knoll M, and Ruska E, *Das elektronenmikroskop*, Zeitschrift Physik 78 (1932) 318 - 339.
- [3.27] B. Hafner, *Scanning electron microscopy primer*, Characterization Facility, University of Minnesota—Twin Cities (2007).
- [3.28] B. Cheney, *Introduction to scanning electron microscopy*, Department of Materials and engineering, San Jose State University.
- [3.29] S. Hsu, *Handbook of Instrumental Techniques for Analytical Chemistry*, Upper Saddle, New Jersey, Prentice Hall PTR.

[3.30] D.R. Vij, *Handbook of Applied Solid State Spectroscopy*, Springer-Verlag, CBS Publishers, New Delhi, India.

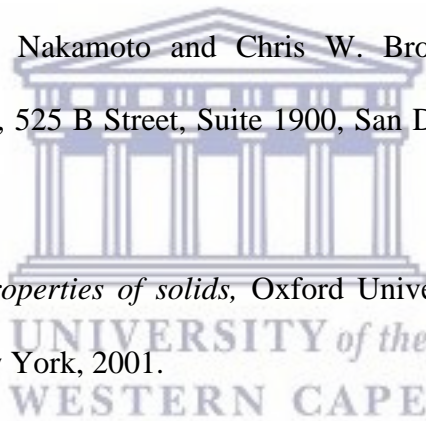
[3.31] J.R. Khoele, *Deposition and structural properties of silicon carbide thin films for solar cells applications*, MSc Thesis, Department of Physics, University of the Western Cape, 2014.

[3.32] M. Malape, *Low-temperature growth of amorphous silicon thin films*, MSc thesis, Department of Physics, University of the Western Cape, 2007.

[3.33] N. Towfie, *Dynamic variation of hydrogen dilution during hot-wire chemical vapour deposition of silicon thin films*, MSc thesis, Department of Physics, University of the Western Cape, 2003.

[3.34] J. R. Ferraro, Kazuo Nakamoto and Chris W. Brown, *Introduction to Raman Spectroscopy*, Academy Press, 525 B Street, Suite 1900, San Diego, California 92101-4495, USA.

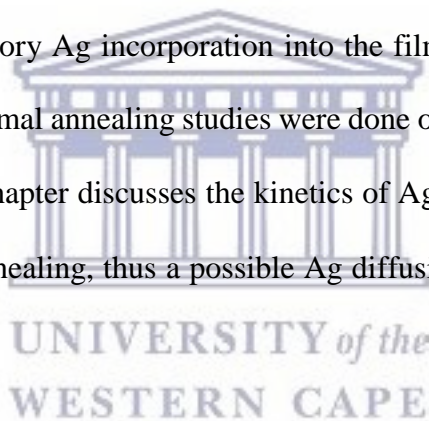
[3.35] A. M. Fox, *Optical properties of solids*, Oxford University Press, Great Clarendon Street, Oxford OX2 6DP, New York, 2001.



Chapter 4 Results and discussion.

4.1 Introduction.

SiC thin films of different thicknesses were fabricated on Si (100) substrate using e-beam deposition. The deposited films were implanted with Ag⁺ ions at three different fluences namely; 2×10^{15} ions/cm², 1×10^{16} ions/cm² and 5×10^{16} ions/cm². The RBS spectra films, implanted at a fluence of 2×10^{15} ions/cm², revealed low Ag incorporation into the films. Annealing these samples at high temperatures (1000 °C – 1300 °C) led to the complete disappearance of Ag peak from the spectra. RBS spectra of films implanted at fluences in the order of 10^{16} showed satisfactory Ag incorporation into the films suitable for heat-treatment studies. Isochronal and isothermal annealing studies were done on films implanted at a fluence of 5×10^{16} ions/cm². This chapter discusses the kinetics of Ag in the films with an increase in temperature and time of annealing, thus a possible Ag diffusion mechanism in the films is proposed.



4.2 Thickness determination from the simulation of RBS spectra.

Fig. 4.1 displays typical SIMNRA simulations of RBS spectra of the as-implanted SiC films; fig. 4.1 (a) and 4.1 (c) display the spectra of films implanted at a fluence of 5×10^{16} ions/cm² and fig. 4.1 (b) and 4.1 (d) those of films implanted at a smaller fluence of 1×10^{16} ions/cm², thus the corresponding intensity of the Ag recorded peaks. The step between the layer's Si surface edge and the interface Si edge profiles the deposited SiC layer. DataFurnace was used to convert RBS spectra data to depth profile information and thus the thicknesses of the

deposited films were obtained by plotting Si depth profiles as shown in fig. 4.2. The depth of the deposited SiC layer is estimated from the depth between the Si edges, indicated by the blue overlaid arrows in fig.4.1. The thicknesses of the deposited films were obtained as 100 nm, 225 nm, 223 nm, and 294 nm for the layers shown in fig. 4.1 (a) – fig. 4.1 (d) respectively. DataFurnace is not sensitive to low atomic number elements and thus the depth profiles of carbon and oxygen could not be extracted.

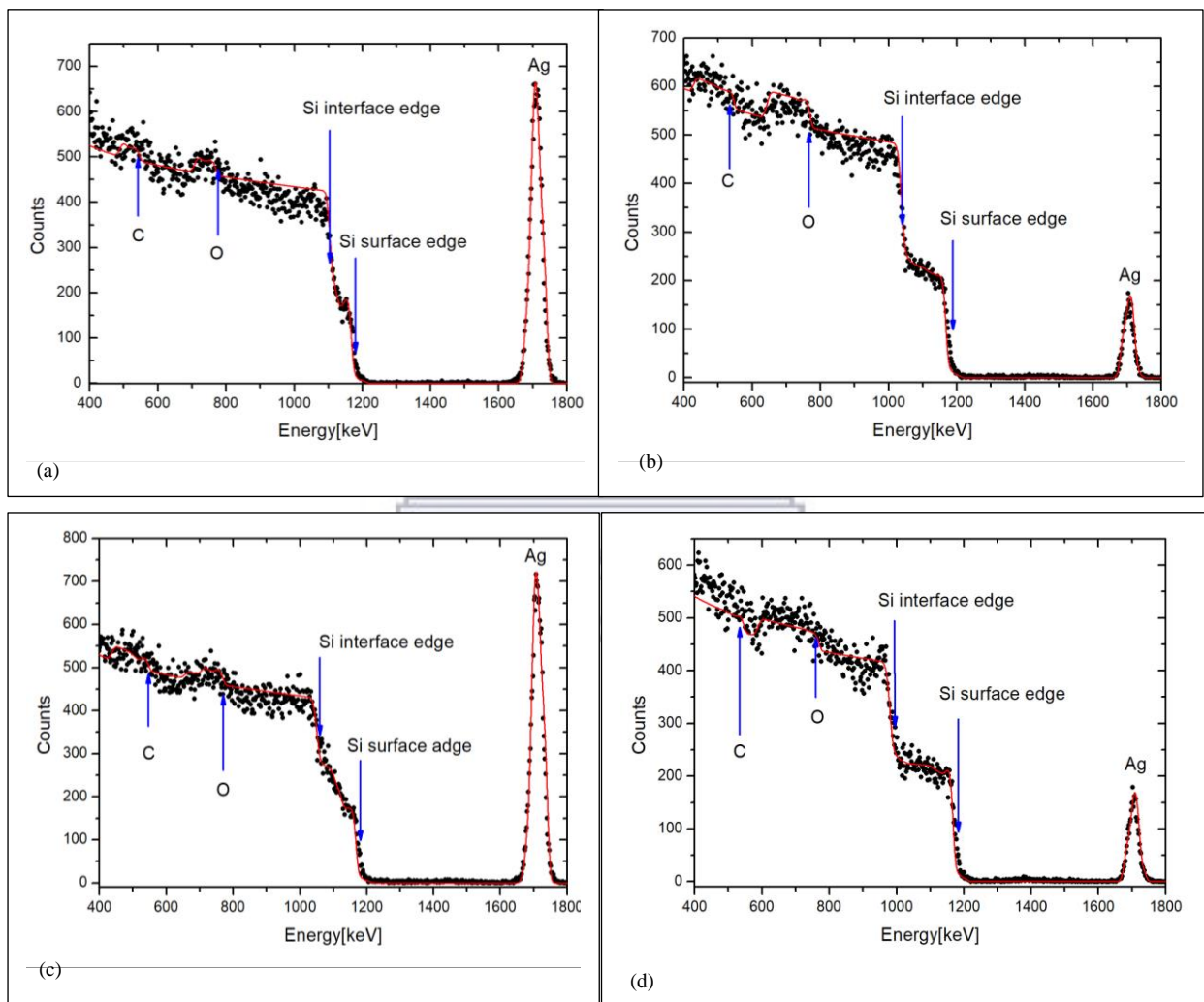
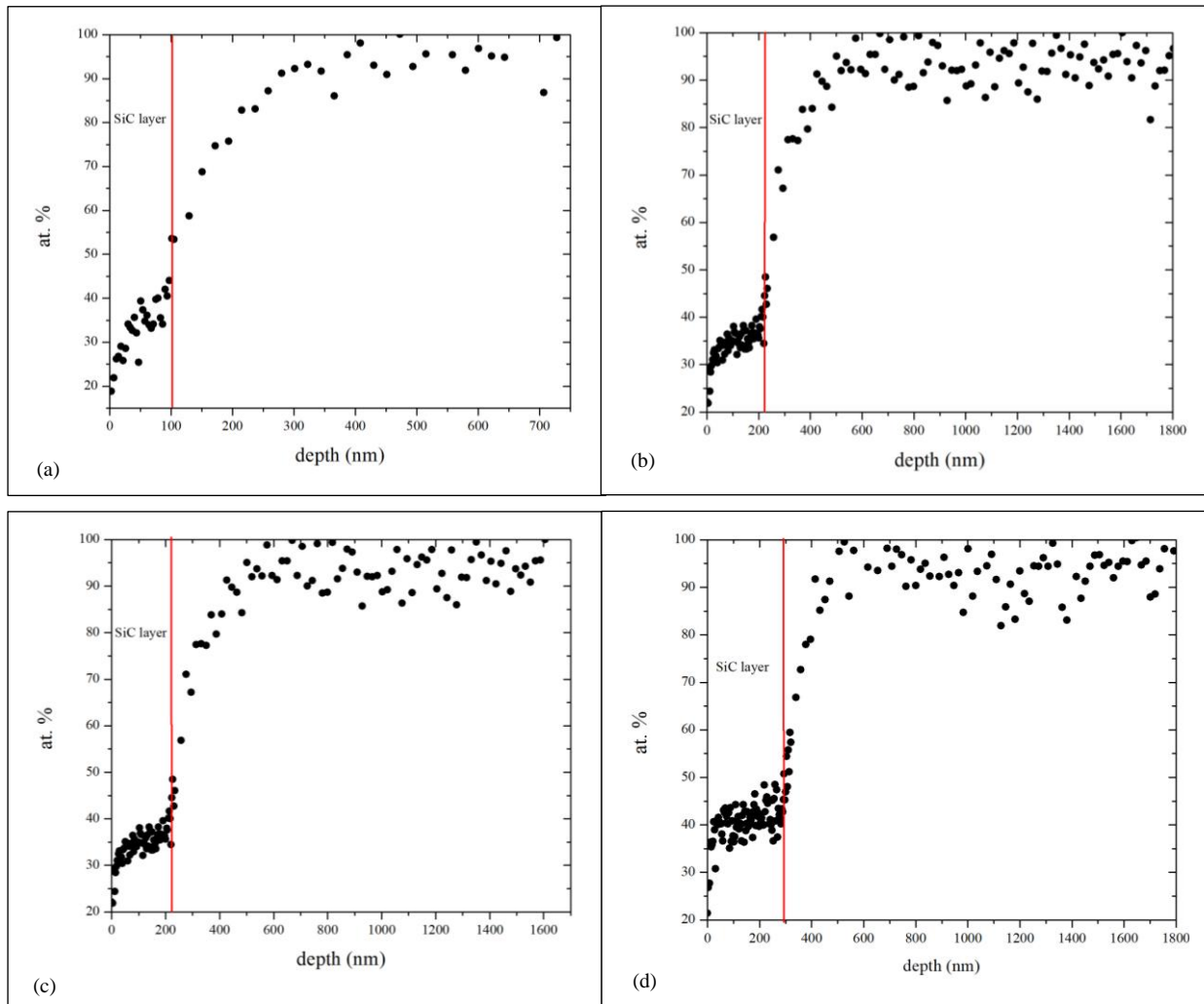


Figure 4.1: Typical SIMNRA simulations of RBS spectra of as-implanted SiC films (a) & (c): at fluence of 5×10^{16} ions/cm² (b) & (d): at a fluence of 1×10^{16} ions/cm². The dotted plots are the experimental spectra and the red solid curves are the simulated ones.



UNIVERSITY of the
WESTERN CAPE

Figure 4.2: Si-depth profiles for the RBS spectra shown in fig 4.1(a) – fig 4.1(d).

Table 4.1 lists the conventional Ids of as-implanted samples; the same sample labelling applies to RBS spectra displayed in fig. 4.1 and fig. 4.3. Rows S_1 and S_3 display the data of films implanted with 5×10^{16} ions/cm² while rows S_2 and S_4 were implanted with 1×10^{16} ions/cm² fluences.

Table 4.2 shows the computed elemental concentration (in weight %) in the films from the simulations in fig. 4.1. Correspondingly, less Ag concentration is recorded in samples S_1 and S_3 implanted with lower fluence. The O in the films can be attributed to residual oxygen in the chamber during deposition and/or in the annealing chamber.

Table 4.1: Conventional sample ids and their description.

Sample	Thickness (nm)	Fluence (ions/cm²)	Fig.
S ₁	100	5×10^{16}	4.1 (a)
S ₂	225	1×10^{16}	4.1(b)
S ₃	223	5×10^{16}	4.1 (c)
S ₄	294	1×10^{16}	4.1 (d)
S ₅	294	2×10^{15}	4.3

Table 4.2: Elemental composition (average weight %) of the as-implanted SiC films shown in fig. 4.1; S₁ & S₃ for higher and S₂ & S₄ for lower fluences respectively.

Element	S₁ (Wt. %)	S₂ (Wt. %)	S₃ (Wt. %)	S₄ (Wt. %)
C	14,53	22,8	17,86	22,32
O	16,31	21,2	10,71	10,54
Si	40,46	52,2	51,34	64,26
Ag	28,7	3,8	20,09	2,88

4.3 The effect of fluence on the microstructure of silicon carbide films.

The results discussed in this section are from a SiC film of ~294 nm in thickness; that was deposited on Si (100) substrates from a SiC target. It is part of an earlier implanted series where

a non – optimized fluence of 2×10^{15} ions/cm² was used. The 110 keV energy of Ag⁺ ions will be kept constant in all implanted films. RBS experiments in this section were done using 2 MeV He⁺ ions provided by the Tandem accelerator at iThemba LABS, Gauteng. Fig. 4.3 shows the typical RBS spectrum of the deposited films that were simulated using SIMNRA for atomic concentration and thickness determination; it displays a relatively low Ag incorporation in the layers. Backscattered surface energies of Ag, Si, oxygen, and carbon are estimated at 1741 keV, 1170 keV, 769.5 and 547.3 keV, respectively. The conversion from channel number to energy scale was done using AuNi/AlO/C standard. The isochronal annealing studies between 1300 °C and 1000 °C have shown a complete disappearance of Ag signal in the RBS spectra. Ag is very volatile above 960 °C (its melting point temperature) temperatures, and it could have easily evaporated off the surface. Fig. 4.4 shows a typical EDX spectrum of the films and Ag well below the detection limit of the system. The subsequent annealing studies were thus restraint to temperatures below 1000 °C.

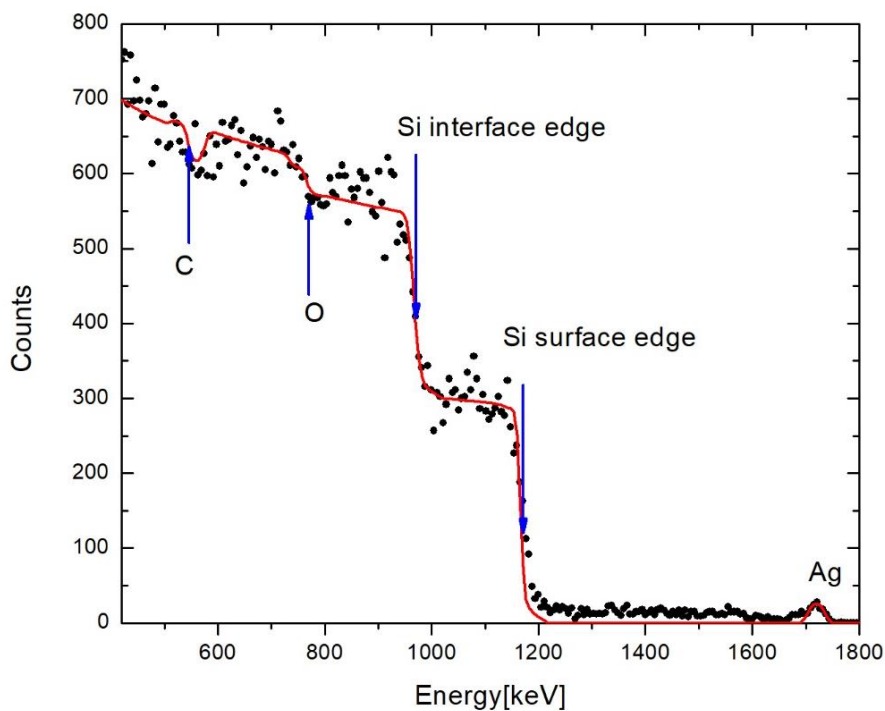


Figure 4.3: Typical RBS simulated spectra of the films implanted with Ag ion fluence of 2×10^{15} ions/cm².

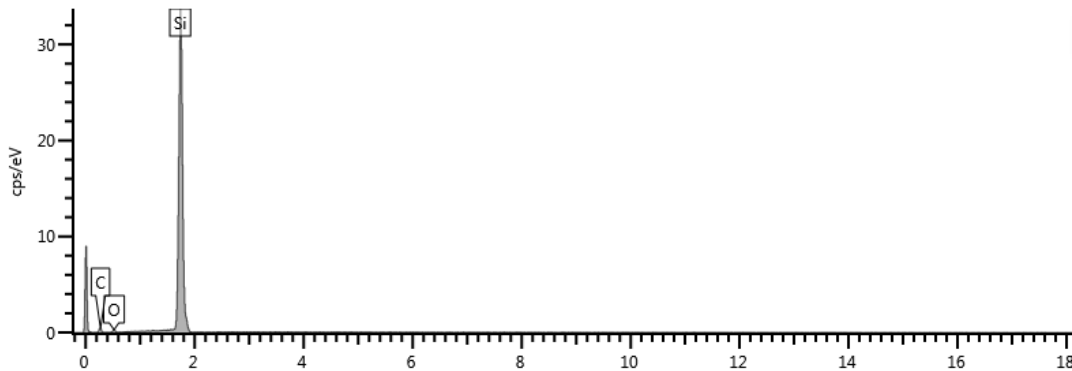


Figure 4.4: Typical EDX spectrum of the films annealed (previously implanted at 2×10^{15} ions/cm²).

Elemental composition observed in as-implanted S₅ is listed in table 4.3 for RBS and EDX. No contaminant element was detected by both techniques. The films have a high Si weight percentage, in part due to the strong substrate component, and a much lower carbon embedded in the matrix coupled with only trace amounts of oxidation. The results from the two techniques are not in good agreement. For Si data for instance, one has to take into account that the interaction volume in EDX does include part of the substrate as the films were thin. As for carbon, EDX tends to overestimate carbon content due to unavoidable contamination especially when the samples were not plasma cleaned and / or when they are electrically charging; the Ag was simply too low to be detected by EDX in this sample. Due to the above discussion, the oxygen concentration had to be underestimated for the overall elemental composition to add to 100%. It can be concluded the RBS data are most reliable because the surface component is always removed from the data reported and the Si substrate interface is easily noticed in our simulations; the RBS data presented here are those exclusively from the bulk of the SiC layer.

Table 4.3: Typical elemental composition in the films; RBS and EDX elemental concentration of the sample (S₅) is given.

Element	RBS (Weight %)	EDX (Weight %)
C	21,25	27,21
O	16,61	3,90
Si	61,82	68,89
Ag	0,32	0,00

During implantation, the whole sample is implanted except the area where the sample is held. Fig. 4.5 present typical SEM micrographs of the implanted and non-implanted areas of the as-implanted film (S₅). Fig. 4.5(a) indicate a clear contrast between the area that was implanted, marked with an X, and the non-implanted area, marked with a Y. Fig. 4.5 (b) shows the non-implanted, and fig. 4.5 (c) the implanted region of the films with higher magnification. The non-implanted area shows a grainy surface suggestive a crystalline network, whereas the implanted region has a smooth surface appearance suggesting an amorphous surface. Thus, it can be concluded that bombardment by ions during implantation induces disorder in the film network.

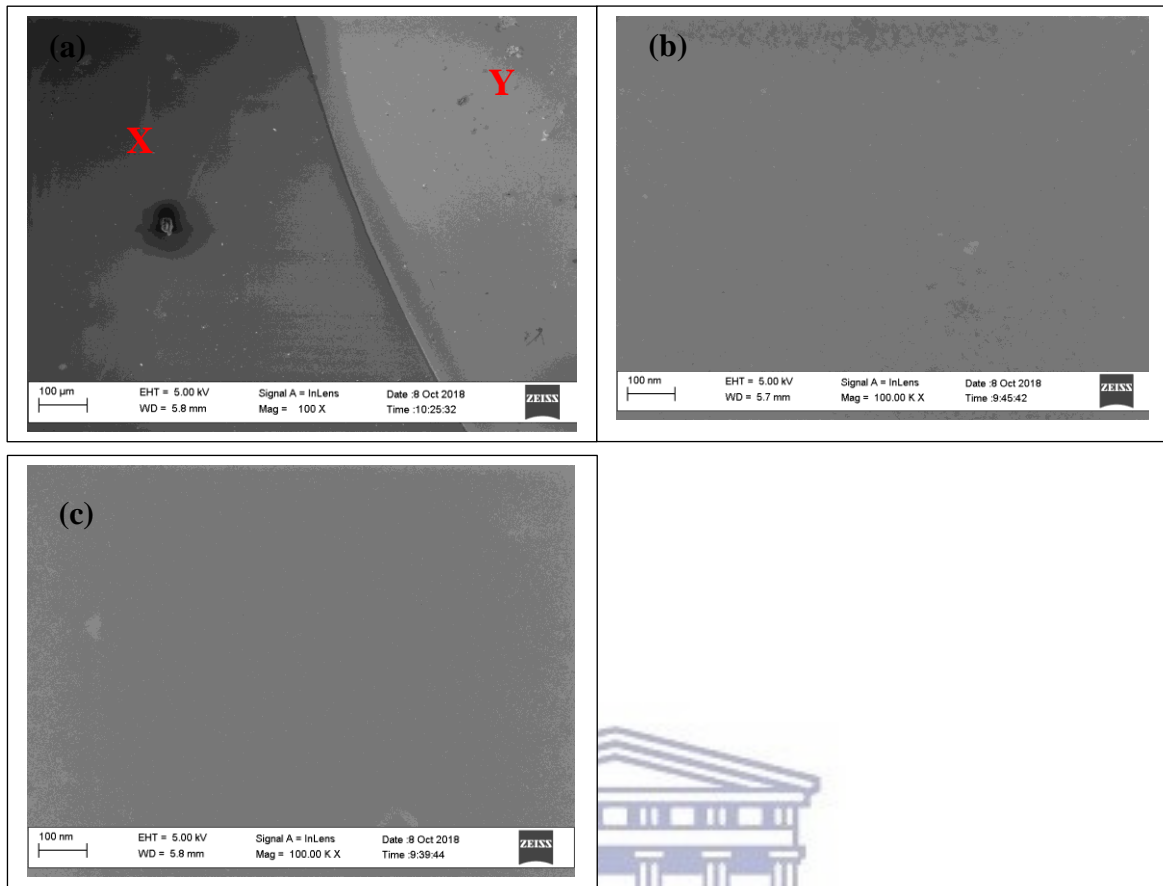


Figure 4.5: SEM micrographs showing (a) implanted and non-implanted region of the films indicated by X, and Y respectively, (b) non-implanted area and, (c) implanted area at a higher magnification.

4.4 Annealing studies on Ag implanted silicon carbide films.

4.4.1 The stability of Ag in SiC deposited films at low temperatures.

Fig. 4.6 shows sample S₅ real-time RBS contour plot map corresponding to a temperature ramp from RT to 600 °C. The sample was initially ramped at a faster rate of 20 °C /min between room temperature (RT) and 300 °C and the ramp rate was decreased to 3 °C /min between 300

°C and 600 °C. The temperature was then held for a further 10 minutes at 600 °C prior to subsequent cooling. The colour legend on the right of the figure illustrates the number of counts. We notice that the yield of Ag (indicated by an overlaid red arrow) does not change throughout the temperature ramp. We, therefore, conclude that Ag is stable until 600 °C, the highest temperature that the heater in the system used can achieve.

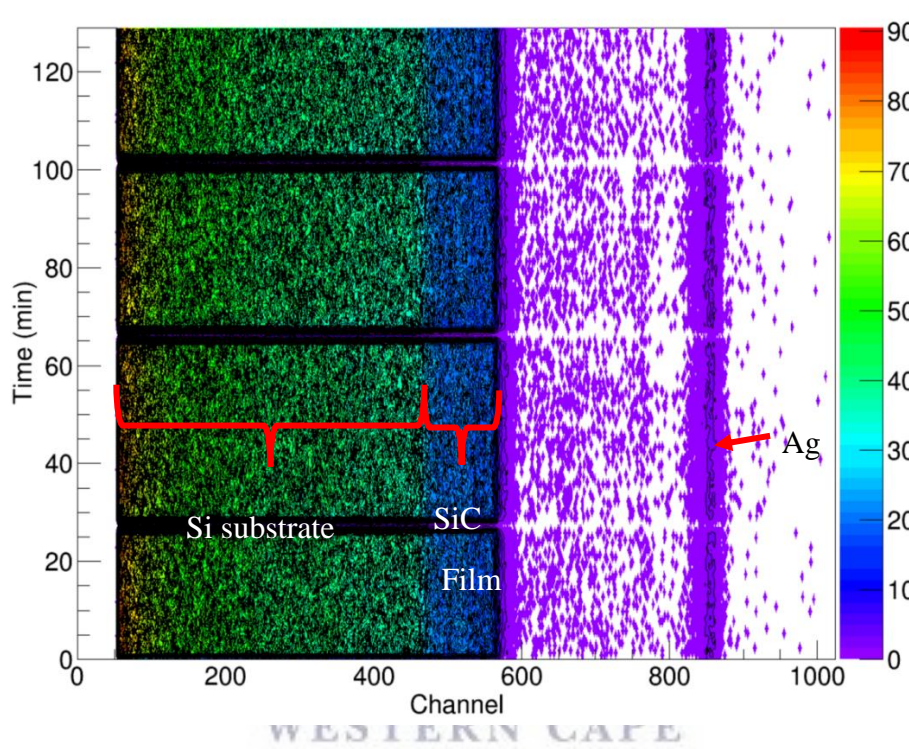


Figure 4.6: Real-time RBS contour plot map corresponding to a temperature ramp from RT to 600 °C.

4.4.2 Isochronal annealing studies using SEM/EDX.

The deposited films discussed from this section onwards were deposited from a commercial high purity hot pressed SiC sheet. Some films were implanted at a fluence of 1×10^{16} ions/cm² and others at 5×10^{16} ions/cm². RBS experiments were done using 2 MeV He⁺⁺ ions provided

by the Tandetron accelerator at iThemba LABS, Cape Town, South Africa. For energy calibration, AuCo/SiO₂/Si standard was used.

Table 4.4 lists the conventional Ids of isochronally annealed samples; the same sample labelling applies to SEM micrographs displayed in fig. 4.7 and RBS spectra displayed in fig. 4.9.

S₆ – S₉ were isochronally annealed from 650 °C - 750 °C, respectively, for 1 hour under N₂ environment.

Table 4.4: Conventional sample ids and their description.

Sample	Thickness (nm)	Fluence (ions/cm ²)	Isochronal annealing (1 hr.)
S ₆	~100	5×10^{16}	650 °C
S ₇	~100	5×10^{16}	750 °C
S ₈	~100	5×10^{16}	850 °C
S ₉	~100	5×10^{16}	950 °C

Fig. 4.7 (a), (b), (c) and (d) shows typical SEM images of samples S₁, S₇, S₈, and S₉ respectively. The SEM micrographs reveal a relatively smooth deposition of the SiC across the scanned area. There is no significant difference between the as-implanted films and the film annealed at 750°C, i.e. the heat treatment does not appear to induce any change in the microstructure of the films at this stage.

The film annealed at 850 °C shows a change in microstructure revealing a grainy film surface. Interestingly, the film annealed at 950 °C recovers its smoothness. This contrast in the microstructure is interpreted in light of the crystallization of the network at 850 °C accompanied with a possible out-diffusion of Ag through the formed grain boundaries; once

the metal has completely out-diffused, further anneal results in the recovery of the network, hence the smooth surface observed in fig. 4.7 (d) corresponding to the film annealed at 950 °C for one hour.

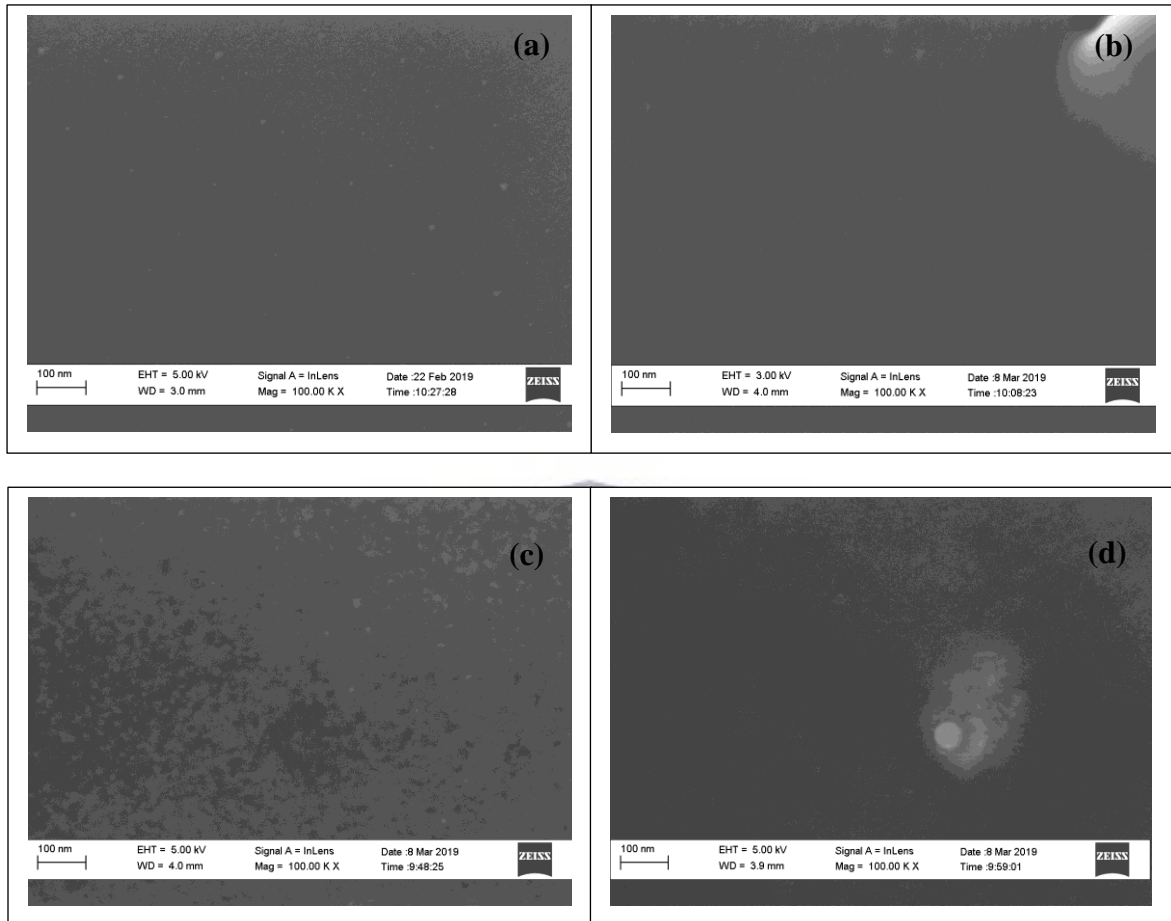


Figure 4.7: SEM top-view micrographs of samples (a) S₁, (b) S₇, (c) S₈, and (d) S₉.

Fig. 4.8 shows a typical EDX spectrum of samples S₇, S₈, and S₉ plotted in black, red and blue, respectively. S₇ and S₈ show the similar elemental composition in Si, O and C. The EDX of S₉ is characterized by the absence of Ag. This is likely due to the out-diffusion of the Ag from the films upon higher temperature treatment. The elemental concentration (in weight %) is provided in table 4.5. As it is shown, Ag concentration in the films decreases as the annealing temperature is increased, consistently with the behaviour of its peak in fig. 4.8. The intense Si peak is due to the contribution of the c-Si substrate.

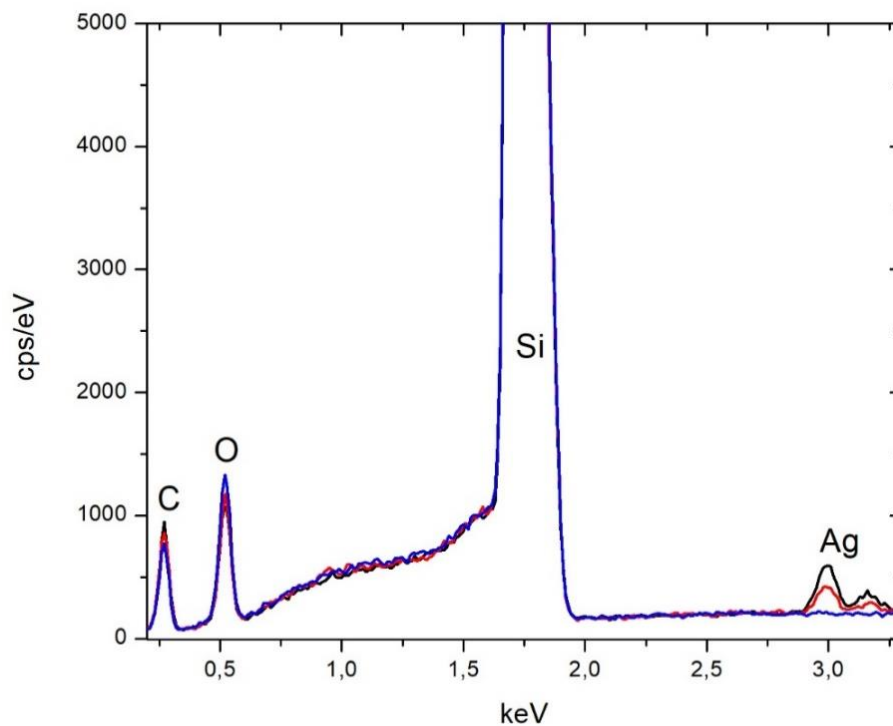


Figure 4.8: EDX spectrum of samples S₇, S₈, and S₉ plotted in black, red, and blue respectively.

Table 4.5: Elemental composition corresponding to the micrographs shown in fig. 4.8.

	S ₁ (Wt. %)	S ₇ (Wt. %)	S ₈ (Wt. %)	S ₉ (Wt. %)
Element				
C	17,99	17,78	17,29	15,63
O	3,77	4,22	4,37	4,99
Si	76,35	76,28	77,33	79,39
Ag	1,89	1,72	1,01	0

4.4.3 Isochronal annealing studies using RBS.

Fig. 4.9 (a) - 4.9 (d) shows RBS spectra of samples S_6 - S_9 respectively. There is no significant change in the spectra of the as-implanted S_1 and the S_6 - S_7 annealed films. However, S_8 shows a decrease in the number of counts and a change in the implantation profile of Ag peak is observed suggesting that Ag is mobile in the films at 850 °C. At 950 °C the Ag has completely diffused out of the films and these results are consistent with EDX findings shown in fig. 4.8 and table 4.5.

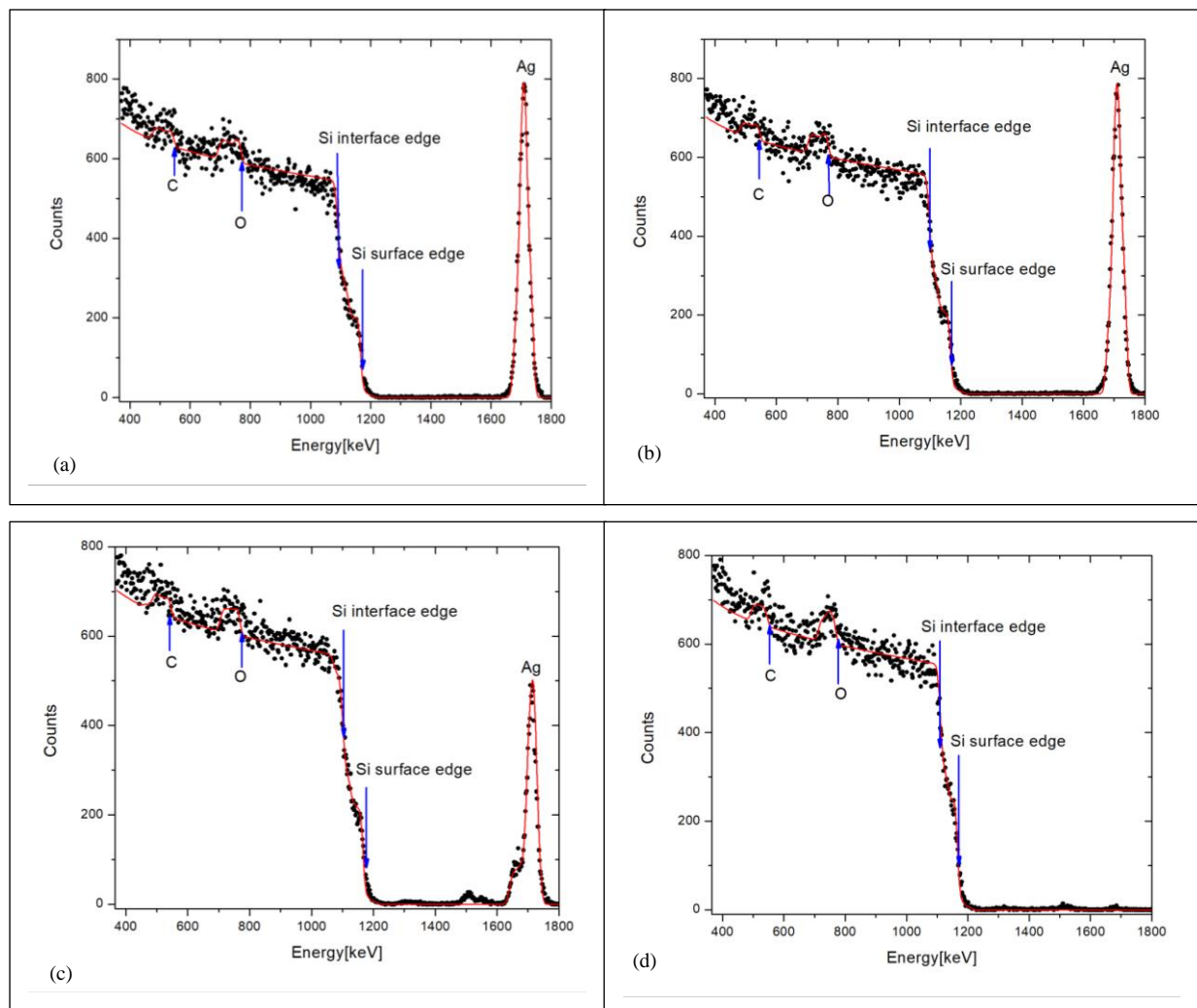


Figure 4.9: Typical SIMNRA simulated RBS spectra of samples (a) S_6 , (b) S_7 (c) S_8 , and (d) S_9 . The dotted plots are the experimental spectra and the red solid curve is the simulated spectra.

Table 4.6 lists the overall elemental concentration in weight percent in the samples S₆ – S₉. A gradual decrease in Ag content is observed with the increase in the annealing temperature; this suggests that part of the implanted silver has out-diffused and/ or it has spread out deeper in the films in minute quantities by cross section so that it is under the detection limit. The last row displays the integrated intensity values of the Ag peak indicating its content in the samples. The decrease in the calculated integrated intensities profile and this is interpreted as the depletion of Ag from the films; this gives credence to our assumption of Ag out-diffusion. The profile of Ag peak integrated areas as a function of annealing temperature is plotted shown fig. 4.15.

Table 4.6: Elemental composition of the isochronally annealed SiC films shown in fig. 4.9.

	S ₆ (wt. %)	S ₇ (wt. %)	S ₈ (wt. %)	S ₉ (wt. %)
Element				
C	15,97	15	16,59	17,98
O	17,2	17,02	20,18	27,43
Si	38,24	39,88	45,37	54,59
Ag	28,6	28,1	17,85	0
Integrated Area	30273	28514	20894	264

4.4.4 Isothermal annealing studies by RBS.

Isothermal annealing studies were done at 850 °C to further investigate the diffusion of the implanted ions in the deposited films. Table 4.7 lists the conventional Ids of isothermally annealed samples; the same sample labelling applies to RBS spectra displayed in fig. 4.10. S₁₀,

S₁₁, and S₁₂ were for 20 minutes, 40 minutes, and 100 minutes respectively at 850 °C under N₂ environment.

Table 4.7: Conventional Ids of isothermally annealed samples and their description at 850°C.

Sample	Thickness (nm)	Fluence (ions/cm²)	Isothermal annealing (850 °C)
S ₁₀	223	5×10^{16}	20 minutes
S ₁₁	223	5×10^{16}	40 minutes
S ₁₂	223	5×10^{16}	100 minutes

Fig. 4.10 (a) shows the as-implanted S₃ and fig. 4.10 (b) - 4.10 (d) show the isothermally annealed S₁₀ - S₁₂ respectively. Table 4.8 displays the overall elemental concentration in weight percent in the samples S₃, and S₁₀ – S₁₂. A gradual decrease in Ag content is observed with the increase in the annealing time; this further substantiates our assumption that part of the implanted silver has out-diffused and/or it has spread out deeper in the film in minute quantities by cross section so that it is under the detection limit. The last row displays the integrated intensity values of the Ag peak indicating its content in the samples. A decrease in the calculated intensities is observed and this is interpreted as the depletion of Ag from the films; this gives credence to our assumption of Ag out-diffusion. The profile of Ag integrated areas-values as a function of annealing time is plotted in fig. 4.18.

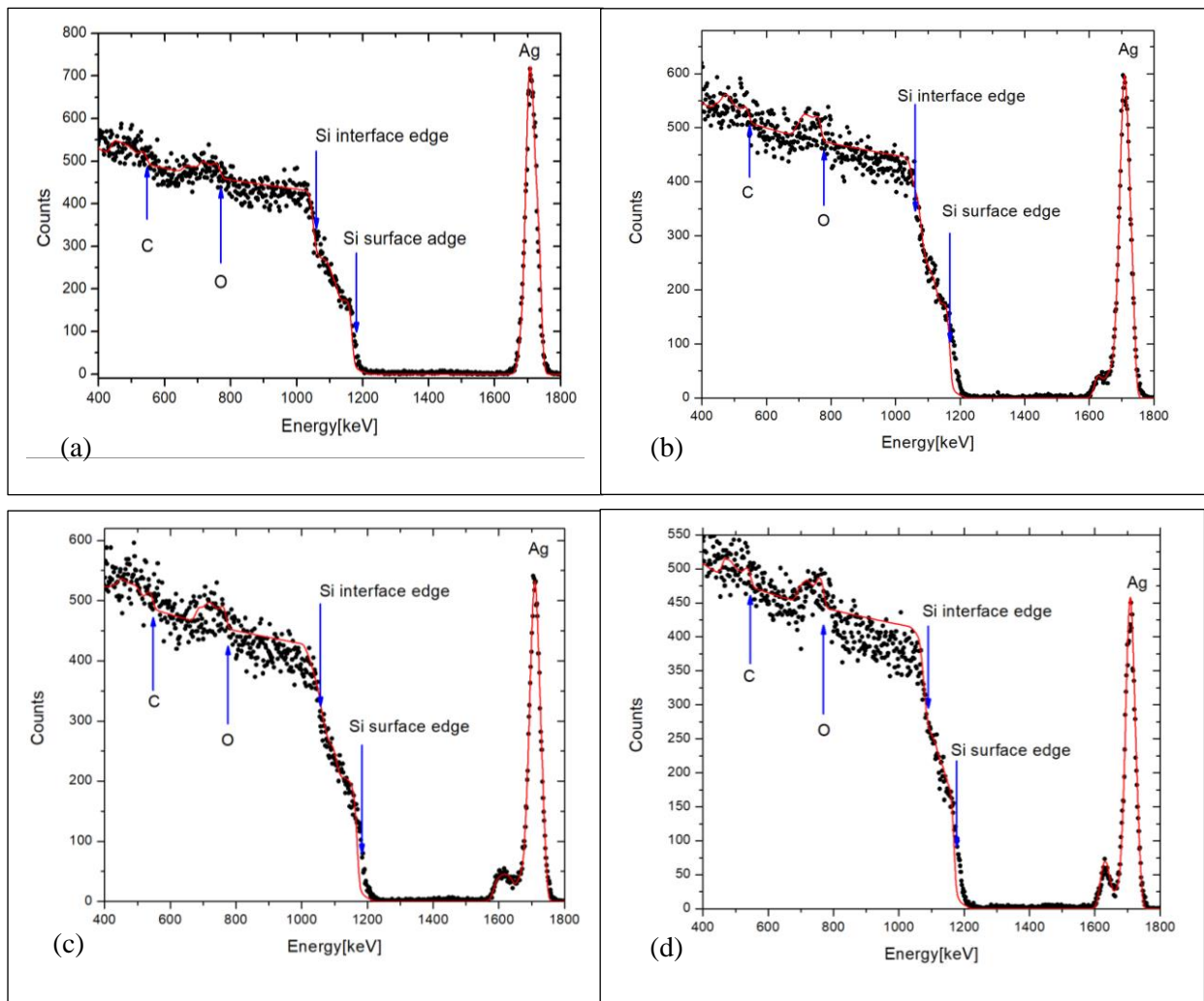


Figure 4.10: Typical SIMNRA simulated RBS of samples (a) S₃, (b) S₁₀, (c) S₁₁, and (d) S₁₂.

The dotted plots are the experimental spectra and the red solid curve is the simulated spectra.

Table 4.8: Elemental composition of the isothermally annealed SiC films shown in fig. 4.10.

	S ₃ (wt. %)	S ₁₀ (wt. %)	S ₁₁ (wt. %)	S ₁₂ (wt. %)
Element				
C	17,86	14,99	15,92	11,92
O	10,71	11,27	11,48	10,48
Si	51,34	56,23	56,22	64,04
Ag	20,09	17,51	16,38	13,54

Integrated	27599	27257	23624	17721
Area				

4.6 Ag depth profiling.

Fig. 4.11 shows a typical implantation profile simulation obtained with SRIM-2013[4.1] code assuming displacement energies of 37 eV and 69 eV for Si and C atoms, respectively [4.2]. The theoretical estimated straggling is 11.2 nm, the kurtosis ($\beta = 2.7024$) and skewness ($\gamma = 0.932$) are almost Gaussian ($\beta = 3, \gamma = 0$) [4.1]. SRIM simulations predicted an implantation Ag projected the range of 40.6 nm into the films assuming a stoichiometric SiC. Fig. 4.12 shows Ag depth profile of S₄ layers as obtained from DataFurnace, it reveals that Ag is implanted at a depth of ~55 nm. The discrepancy is due to the fact that both the mass density and the microstructure of the deposited SiC layers are different from the stoichiometric crystalline SiC whose published tabulated data were used in generating the SRIM graph.

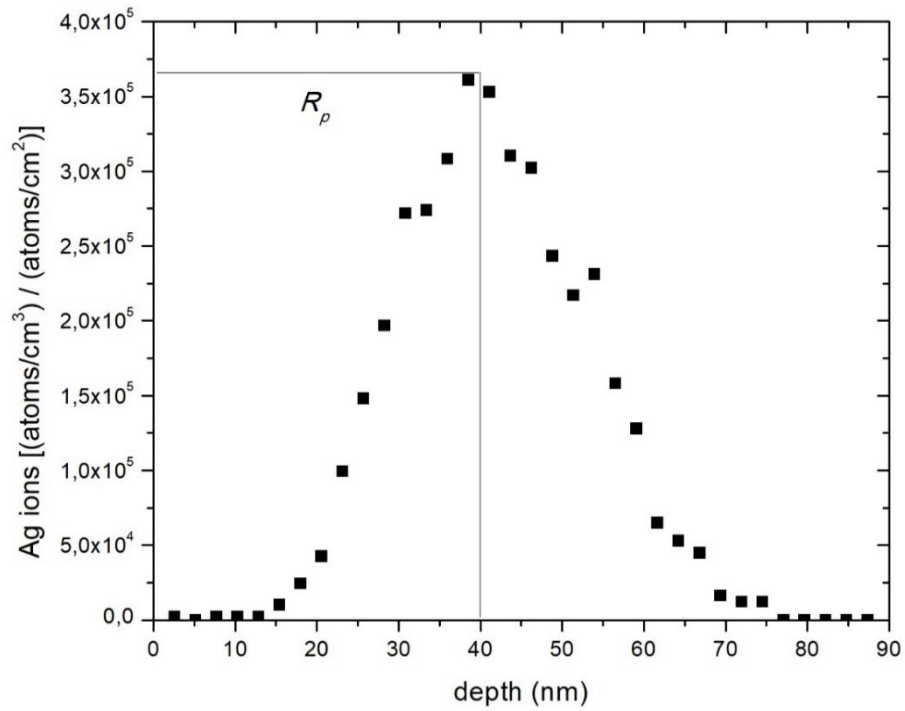


Figure 4.11: A typical implantation profile simulated with SRIM-2013.

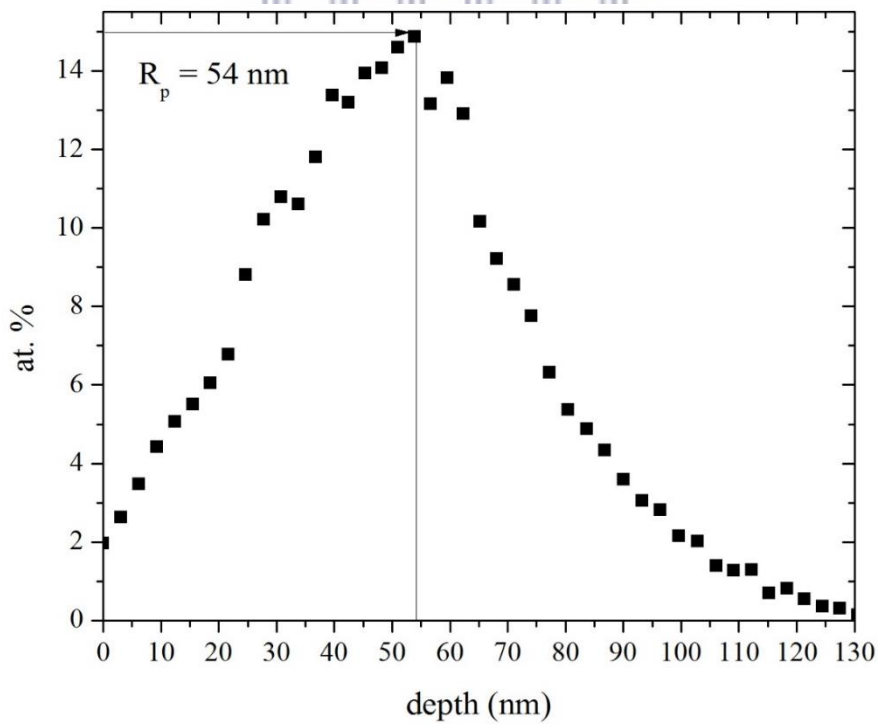


Figure 4.12: Ag depth profile of sample S₃, extracted from DataFurnace.

Fig. 4.13 shows Ag RBS spectra of S₁, S₆, S₇, S₈, and S₉ plotted in black, red, green, blue, and magenta, respectively. The profile of S₁, S₆, S₇, have more or less similar intensities and same profile. This suggests that the implanted Ag was stable up to ~750 °C. The spectrum of S₈ has shown that the Ag peak decreased in intensity and, as discussed in the last section displayed shoulder-like features deeper in the films. This temperature can then be ascribed as the onset of Ag diffusion in the deposited SiC films. It has been reported previously [4.3] that Ag and Si do not form a silicide but Ag becomes unstable above 840 °C in Si network [4.3]. Given the observed high Si concentration in the deposited films, the diffusion of Ag would be similar in Si-rich SiC materials. The RBS spectrum of S₉ did not show any detectable Ag in the films and these results are consistent with EDX results (fig. 4.8 and table 4.4).

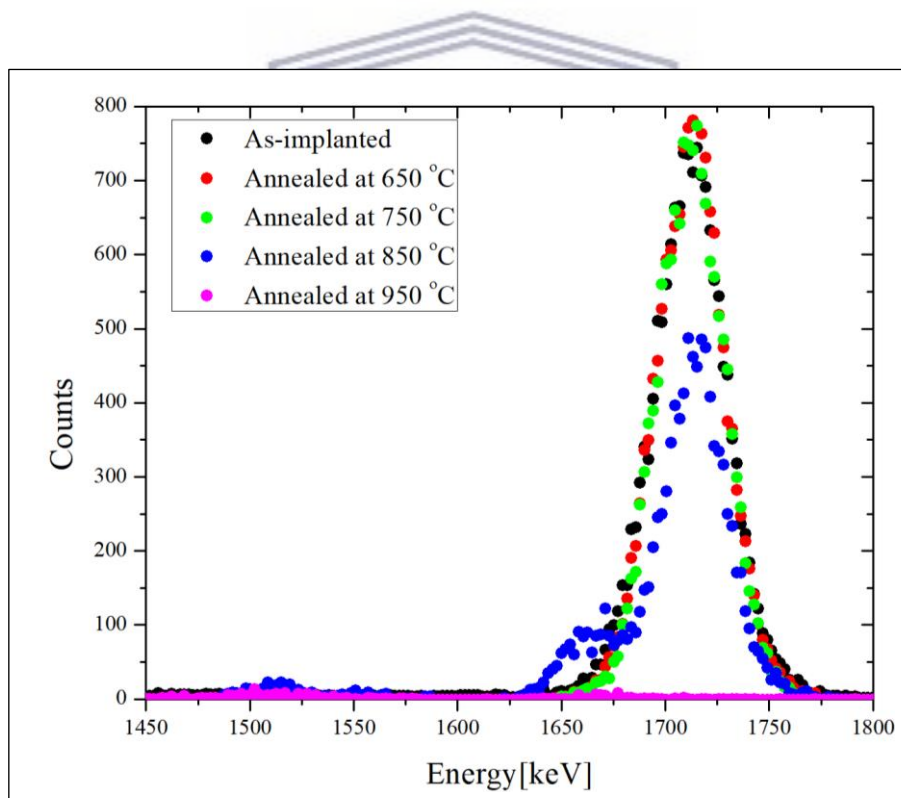


Figure 4.13: Ag RBS profile of S₃, S₆, S₇, S₈, and S₉ plotted in red, green, blue and magenta, respectively.

Fig. 4.14 shows the corresponding Ag depth profiling corresponding to spectra shown in fig. 4.13 in the same colour code. At 850 °C there is a huge Ag loss with trace amounts found

deeper into the sample. The small shoulders on the Ag peak towards the interface with the substrate and its asymmetric profile towards the surface suggest that they are competing in and out-diffusion mechanisms. . K. Fukuda *et al.* [4.4] argued that the appearance of the peaks in the release rate below 1200 °C in SiC, suggests that the release is controlled by the ejection from the trapping sites rather than by the diffusion only. On the other hand, Hart *et al.* [4.5] showed in the luminescence experiments that lattice defects in SiC induced by ion bombardment were almost completely annealed at about 1000 °C. Thus, we argue that the shoulders observed in fig. 4.13 and fig. 4.14 can be attributed to Ag which is ejected from the Si trapping sites during the reconstruction of the network that appears to be complete around 950 °C in our experiments, according to the SEM results presented in fig. 4.7.

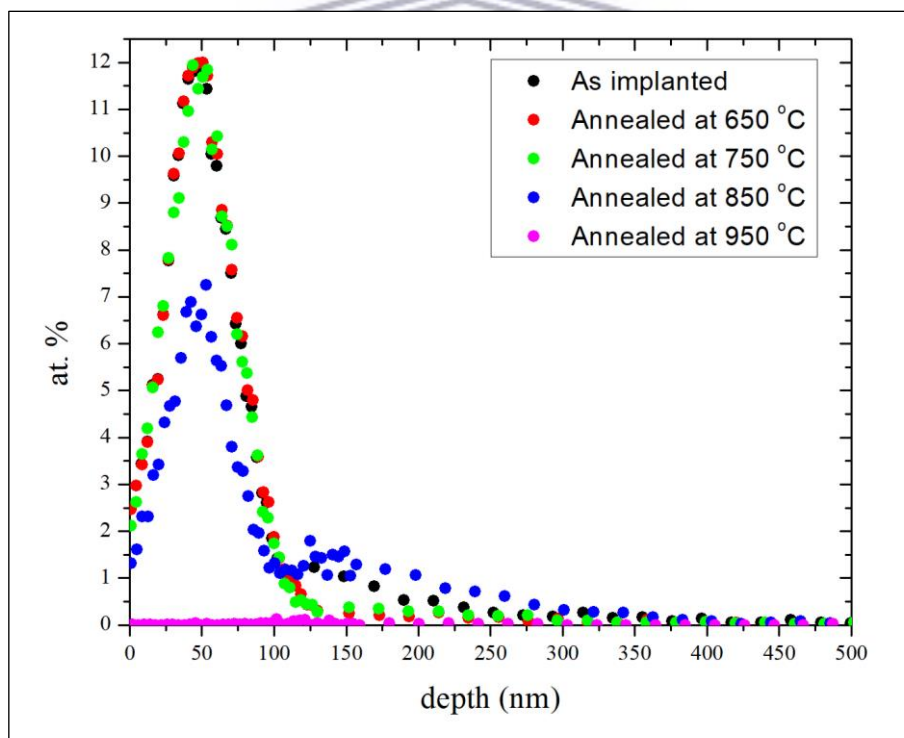


Figure 4.14: Ag depth profiling corresponding to spectra shown in fig. 4.13 in the same colour code.

Fig. 4.15 displays the relation between Ag integrated areas of spectra shown in fig. 4.13 as a function of annealing temperature. The constructed profile exhibits an almost exponential Ag decay in the films with an increase of annealing temperature. It can be seen that from RT to 750 °C there is little release of Ag from its implantation site i.e. slow diffusion kinetics. The rate of release accelerates in the 750 °C – 850 °C, temperature range. Finally, a sharp depletion of Ag content is observed from 850 °C to 950 °C where no more Ag is detected by RBS, in agreement with EDX findings.

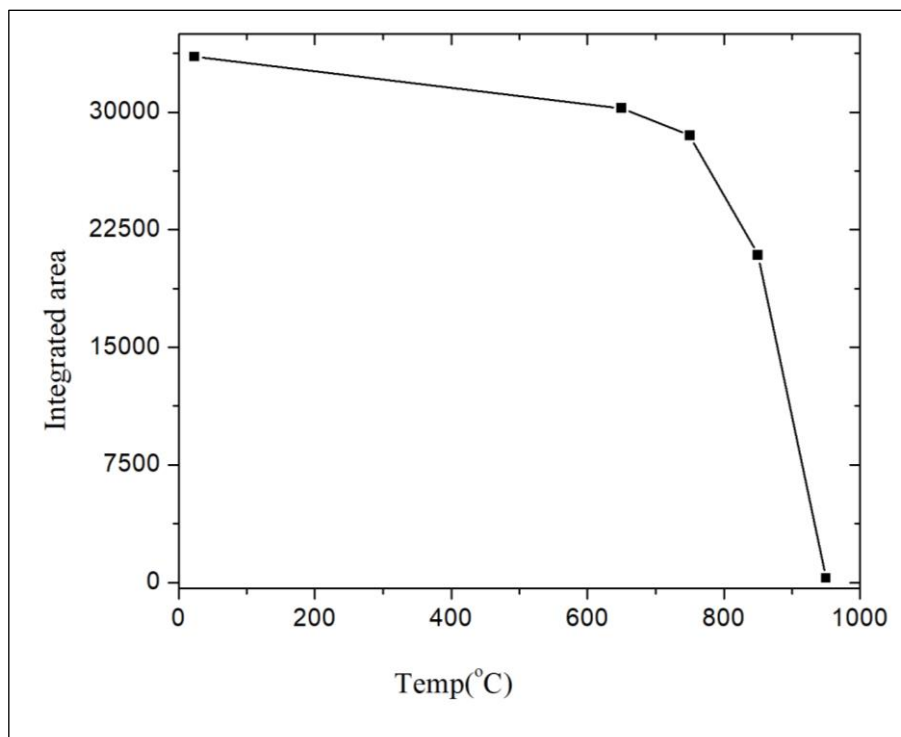


Figure 4.15: The profile of Ag peak integrated areas from fig. 4.13 as a function of annealing temperature. (The broken lines are as guide to the eye).

Fig. 4.16 displays Ag RBS implantation profiles of S₃, S₁₀, S₁₁, and S₁₂ plotted in black, red, green, and blue. Fig. 4.17 gives their respective Ag depth profiles in the samples. Fig. 4.18 displays the relationship between Ag integrated areas of spectra shown in fig. 4.16 as a function of annealing time. The profile suggests an almost steady decay of Ag in the films with the increase of annealing time in the range probed. This is rather expected as the diffusion

coefficient is the same at a given annealing temperature while it does increase as the annealing temperature is increased, thus the exponential decay observed in fig. 15.

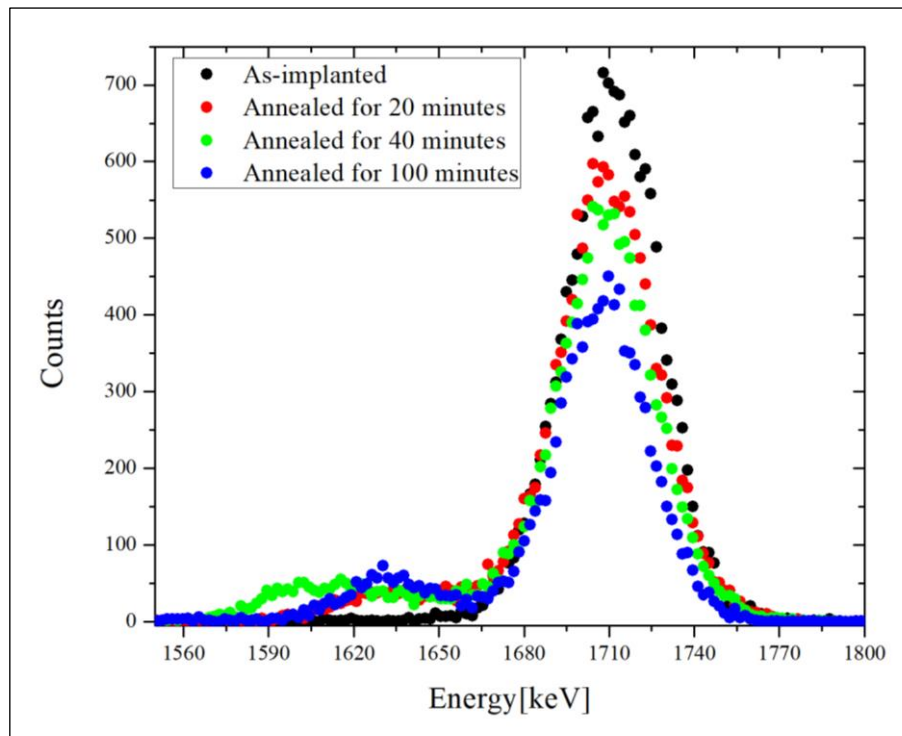


Figure 4.16: RBS spectra of sample S₃, S₁₀, S₁₁, and S₁₂ plotted in black, red, green, and blue.

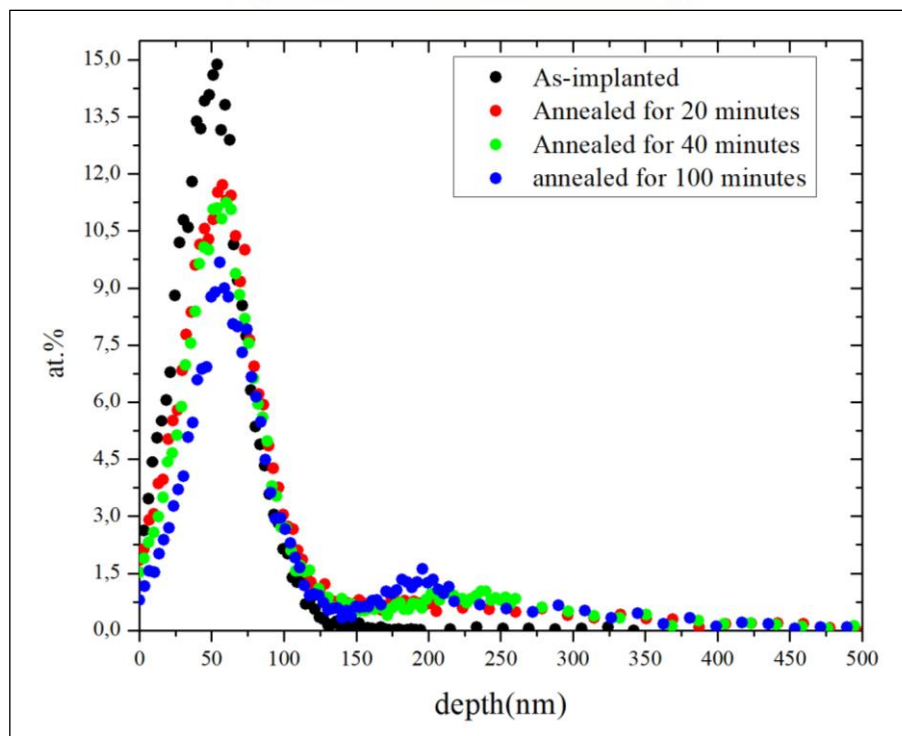


Figure 4.17: the corresponding Ag depth profiles in the same colour codes as in fig. 4.16.

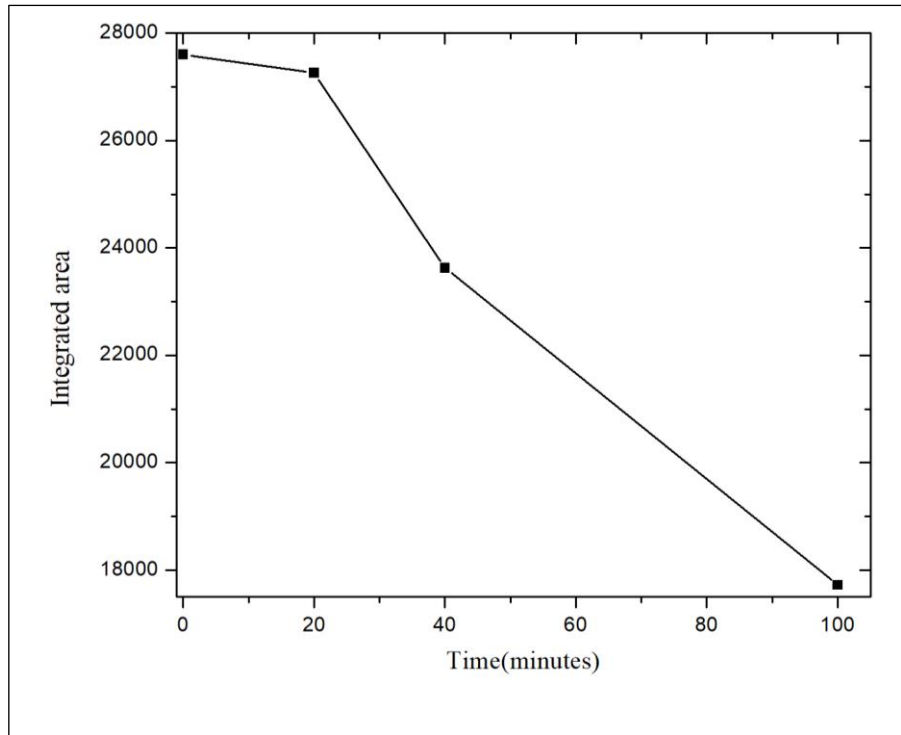


Figure 4.18: The profile of Ag integrated areas as a function of annealing time.



4.7 Proposed mechanism of diffusion.

Although no direct systematic studies on defect formation have been done in this study, the FTIR results displayed in fig. 4.19 can give a qualitative approach to the mechanism of Ag diffusion: the increase in oxidation as the temperature increases suggests a more defective and porous network; on the other hand the narrowing of the peak due SiC stretching bonds at around 800 cm^{-1} is interpreted as a re-arrangement of the network in polycrystalline SiC grains in the Si matrix. The Ag diffusion can thus be explained in terms of leakage through pores and grain boundaries as proposed previously by Friedland [4.6] and Gerzack [4.7].

Fig. 4.19 displays FTIR spectra of as-implanted and selected isochronally annealed films. Three main vibration peaks have been observed and their assignment is indicated on the figure. The noticeable feature is the narrowing of the peak due to SiC at around 800 cm^{-1} and this is

interpreted as a re-arrangement of the network in polycrystalline SiC grains in the Si matrix. We note also a broad peak between 900 cm^{-1} to 1100 cm^{-1} , it is related oxygen related vibrations; it can be deconvoluted into two components, one centered at $\sim 960\text{ cm}^{-1}$ due to Si-O-C and a second centered ~ 1070 due to SiC stretching vibration mode. It is interesting to see that this peak shifts to higher energy (above 1000 cm^{-1}) in the sample annealed at $850\text{ }^{\circ}\text{C}$ concomitantly with the narrowing of the 800 cm^{-1} peak as well the appearance of another oxygen related peak at $\sim 460\text{ cm}^{-1}$ that we assign to Si-O-Si rocking vibration mode. Thus the rearrangement of the network consists in the breakage of the Si-O-C bonds, the C and Si crystallize in SiC while the only remaining O related peaks come from different modes of SiO. Another small peak was observed at $\sim 1400\text{ cm}^{-1}$; it is assigned to C-C and it persists upon high temperature anneal.

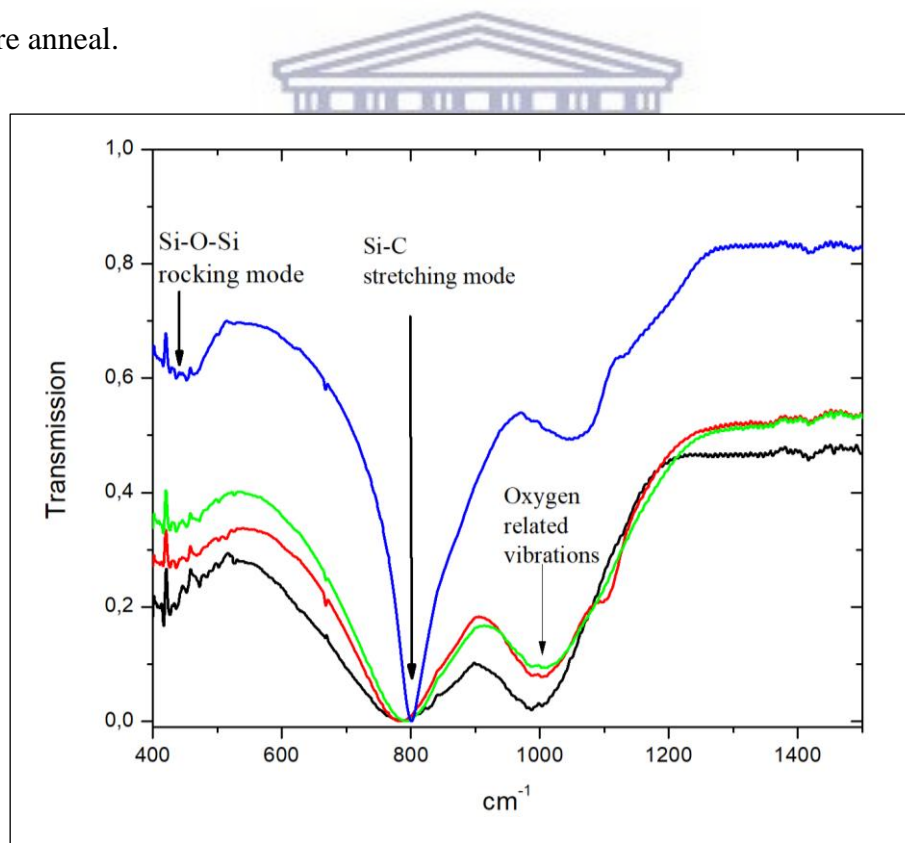


Figure 4.19: FTIR spectra of S₁, S₆, S₇, and S₈ plotted in black, red, green, and blue respectively.

4.8 Summary and recommendations.

4.8.1 Conclusions.

In this work, diffusion studies of implanted Ag^+ in SiC films were done. SiC thin films were processed on Si (100) substrates using e-beam evaporation from a commercial high purity hot pressed SiC sheet. The as-deposited films were thereafter implanted with Ag^+ ions.

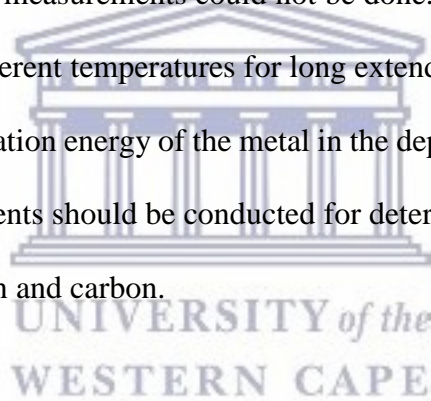
Realtime RBS experiments showed that Ag^+ was stable until 600 °C, which was the highest temperature that the heater in the system used could achieve. This temperature is well above the operating temperature of a conventional Si solar cell. Thus, we postulate that SiC is suitable a candidate for use as diffusion barrier material to guard against transition metal contaminants in Si based solar cells.

Conventional RBS studies on isochronally annealed films at higher temperatures in the range between 650 °C and 950 °C reveal that there is no significant change in the spectra up to a temperature of ~750 °C. At 850 °C a change in the Ag implantation profile was observed, suggesting that Ag is mobile at that temperature. The corresponding depth profile at 850 °C suggests that there is significant Ag in- diffusion, however, the overall integrated intensity results indicate that most of the Ag ions are escaping out of the films. After annealing for one hour at 950 °C, all the Ag has essentially escaped out of the films and/or spread throughout the layer below the detection limit of RBS. Isothermal annealing studies for varied times at 850 °C confirm Ag in-diffusion, but at the same time there is evidence of depletion of Ag near-surface regions as the annealing time increases; this suggests a continuous out-diffusion. FTIR investigations show a re-arrangement of the network at the annealing temperature where it was observed an accelerated rate of diffusion; on top of interstitial diffusion model proper to SiC at lower temperature than 1200 °C, we postulate that the diffusion was mediated by formed grain boundaries during the recrystallization process. The shoulders observed on the Ag depth

profiles during annealing were explained in terms of Ag which is ejected from the trapping sites that were formed either during the film processing or through ions damage during implantation.

4.8.2 Recommendations for future studies.

This is the first completed mini-thesis based on spectrometry studies on SiC films implanted with Ag⁺ for application in thin film Si solar cells in our department. We are aware that Ag diffusion kinetics in SiC films have not yet been optimized. Due to time constraints, more additional annealing and RBS measurements could not be done. Future work should focus on isothermal studies done at different temperatures for long extended periods of time so that the diffusion coefficient and activation energy of the metal in the deposited films can be extracted. Time of flight (TOF) experiments should be conducted for determination of the depth profiles of lighter elements like oxygen and carbon.



References.

- [4.1] J.F. Ziegler, M.D. Ziegler, and J.P. Biersek, *Interactions of ions with matter: SRIM – The stopping and range of ions in matter*, available from <http://www.SRIM.org/>
- [4.2] A. Y. Konobeyev, U. Fischer, Y. A. Korovin, and S. P. Simakov, *Evaluation of effective threshold displacement energies and other data required for the calculation of advanced atomic displacement cross-sections*, Nuclear Energy and Technology 3 (2017) 169- 175.
- [4.3] F. A. Shunk, *Constitution of binary alloys*, McGraw-Hill Company, New York, 1969.
- [4.4] K. Fukuda and K. Iwamoto, *Xenon diffusion behaviour in pyrolytic in SiC*, Journal of material science 11 (1976) 522 – 528.
- [4.5] R.R. Hart, H.L. Dunlop and O. J. Marsh, *Radiation Effects in Semiconductors*, (Gordon and Breach, New York, 1971) p. 405.
- [4.6] T. J. Gerczak, B. Leng, K. Sridharan, J. L. Hunter, A. J. Giordani, and T. R. Allen, *Observations of Ag diffusion in ion implanted SiC*, Journal of Nuclear Materials 461 (2015) 314–324
- [4.7] E. Friedland, J.B. Malherbe, N.G. van der Berg, T. Hlatshwayo, A.J. Botha, E. Wendler, and W. Wesch, *Study of silver diffusion in silicon carbide*, Journal of Nuclear Materials 389 (2009) 326–331.



Appendix A

Basic steps for simulation of RBS spectra with SIMNRA package.

SIMNRA is a computer simulation package that we used to simulate the measured RBS spectra. The swallow command was used to read experimental data stored in ASCII format without channel numbers by copying the experimental data into it with keywords “empty swallow”, as shown in fig. A.1. The channel numbers when reading into SIMNRA will start with 0.



Figure A.1: Example for an extended ASCII file which can be imported with “File→Read Spectrum Data→Swallow.”

The conversion from channels to energy was done using a standard with elements of known energies following a linear relation given by:

$$E[\text{keV}] = X \times \text{channelnumber} + Y$$

E is the particle energy in keV. The calibration offset Y must be entered in the calibration offset field, in keV as shown in fig. A.2 (a). The energy per channel X must be entered in the energy per channel field, X in keV/channel.

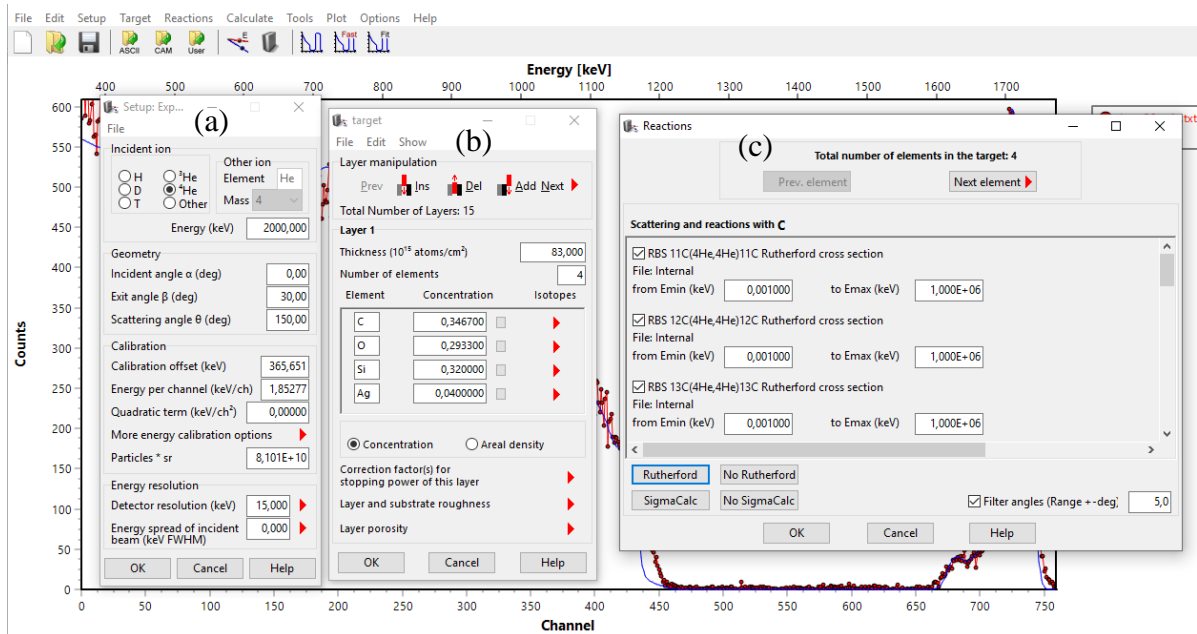


Figure A.2: A screenshot of the SIMNRA interface depicting the (a) experimental setup, (b) target, and (c) reactions windows, respectively.

The second step involves setting up experimental parameters such as incident ion, geometry, calibration, and energy resolutions using the “Setup→Experimental setup” command and the window in the fig. A.2 (a). The target of the sample was created by using the “Target → Target” and the window is shown in fig. A.2 (b). The thickness of the layer was entered in the “Thickness (10^{15} atoms/cm²)” textbox. The symbols of elements were entered in the text boxes provided in the “target” window after entering the value of “Number of elements”. The composition of a layer does not change throughout its thickness. To simulate a concentration profile we used multiple layers. The layer’s atomic concentration c must be $0.0 \leq c \leq 1$. The sum of the concentration of all elements in one layer must be equal to 1. In the reactions menu, the window is shown in fig. A.2 (c) the cross-section data used for the calculation of the simulated spectrum are chosen.

Appendix B

Basic steps for conversion of RBS spectra to depth profiles using DataFurnace package.

DataFurnace is a computer program that was used to extract depth profiles for RBS spectrum data. RBS spectrum data must be saved in an ASCII format, without the channel numbers, in order to read it into DataFurnace program. The data file was put into a separate directory because the program creates a large number of files so it is best to create a directory for each spectrum data to be converted. The spectrum data is read into DataFurnace using the “Spectra → Add spectrum” command. To start, the file path must be changed to the directory in which the data file is saved in by clicking on the textbox next to the “Directory” in the WinDF window shown in fig. B.1 (a). The data file was viewed in the “FileNames” sub-window as shown in fig. B.1 (a) by using the command “Setup → geometries → new” and it was stored in “6: 1024 x coll” format.

The next step involves setting up the experimental parameters such as the geometry and the structure of your sample. The geometry file was created by using the command “Setup → Geometry → New”, and changing the default setups to our experimental parameters and saving it under with a file format “6: 1024ch x coll” as shown in fig B.1 (b). The saved geometry file was viewed in the “Geometries” sub-window in fig. B.1 (a) by using the “Setup → Geometry → Add geometry” command. The geometry file is saved with a .geo extension and can be edited anytime. The data file and geometry file was associated by clicking on both and then clicking the Associate button which will enables for a number value to appear in the “Charge” sub-window (in fig. B.1 (a)) to appear.

The structure file was created using the “Setup→Structure→New” command, which can be edited at a later stage. The file is saved with .str extension and was read into the program by using the “Setup→Structure→Add structure”. It is necessary to create a “batch” file, and this was done by using the “Batch→Save batch” command. The batch file will be saved with a .spc extension.

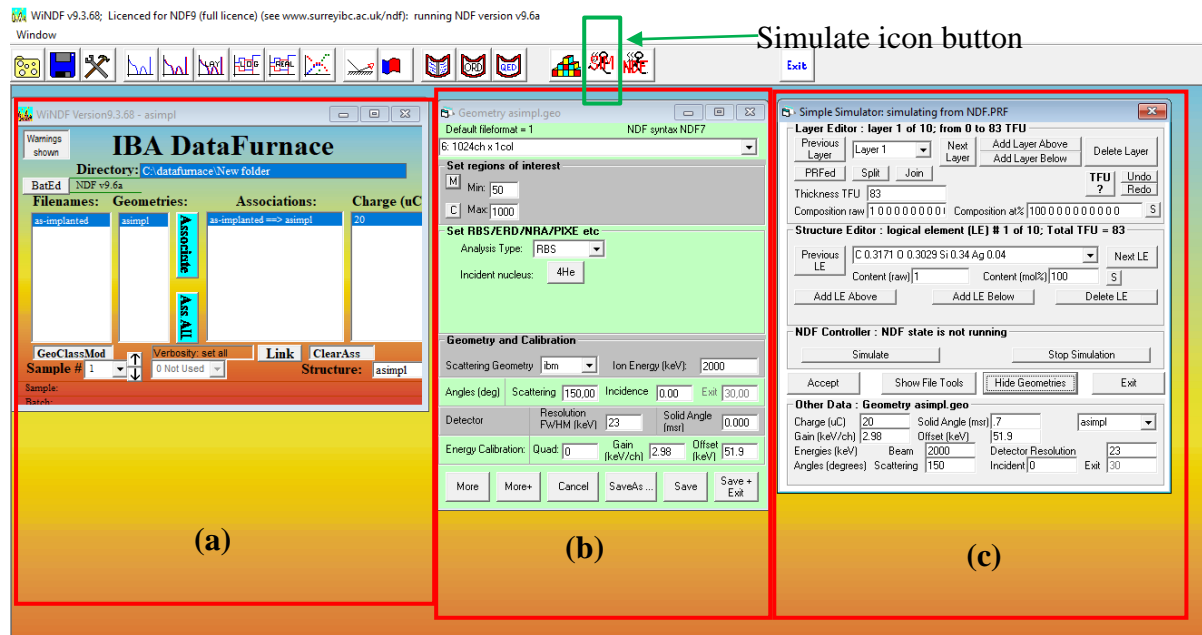


Figure B.1: A screenshot of DataFurnace interface depicting the (a) WinDF, (b) the geometry, and (c) sample simulator windows respectively.

To simulate spectrum data, we first had to build the structure by using the “target” values in SIMNRA. To get the window to show up in fig. B.1 (c), we clicked on the simulate button as shown by an overlaid green box pointed at, by an arrow in fig. B.1. The number of layers with their respective layers were added by clicking on the “Add Layer Below” in the “Layer Editor” group box shown in fig. B.1 (c). The number of layers was added in the “Structure Editor” group box by clicking on the “Add LE Below” button. The respective atomic concentration matching the ones used in SIMNRA was typed in the textbox available in the “Structure Editor” group box. The atom symbol together with its concentration must be typed with a space

separating them. The “Simulate” button was clicked to create the depth profiles. The depth profiles are automatically saved in the directory by clicking the save button and saving the .spc file that will appear on the pop-up window.

